SANDIA REPORT
SAND2018-0171
Unlimited Release
Printed January 2018

Modeling Heat Transfer and Pressurization of Polymeric Methylene Diisocyanate (PMDI) Polyurethane Foam in a Sealed Container

Sarah N. Scott

Prepared by
Sandia National Laboratories
Albuquerque, New Mexico 87185 and Livermore, California 94550

Sandia National Laboratories is a multimission laboratory managed and operated by National Technology and Engineering Solutions of Sandia, LLC, a wholly owned subsidiary of Honeywell International, Inc., for the U.S. Department of Energy's National Nuclear Security Administration under contract DE-NA0003525.

Issued by Sandia National Laboratories, operated for the United States Department of Energy by National Technology and Engineering Solutions of Sandia, LLC.

Available to DOE and DOE contractors from
U.S. Department of Energy
Office of Scientific and Technical Information
P.O. Box 62
Oak Ridge, TN 37831

Telephone: (865) 576-8401
Facsimile: (865) 576-5728
E-Mail: reports@osti.gov
Online ordering: http://www.osti.gov/scitech

Available to the public from
U.S. Department of Commerce
National Technical Information Service
5301 Shawnee Rd
Alexandria, VA 22312

Telephone: (800) 553-6847
Facsimile: (703) 605-6900
E-Mail: orders@ntis.gov
Online order: https://classic.ntis.gov/help/order-methods/

SAND2018-0171
Printed January 2018
Unlimited Release

Modeling Heat Transfer and Pressurization of Polymeric Methylene Diisocyanate (PMDI) Polyurethane Foam in a Sealed Container

Sarah N. Scott
Thermal/Fluids Science and Engineering
Sandia National Laboratories
P. O. Box 969
Livermore, California 87185-MS9957

Abstract

Polymer foam encapsulants provide mechanical, electrical, and thermal isolation in engineered systems. It can be advantageous to surround objects of interest, such as electronics, with foams in a hermetically sealed container to protect the electronics from hostile environments, such as a crash that produces a fire. However, in fire environments, gas pressure from thermal decomposition of foams can cause mechanical failure of the sealed system. In this work, a detailed study of thermally decomposing polymeric methylene diisocyanate (PMDI)-polyether-polyol based polyurethane foam in a sealed container is presented. Both experimental and computational work is discussed. Three models of increasing physics fidelity are presented: No Flow, Porous Media, and Porous Media with VLE. Each model us described in detail, compared to experiment, and uncertainty quantification is performed. While the Porous Media with VLE model matches has the best agreement with experiment, it also requires the most computational resources.

ACKNOWLEDGMENTS

The author would like to acknowledge Amanda Dodd, Victor Brunini, and Ryan Keedy for their contributions to the organic material decomposition project.

This work was funded by ASC V&V and P&EM.

TABLE OF CONTENTS

1. Introduction....................17
    - 1.1. PMDI Polyurethane Chemistry....................19
    - 1.2. Literature Review....................22
2. Background....................27
    - 2.1. Foam in a Can (FIC) Experiment Description....................27
    - 2.2. FIC Experimental Results....................28
    - 2.3. Description of No Flow decomposition and pressurization model....................31
3. No Flow Model....................37
    - 3.1. Mesh Resolution Study....................38
    - 3.2. Mean Value Method....................39
    - 3.3. Comparison of model and experiments....................41
        - 3.3.1. 150 C/min....................41
        - 3.3.2. 50 C/min....................43
    - 3.4. Addition of enclosure radiation....................45
        - 3.4.1. Description of interface tracking method....................45
        - 3.4.2. Results....................46
    - 3.5. Remarks....................52
4. Porous Flow Model....................53
    - 4.1. Description of model....................53
        - 4.1.1. PMDI Parameter Specification....................56
        - 4.1.2. The Ideal Gas Law....................57
    - 4.2. Mesh Resolution Study....................60
    - 4.3. Parameter Calibration....................64
        - 4.3.1. Original Calibration....................66
        - 4.3.2. Temperature and Pressure Calibrations....................68
        - 4.3.3. Thermal Conductivity....................69
        - 4.3.4. Optimization After Revisions to the Model....................74
    - 4.4. Validation of Calibrated Model....................75
        - 4.4.1. 150 C/min....................75
        - 4.4.2. 50 C/min Heating Rate with Parameters from 150 C/min Optimization 77
        - 4.4.3. The Phase of Decomposition Products....................78
    - 4.5. Remarks....................80
5. Porous Media with Vapor Liquid Equilibrium (VLE) Model....................83
    - 5.1. 5.1 Description of model....................83
        - 5.1.1. Fundamentals of VLE....................83
        - 5.1.2. Composition....................89
        - 5.1.3. Vapor Quality....................90
        - 5.1.4. Vapor Pressure....................92
        - 5.1.5. Application of VLE to PMDI RPU Foam in a Can....................92
    - 5.2. Implementation of the VLE model....................97
        - 5.2.1. Description of Implementation....................97
        - 5.2.2. Initial testing....................98

5.2.3. 5.3.1 2D Block Model 100
5.3. 2D Foam in a Can 102
5.3.1. Mesh Resolution Study 103
5.3.2. Nominal Results 104
5.3.3. Uncertainty Quantification and Sensitivity Study 105
5.4. 3D Foam in a Can Model 117
5.5. Remarks 119
6. Conclusion 121
6.1. 6.1 Comparison of the models 121
6.2. 6.2 Future Work 124
References 127

FIGURES

Figure 1: Illustration of the effects of liquefaction and flow, erosive channeling, and condensation in the upright and inverted orientations. 19
Figure 2: Formation of a general polyurethane 20
Figure 3: MDI structural formula 20
Figure 4: PMDI structural formula, where n ranges from 1 to 4 20
Figure 5: Structures of organic decomposition products 21
Figure 6: FIC Experiment: (a) experimental setup of the foam in a can experiments, (b) the location of thermocouples, (c) description of upright and inverted heating, and (d) an exploded view of the geometry. 28
Figure 7: Representative nominal experimental results: (a) 50 C/min and (b) 150 C/min upright (solid line) and inverted (dashed line) temperature vs time along the external side of the can. 29
Figure 8: X-Ray of the 50 C/min experiments when TC 25 is approximately 150C (423K) degrees in the (a) inverted and (b) upright orientations. The numbers on the image are the temperature (in C) of the thermocouple in that location. The pressure is also noted. These frames correlate with 850 seconds for the inverted and 1017 seconds in the upright. 29
Figure 9: Representative nominal experimental results: (a) 50 C/min and (b) 150 C/min upright (solid line) and inverted (dashed line) temperature vs time for thermocouple 25. . 30
Figure 10: Representative nominal experimental results for upright (solid line) and inverted (dashed line) internal can pressure vs time for (a) 50 C/min and (b) 150 C/min.... 31
Figure 11: Time vs temperature for the thermocouples separated by 180 degrees on outside of the can for the upright configuration, where the solid line are thermocouples 4, 16, 17, and 18 and the dashed lines are 2, 11, 12, and 13 (a) 50 C/min and (b) 150 C/min. 31
Figure 12: Schematic of the No Flow model 37
Figure 13: Mesh resolution study results: (a) temperature vs time of the embedded mass for the original (coarsest) mesh and for the 32x and 1024x more elements than the original mesh and (b) L_2 and L_∞ norms with best fit lines (L_2 best fit slope = -1.76 (R^2 = 0.99), L_∞ best fit slope = -0.83 (R^2 = 0.97)). 39

Figure 14: Computational results (solid) with $\pm\boldsymbol{2\sigma R}$ uncertainty and experimental results (dashed) with ±2% error for the exterior side thermocouples temperature vs time in the (a) inverted and (b) upright orientations.. 41
Figure 15: Inverted and upright computational results (solid) with $\pm\boldsymbol{2\sigma R}$ uncertainty and experimental results (dashed) with ±2% error for (a) temperature vs time for TC 25 and (b) pressure vs time. 42
Figure 16: Parameter importance vs time for pressure for (a) inverted and (b) upright.............. 42
Figure 17: Parameter importance vs time for (a) TC 17 and (b) TC 25 for the inverted configuration. 43
Figure 18: Computational results (solid) with $\pm\boldsymbol{2\sigma R}$ uncertainty and experimental results (dashed) with ±2% error for the exterior side thermocouples temperature vs time in the (a) inverted and (b) upright orientations.. 44
Figure 19: Inverted and upright computational results (solid) with $\pm\boldsymbol{2\sigma R}$ uncertainty and experimental results (dashed) with ±2% error for (a) temperature vs time for TC 25 and (b) pressure vs time. 44
Figure 20: Parameter importance vs time for pressure for (a) inverted and (b) upright.............. 45
Figure 21: Parameter importance vs time for (a) TC 17 and (b) TC 25 for the upright configuration. 45
Figure 22: Example decomposition of two linear triangle elements using CDFEM. Additional nodes are added at the interface location on the existing mesh edges. Interface edges are then added to connect the new nodes and create a surface that boundary conditions may be applied to. Finally, edges are added to divide any quadrahedra back into triangles. 46
Figure 23: Comparison of simulations (s) and experiment (e) for (a) one set of thermocouples on the side of the can and (b) the embedded object. 47
Figure 24: Comparison of pressure for simulation and experiment 47
Figure 25: Mass loss versus temperature for PMDI from TGA experiment 48
Figure 26: Comparison of three CDFEM threshold temperatures (550K, 600K, 650K), the simulation without CDFEM, and the experiment for (a) TC 16 and (b) TC 19...... 48
Figure 27: Comparison of three CDFEM threshold temperatures (550K, 600K, 650K), the simulation without CDFEM, and the experiment for (a) TC 25 and (b) pressure. . 49
Figure 28: X-Ray image of experiment after 630 seconds showing the foam receding from the heated plate.. 49
Figure 29: Cross-section of simulation after 630 seconds showing the foam receding past the embedded object when the threshold temperature is set at a) 550 K b) 600 K and c) 650 K. The darker gray represents the low temperature region and the lighter grey the high temperature region... 50
Figure 30: X-Ray image of experiment after 780 seconds showing the foam receding past the embedded object.. 50
Figure 31: Cross section of simulation after 780 seconds showing the foam receding past the embedded object when the threshold temperature is set at a) 550 K b) 600 K and c) 650 K. The darker gray represents the low temperature region and the lighter grey the high temperature region... 50
Figure 32: (a) 600 K (b) 650K threshold temperature simulation after 780 seconds showing the percentage of CO_2 with the decomposition surface drawn over the cross section of the FIC and (c) baseline simulation... 51

Figure 33: Comparison of pressure, (a) and (c), and temperature, (b) and (d), for varying emissivity (ranging from 0.2, the blue line, to 0.9, the gold line, in increments of 0.1) for the can in (a) and (b) and the foam in (c) and (b). Each results is compared with the experiment (green dashed) 51
Figure 34: Schematic of the Porous Media model 53
Figure 35: Generalized compressibility chart [58] with decomposition products indicated for 550 K and 12 MPa. 58
Figure 36: Generalized compressibility chart [58] with decomposition products indicated for 550 K and the partial pressure indicated in 59
Figure 37: Inverted (a) pressure vs time and (b) temperature vs time of the embedded mass for the meshes investigated in this study. 61
Figure 38: Inverted (a) pressure vs time and (b) temperature vs time for the difference between the finest (240x) and the mesh of interest. 61
Figure 39: Upright (a) pressure vs time and (b) temperature vs time of the embedded mass for the meshes investigated in this study. 62
Figure 40: Upright (a) pressure vs time and (b) temperature vs time for the difference between the finest (240x) and the mesh of interest. 62
Figure 41: Inverted Configuration. Time averaged L_2 and L_∞ convergence rates for (a) the solid temperature vs elements and (b) the gas temperature vs elements. The convergence rates for the temperature in the solid phase are $L_2 = -1.25$ and $L_\infty = -0.51$. In the gas phase, the rates are $L_2 = -0.91$ and $L_\infty = -1.23$ 63
Figure 42: Upright Configuration. Time averaged L_2 and L_∞ convergence rates for (a) the solid temperature vs elements and (b) the gas temperature vs elements. The convergence rates for the temperature in the solid phase are $L_2 = -1.25$ and $L_\infty = -0.51$. In the gas phase, the rates are $L_2 = -2.03$ and $L_\infty = -1.40$ 63
Figure 43: Cross sectional views of the temperature of the gas (foam region) and of solid temperature (can region) of the inverted mesh resolution study at (a) 10x, (b) 48x, (c) 63x, and (d) 240x 64
Figure 44: Inverted and upright experimental results for the 150 C/min experiments (a) temperature vs time for TC 25 and (b) pressure vs time. 66
Figure 45: Values explored for each run with optimized value highlighted for (a) virgin foam permeability, (b) char foam permeability, (c) organic gas fraction, and (d) char $\boldsymbol{\beta R}$ 67
Figure 46: Inverted and upright experimental results for the 150 C/min experiments (a) temperature vs time for TC 25 and (b) pressure vs time. 68
Figure 47: Pressure (a) and Temperature (b) compared to experiment when optimizing for only temperature 68
Figure 48: Pressure (a) and Temperature (b) compared to experiment when optimizing for only pressure 69
Figure 49: Cube of foam used to tests bulk conductivity theory. The cube is 1 cm cubed and sides 1 through 5 had an adiabatic boundary condition and side 6 was at a constant temperature of 400K 71
Figure 50: Temperature in the middle of side 1 and side 4 for the No Flow (NF), Porous Media (PM), and the decoupled Porous Media (PM no gas) 71

Figure 51: Temperature in the middle of side 1 and side 4 for the No Flow (NF), Porous Media with the original conductivity (PM), and Porous Media with volume averaged conductivity (PM k) 73
Figure 52: Pressure (a) and Temperature (b) for Constant Mass Diffusivity (ConstD), Varying Mass Diffusivity (VaryD), and Original Implantation (Orig) compared with experimental results (Exp) in the inverted (IN) and upright (UP) orientations. 74
Figure 53: Optimized simulation results (solid) with experimental values (dashed) for upright (blue) and inverted (red) for the 150 °C/min heating rate for (a) pressure and (b) temperature of the embedded object (TC 25).......... 75
Figure 54: Simulation results (solid) with experimental values (dashed) for the 150 °C/min heating rate for (a) pressure and (b) temperature of the embedded object (TC 25). 76
Figure 55: Simulation results (solid) with experimental values (dashed) for the 150 °C/min heating rate for (a) inverted and (b) upright.......... 76
Figure 56: Simulation results (solid) with experimental values (dashed) for the 50 °C/min heating rate for (a) pressure and (b) temperature of the embedded object (TC 25)............ 77
Figure 57: Simulation results (solid) with experimental values (dashed) for the 50 °C/min heating rate for (a) inverted and (b) upright.......... 77
Figure 58: Optimized separate organic liquid fraction simulation results (solid) with experimental values (dashed) for upright (blue) and inverted (red) for the 150 C/min heating rate for (a) pressure and (b) temperature of the embedded object (TC 25).......... 78
Figure 59: Separate organic liquid fraction simulation results (solid) with experimental values (dashed) for the 150 C/min heating rate for (a) inverted and (b) upright............... 79
Figure 60: Simulation results (solid) with experimental values (dashed) for the 50 C/min heating rate for (a) pressure and (b) temperature of the embedded object (TC 25)............ 80
Figure 61: Simulation results (solid) with experimental values (dashed) for the 50 C/min heating rate for (a) inverted and (b) upright.......... 80
Figure 62: Vapor pressure vs temperature for the major organic decomposition products. The vapor pressure is calculated using the Antoine equation (A), the Unger-Suuberg correlation with the original coefficients (UG), and the Unger-Suuberg correlation with Fletcher et al.’s coefficients (F). The temperature is limited to the range over which the Antoine equation was derived. 94
Figure 63: Vapor pressure vs temperature for the major organic decomposition products. The vapor pressure is calculated using the Antoine equation (A), the Unger-Suuberg correlation with the original coefficients (UG), and the Unger-Suuberg correlation with Fletcher et al.’s coefficients (F). The temperature is limited to the critical temperature.......... 95
Figure 64: Average gas temperature vs Pressure for the 50 C/min experiment displayed with the dew and bubble point calculated using both Raoult’s and Henry’s Law 96
Figure 65: Mole fractions in the liquid (x_i) and gas (y_i) phases for carbon dioxide and aniline .. 96
Figure 66: Average gas temperature vs Pressure for the 50 C/min experiment displayed with the mass vapor quality of aniline 97
Figure 67: Schematic of the 2D VLE model for a Block 99
Figure 68: Plots, over time, of (a) pressure and (b) temperature for the 2D block problem. Four combinations of representative decomposition products are compared............... 100

Figure 69: Plots, over time, of (a) pressure and (b) temperature of the steel block for the 2D block problem, comparing the Porous Media with and without VLE models...... 101
Figure 70: Plots of temperature, aniline mass concentration, and aniline quality for the 2D block problem, shown at five points in time for (a) inverted and (b) upright................ 102
Figure 71: Schematic of the VLE model for FIC 103
Figure 72: Three meshes used in the mesh resolution study and the number of nodes in the mesh (a) Coarse (b) Gradient, and (c) Finest.. 103
Figure 73: Mesh resolution results for the Inverted 2D meshes for (a) pressure and (b) temperature.. 104
Figure 74: Simulation results (solid) with experimental values (dashed) for upright (blue) and inverted (red) for the 150 °C/min heating rate for (a) pressure and (b) temperature of the embedded object (TC 25)... 104
Figure 75: Simulation results (solid) with experimental values (dashed) for the 150 °C/min heating rate for (a) inverted and (b) upright.. 105
Figure 76: Simulation results (solid) with experimental values (dashed) for upright (blue) and inverted (red) for the 150 °C/min heating rate for pressure with (a) the simulation error field representing the range of the simulations and (b) the simulation error field representing the first standard deviation of the simulations. 110
Figure 77: Simulation results (solid) with experimental values (dashed) for upright (blue) and inverted (red) for the 150 °C/min heating rate for TC25 with (a) the simulation error field representing the range of the simulations and (b) the simulation error field representing the first standard deviation of the simulations. 110
Figure 78: Simulation results (solid) with experimental values (dashed) for the inverted orientation and the 150 °C/min heating rate for the thermocouples along the sides of the can with (a) the simulation error field representing the range of the simulations and (b) the simulation error field representing the first standard deviation of the simulations. 111
Figure 79: Simulation results (solid) with experimental values (dashed) for the upright orientation and the 150 °C/min heating rate for the thermocouples along the sides of the can with (a) the simulation error field representing the range of the simulations and (b) the simulation error field representing the first standard deviation of the simulations. 111
Figure 80: Heat maps that correlates each parameter with each response for the inverted (left) and upright (right) simulation. A darker color indicates that the response is more sensitive to the parameter.. 112
Figure 81: Heat maps that correlates each parameter with each response for the inverted (left) and upright (right) simulation. A darker color indicates that the response is more sensitive to the parameter. In this map, 'Heat Flux' was removed at a parameter in order to be able to view the effects of the other parameters................................ 113
Figure 82: Top five sensitive parameters for TC1 for (a) inverted and (b) upright................... 114
Figure 83: Top five sensitive parameters for TC16 for (a) inverted and (b) upright................. 115
Figure 84: Top five sensitive parameters for TC17 for (a) inverted and (b) upright................. 115
Figure 85: Top five sensitive parameters for TC18 for (a) inverted and (b) upright................. 115
Figure 86: Top five sensitive parameters for TC19 for (a) inverted and (b) upright................. 116
Figure 87: Top five sensitive parameters for TC25 for (a) inverted and (b) upright................. 116
Figure 88: Top five sensitive parameters for Pressure for (a) inverted and (b) upright. 117

Figure 89: Simulation results (solid) with experimental values (dashed) for upright (blue) and inverted (red) for the 150 °C/min heating rate for (a) pressure and (b) temperature of the embedded object (TC 25). These results are for the 3D mesh used in the Porous Media only study. 117
Figure 90: Simulation results (solid) with experimental values (dashed) for the 150 °C/min heating rate for (a) inverted and (b) upright. These results are for the 3D mesh used in the Porous Media only study. 118
Figure 91: Simulation results (solid) with experimental values (dashed) for upright (blue) and inverted (red) for the 150 °C/min heating rate for (a) pressure and (b) temperature of the embedded object (TC 25). These results are for the 2D coarse mesh. 118
Figure 92: A comparison of the three models. Simulation results (solid) with experimental values (dashed) for upright (blue) and inverted (red) for the 150 °C/min heating rate for (a) pressure and (b) temperature of the embedded object (TC 25). 123

TABLES

Table 1: Major decomposition products of PMDI polyurethane foam 21
Table 2: Prefactor, exponent, and activation energy for the Arrhenius rate for each foam subgroup. 22
Table 3: Decomposition reaction scheme. 32
Table 4: PMDI reaction properties where $\boldsymbol{M}$ is the molar mass, $\boldsymbol{\Delta H}$ is the heat of reaction, $\boldsymbol{k0}$ is the frequency factor, and $\boldsymbol{EaR}$ is the activation temperature 32
Table 5: PMDI Foam Specific Heat 33
Table 6: PMDI 320 kg/m^3 Foam Bulk Thermal Conductivity 34
Table 7: Input parameters used in mean value method 41
Table 8: Decomposition reaction scheme. 56
Table 9: Thermochemical information for major decomposition products 57
Table 10: Mass and Mole fraction information using Ericson's global decomposition formula 58
Table 11: Critical Pressure and Temperature information using partial pressures 59
Table 12: Mesh resolution study 60
Table 13: Max error in quantity of interest for 15x mesh 64
Table 14: Parameters optimized in calibration 66
Table 15: Parameters optimized in calibration 69
Table 16: Measured thermal conductivity with respect to temperature 70
Table 17: Calculating the gas conductivity, $\boldsymbol{kg}$ 72
Table 18: Measured thermal conductivity with respect to temperature. NF bulk conductivity refers to the experimentally measured thermal conductivity that was used in the No Flow model, PM bulk conductivity refers to the bulk conductivity with the gas contribution removed, and PM solid conductivity refers to the conductivity of the solid phase alone (no pore space). 72
Table 19: Values of gas conductivity, experimentally measured by NIST, calculated using constant mass diffusivity, and calculated using the Chapman-Enskog theory. 74
Table 20: Parameters optimized in calibration performed after model changes 75
Table 21: Parameters optimized in two organic liquid fractions calibration 78
Table 22: Comparing optimized vales of 1 and 2 organic liquid fractions calibrations 79

Table 23: Coefficients used by various authors (note that these constants require units of Kelvin and atm) 92
Table 24: Thermochemical information for major decomposition products 93
Table 25: Antoine coefficients and the temperature range over which they are applicable for organic decomposition products, where the Antoine equation requires temperature in K and pressure in Pa [66] 93
Table 26: Input parameters used in LHS method. 107
Table 27: Progression of the model over time 124

EXECUTIVE SUMMARY

Polymer foam encapsulants provide mechanical, electrical, and thermal isolation in engineered systems. It can be advantageous to surround objects of interest, such as electronics, with foams in a hermetically sealed container to protect the electronics from hostile environments, such as a crash that produces a fire. However, in fire environments, gas pressure from thermal decomposition of foams can cause mechanical failure of the sealed system.

In this work, a detailed study of thermally decomposing polymeric methylene diisocyanate (PMDI)-polyether-polyol based polyurethane foam in a sealed container is presented. Both experimental and computational work is discussed. Validation experiments, called Foam in a Can (FIC) are presented. In these experiments, 320 kg/m^3 PMDI foam in a 0.2 L sealed steel container is heated to 1073 K at a rate of 150 K/min and 50 K/min. FIC is tested in two orientations, upright and inverted. The experiment ends when the can breaches due to the buildup of pressure from the decomposing foam. The temperature at key locations is monitored as well as the internal pressure of the can. When the foams decompose, organic products are produced. These products can be in the gas, liquid, or solid phase. These experiments show that the results are orientation dependent: the inverted cans pressurize, and thus breach faster than the upright. There are many reasons for this, among them: buoyancy driven flows, the movement of liquid products to the heated surface, and erosive channeling that enhance the foam decomposition.

The effort to model this problem begins with Erickson’s No Flow model formulation. In this model, Arrhenius type reactions, derived from Thermogravimetric Analysis (TGA), control the reaction. A three-step reaction is used to decompose the PMDI RPU (rigid polyurethane foam) into CO_2, organic gases, and char. Each of these materials has unique properties. The energy equation is used to solve for temperature through the domain. Though gas is created in the reaction mechanism, it does not advect, rather, its properties are taken into account when calculating the material properties, such as the effective conductivity. The pressure is calculated using the ideal gas law. A rigorous uncertainty quantification (UQ) assessment, using the mean value method, along with an analysis of sensitivities, is presented for this model. The model is also compared to experiments. In general, the model works well for predicting temperature, however, due to the lack of gas advection and presence of a liquid phase, the model does not predict pressure well.

Porous Media Model is then added to allow for the advection of gases through the foam region, using Darcy’s law to calculate the velocity. Continuity, species, and enthalpy equations are solved for the condensed and gas phases. The same reaction mechanism as in the No Flow model is used, as well as material properties. A mesh resolution study, as well as a calibration of parameters is conducted, and the model is compared to experimental results. This model, due to the advection of gases, produces gravity dependent results that compare well to experiment.

However, there were several properties that had to be calibrated, and replacing these calibrated parameters with physically derived values is desired. To that end, Vapor Liquid Equilibrium (VLE) equations are added to the Porous Media model. These equations predict the vapor/liquid split of the organic decomposition products based on temperature and pressure. UQ for the parameters in the model as well as a sensitivity study is presented, in addition to comparison to experiment. The addition of the VLE improved temperature and pressure prediction, both qualitatively and quantitatively.

NOMENCLATURE

Abbreviation	Definition
SNL	Sandia National Laboratories

1. INTRODUCTION

Polymers and other organic materials have a long history of use in mechanical systems to provide mechanical, electrical, and thermal isolation. However, compared to other engineering materials such as metals, the thermo-mechanical properties of these materials are still not well known. Additionally, polymers decompose at relatively low temperatures, making their properties even harder to characterize.

These polymers can be placed in hermetically sealed environments to protect objects of interest. Since these polymers create gasses when they thermally decompose, such systems can violently breach. Accurately modeling organic materials in thermal environments is therefore crucial for systems safety analysis, but can be challenging due to complex physics, uncertain thermal properties, and the relatively low decomposition temperatures. When polymers are exposed to a source of heat, such as fire, they undergo both physical and chemical changes [1]. The chemical breakdown, or decomposition, of the polymer causes large molecules to fragment, forming a variety of smaller molecules. These smaller fragments can vary greatly in size and properties and can undergo further decomposition. The chemical subspecies have differing equilibrium vapor pressures and those subspecies with the highest vapor pressures will quickly vaporize and in a sealed system can cause the container to pressurize. The subspecies that do not vaporize are left in either a liquid or solid form. While it is possible for a polymer to decompose completely into vapor, it is unlikely. Typically, solid residue is left behind and, in a material that chars, this layer can be porous.

The subspecies that do not vaporize are left in either a liquid or solid form. The liquid subspecies have the ability to flow and introduce a new path for heat transfer to initiate further decomposition. This flow creates channels in the polymer that, while difficult to predict, influence the overall rate of decomposition. Bubbling can also occur within the liquid subspecies. As decomposition continues within these subspecies, the vapor pressure increases in species that are not necessarily at the surface of the liquid. As the pressure and temperature build, these species will vaporize and force their way to the surface, similar to boiling water. In materials that char, if the char is covering virgin material, then decomposition continues and the subspecies will have to travel through the char to reach the surface. The hot char can cause secondary reactions in the subspecies and it can act as a thermal barrier between the virgin material and the heat source, slowing further decomposition.

Many factors can influence the decomposition of polymers. For example, decomposition can be accelerated by the presence of oxidants [2]. When compared to nitrogen, char formation in polyurethane increases in the presence of oxygen due to exothermic interactions between the oxygen molecule and the polymer. The previously discussed characteristics of polymers make the determination of properties difficult.

Of particular interest is polymeric methylene diisocyanate (PMDI)-polyether-polyol based polyurethane foam. When polyurethane decomposes, it produces a range of subspecies in the solid, liquid, and gas phases. In the application space of interest, the polyurethane foam is in a sealed, non-oxidative environment. While this means the gas subspecies will not exhibit flaming combustion, the gases will cause pressurization. In a sealed environment, the pressure of the gas will be dependent on the number of moles of the gas and the volume of the gas. Both of these factors are directly dependent on how the virgin polymer decomposes.

Historically, there have been efforts at Sandia National Laboratories (who funded the current work) to study organic materials and develop models to simulate their behavior in response to fire-like heat flux environments. Until recently, efforts were focused only on heat transfer through organics to components of interest. Recent efforts have focused on heat transfer as well as pressure generation. Erickson *et al*. [3 - 5] have developed models to simulate organic material decomposition and heat transfer through the organics using small-scale experiments to measure kinetic and thermal properties and a mid-scale experiment for validation of the model, which is discussed in detail in Chapter 2. Thermal Gravimetric Analysis (TGA), Fourier Transform Infra-Red (FTIR) spectroscopy, and Differential Scanning Calorimetry (DSC) were used to determine decomposition kinetics, heat of reaction, and specific heat. Thermal conductivities are taken from the literature and radiative properties were measured. The data from mid-scale experiment, known as Foam in a Can (FIC), were used for validation. The FIC experiment consists of a stainless steel cylindrical container filled with foam along with an embedded metal object. Many experiments have been performed with variations in the can design and/or variation in the foam. The cans have had different wall thicknesses, heating rates, hold temperatures, a range of densities, different foam types, and the can may be filled completely with foam or it may contain a gap of inert gas.

The model created by Erickson works well for foams that leave a structured char behind, however, PMDI polyurethane foam does not. Unlike the foams that leave a structure char, the pressure response for PMDI has a strong orientation dependence. The difference between the upright and inverted response is affected by the type of foam, density of foam, and applied boundary condition temperature history. For example, polyurethane foams liquefy and flow, exhibit erosive channeling, and have a distribution of decomposition products between the gas, liquid, and solid phases.

The nominal prediction of pressure does a poor job of capturing the difference between upright and inverted experimental behaviors because the model does not include the necessary physics. The model does however include model form errors to account for errors in the pressure prediction associated with the number of moles of gas, the volume that the gas occupies, and the temperature of the gas. The current model does not take into account gravity and therefore the model predicts the same results for both the upright and inverted heating orientations. However, as seen from the experimental data, there a marked difference between the two orientations. The physics that are playing a role in the difference between the inverted and upright orientations include liquefaction and flow, erosive channeling, and the distribution of decomposition of products between the gas and condensed phases. In the upright orientation, when the foam decomposes from a solid to a liquid, it pools on the top of the virgin foam and channels downward into the unreacted foam. However, in the inverted orientation, the liquid polymer can drip down onto the heated plate and almost instantly gasify. Figure 1 illustrates these concepts.

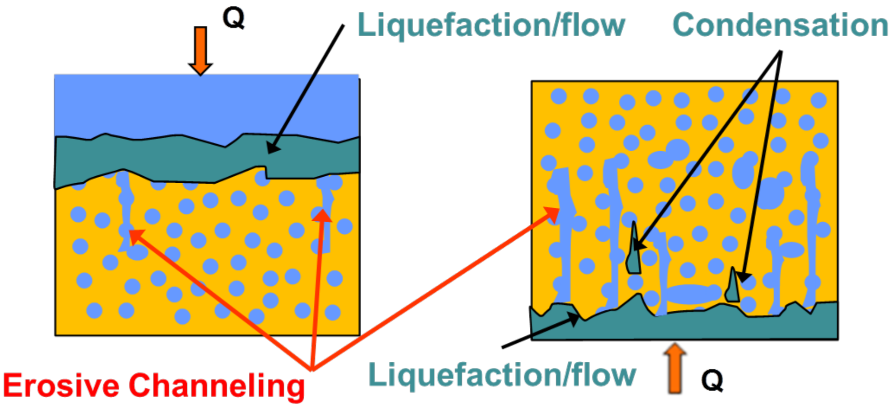

Figure 1: Illustration of the effects of liquefaction and flow, erosive channeling, and condensation in the upright and inverted orientations.

Of interest is assuring heat transfer through decomposing materials is correct as well as being able to predict the pressure generation as a function of time and temperature for a pressurizing region. This work will strive to make improvements in both of these areas by assessing the current models and adding additional physics. The modeling path forward involves incremental improvements to the current model formulation, a porous media formulation, and a method to handle the creation and destruction of a liquid phase. A multi-faceted approach is essential to address the important physics on an individual basis so that the most impactful and cost-effective pieces can be incorporated.

After a general introduction to polyurethane chemistry and a review of relevant literature, this work, in Chapter 2, will describe in detail the Foam in a Can validation experiments, interpreting the results in order to identify the physics that are important for modeling the problem. In Chapter 3, Erickson’s ‘No Flow’ model formulation is evaluated for PMDI polyurethane foam by preforming a rigorous uncertainty quantification assessment of the model. In Chapter 4, a Porous Media model is added to allow for the advection of gases through the foam region, using Darcy’s law to calculate the velocity. A mesh resolution study, as well as a calibration of parameters will be presented, and the model will be compared to experimental results. Chapter 5 will present a Vapor Liquid Equilibrium addition to the Porous Media model. Uncertainty quantification for the parameters in the model as well as a sensitivity study will be presented, in addition to comparison to experiment. This work will conclude with a comparison of the models presented and a path forward for future work.

1.1. PMDI Polyurethane Chemistry

Polyurethanes are generally formed by reacting an isocynate with a polyol. It is this reaction which causes the polymerization of the molecule that forms a polyurethane.

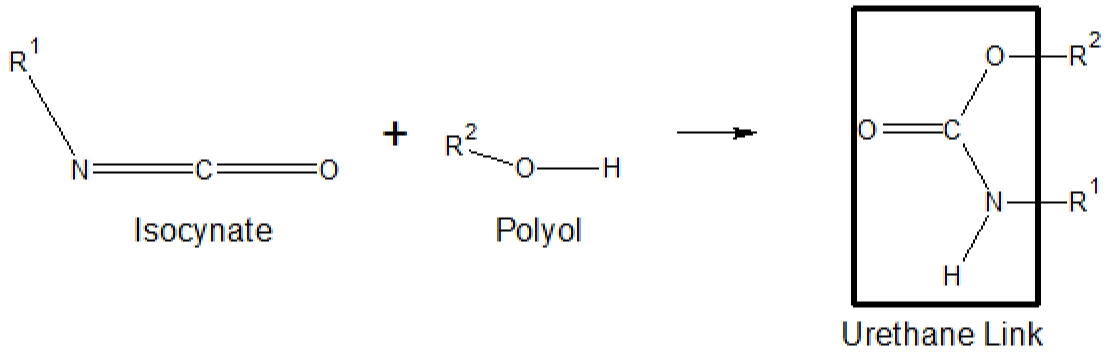

Figure 2: Formation of a general polyurethane

There are many different isocynates that can be used to form polyurethane. This work will deal with the isosynate PMDI (polymetric methylene diphenyl diisocyanate). There are two forms this isosyante can come in, the MDI arrangement and the PMDI arrangement. Figure 3 shows the MDI structure, with each of the parts of the molecule labeled. Figure 4 show the polymetric form, which is very similar to MDI, the difference being that several of the MDI molecules are linked together through a backbone of alternating pheyl groups and methylene [6].

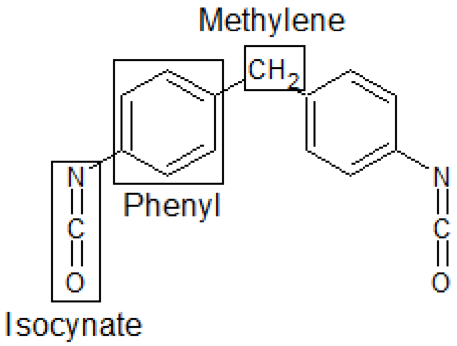

Figure 3: MDI structural formula

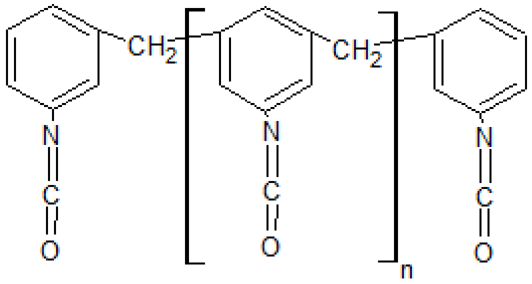

Figure 4: PMDI structural formula, where n ranges from 1 to 4

In order to form PMDI polyurethane foam, the PMDI must be reacted with polyols, catalysts, and water. Adding the water (or another blowing agent) will allow for the carbon dioxide to form, creating the bubbles in the foam. These bubbles are called ‘cells’, and the resulting foam can be closed or opened cell. An open cell foam is one where gas can flow through the cells (e.g., a seat cushion) and a close cell foam is one where gas cannot flow through the cells (e.g., the insulation in a refrigerator). In this work, close cell foams are of interest.

In previous work at Sandia National Laboratories, Erickson *et. al* collected FTIR (Fourier transform infrared spectroscopy) spectra data during TGA (thermogravimetric analysis) experiments on MDI rigid polyurethane foam [7]. The TGA experiments were done in either an unconfined for a partially confined sample container. The purpose of the partially confined was to allow a pressure build up in order to investigate how the reaction varied with pressure.

For the unconfined sample, the FTIR analysis indicated the presence of carbon dioxide and of isocyanates. For the partially confined samples, the isocynate signal was “greatly reduced” and the carbon dioxide signal increased. In addition, there was a signal indicating the presence of amine moieties. Erickson was able to identify the presence of phenyl isocynate, aniline, 4-methylaniline, water vapor, ammonia, and carbon dioxide. Nemer *et. al* conducted experiments to analyze the liquid decomposition products [8]. He found the primary products to be aniline, 4-methylaniline, and propylene glycol. The results are collected in Table 1

Table 1: Major decomposition products of PMDI polyurethane foam

Molecule	**Formula**	**Molar Mass**
Phenyl isocyanate	C7H5NO	119
Aniline	C6H5NH2	93
4-methylaniline	C7H9N	107
Propylene glycol	C3H8O2	76
Water vapor	H2O	18
Ammonia	NH3	17
Carbon dioxide	CO2	44

The structures for the primary organic decomposition products are shown in Figure 5.

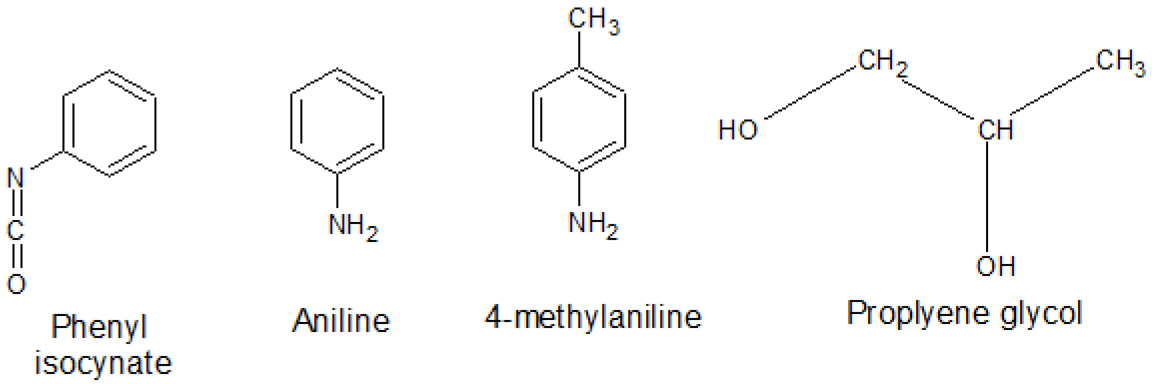

Phenyl isocynate

Aniline

4-methylaniline

Proplyene glycol

Figure 5: Structures of organic decomposition products

Using the TGA and FTIR data [3], [4], [7] Ericson *et. al* determined the global mechanism, on a mass fraction basis, to be:

$$PMDI\ RPU\ \rightarrow 0.25\ CO_2 + 0.20\ LMWO + 0.35\ HMWO + 0.2\ char \qquad 1$$

This decomposition mechanism is governed by three reactions. In order to simplify, it is assumed that the PMDI polyurethane foam is comprised of three subgroups, *FOAMA*, *FOAMB*, and *FOAMC*, such that:

$$PMDI\ RPU\ = 0.45\ FOAMA + 0.15\ FOAMB + 0.4\ FOAMC \qquad 2$$

These foam subgroups decompose through these mechanisms:

$$FOAMA\ \rightarrow 0.56\ CO_2 +\ 0.44\ LMWO \qquad 3$$

$$FOAMB\ \rightarrow\ HMWO \qquad 4$$

$$FOAMC\ \rightarrow 0.5\ HMWO + 0.5\ char \qquad 5$$

The reaction takes the general Arrhenius form:

$$k = AT^{\beta} e^{-E_a/RT} \qquad 6$$

Where for the three reactions:

Table 2: Prefactor, exponent, and activation energy for the Arrhenius rate for each foam subgroup.

Reaction	A	β	E_a
Foam A	8.077 x 10^{12}	0	179441062
Foam B	0.179 x 10^{12}	0	179441062
Foam C	8.906 x 10^{9}	0	179441062

1.2. Literature Review

Polyurethane foams have been studied for many years due to its wide use in residential, engineering, and petro-chemical applications. For example, the smoldering ignition of upholstery is a leading cause of death in residential fires [9]. To successfully model the ignition of polyurethane, a chemical kinetics mechanism that controls pyrolysis must be proposed. This is typically done by preforming thermographic analysis combined with Fourier transform infrared spectroscopy (TGA-FTIR). For example, for a toluene diisocyanate (TDI) polyurethane foam, a five step reaction mechanism has been proposed by Rogaume [10]. Analysis of the gases showed the principle products to be CO_2, CO, H_2O, NO and complex hydrocarbons [11].

In order to successfully simulate the pyrolysis of a solid, more than just the kinetic mechanism must be modeled. Heat, momentum, and mass transfer as well as the chemical processes must be considered [12]. These simulations have been performed for a variety of materials, from woods and other natural materials [12], to polymers such as PMMA [13], and polyurethanes [14]. An example of a numerical code used to simulate the pyrolysis of these types of materials is Gpyro [15]. Gpyro solves for conjugate heat transfer, fluid flow and pressurization using Darcy's law for porous media, gas species diffusion and convection, and heterogeneous and homogenous reaction kinetics. A derivation similar to that which Gpyro was based was used to implement a porous flow capability into the Sierra Thermal/Fluids codes used at Sandia National Laboratories [16] and will be further discussed in Chapter 4.

The use of a Darcy's law based porous flow derivation for determining the flow velocity is not uncommon. It's often used in geology, for example in seismic analysis [17] and hydrology [18], but has been used in other fields, such as in bioengineering to model drug delivery [19]. In combustion, Darcy's law have been used numerically study the flame stabilization in a porous burner [20, 21], as well as the flow through a pyrolyzing medium. For example, it has been used to study pyrolysis in open cell polyurethane foams. Dodd *et al.* [22] presented a two dimensional numerical formulation of a block of polyurethane foam, which includes a seven step kinetic model for the smolder mechanism. This formulation also included the effect of heat, mass, species, and momentum transfer of the porous solid and gas phases, and showed that the model was sensitive to boundary conditions, thermal properties, and the heat of reaction of both the char and the oxidization reaction. This formulation was used to study the transition from smoldering to flaming [23]. Darcy's law has also been used to study the heat and mass transport in developing char layers in polymers [24]. In this work, Staggs shows that the evolution of both temperature and gas pressure are governed by the diffusion process, but cautions the reader that these interpretations only hold true as long as the char remains structured enough for Darcy's law to remain valid.

The liquid phase is also of interest when studying pyrolyzing polymers. For thermoplastics, an external heat source can cause the polymer to melt and flow. Melting polymers can change the flammability properties of the material [25] as well affect the upwards flame spread [26]. The melting of the polymers can also cause the dripping and pooling of flammable liquid, as seen in Butler *et al.* [27, 28]. In this experimental and computational work, a radiant heat source was directed at a vertical slab of polypropylene. The surface of the slab would melt and drip. The mass of the slab and dips were measured in real time. Butler and Oñate then modeled this phenomena using a particle finite element method (PFEM) to track the movement of plastics that have a defined melting temperature [29]. PFEM combines concepts from particle-based techniques with those of the standard FEM by defining a point cloud within the domain for each point in time. Next an Alpha-Shape function defines the free surface of the melting zones. A mesh is then generated using the points in the point cloud as the nodes. These melting thermoplastic mass loss simulations agreed well experimental results, proving the use of this PFEM technique. However, this work did not account for detailed reaction kinetics, but it did include a gasification term in order to account for additional mass loss.

Problems arise when the polymer being modeled is a thermoset (like rigid polyurethane foam), rather than a thermoplastic. An effort to model the liquefaction of such a polymer was performed by Sun [30] at Sandia. Sun used an Arbitrary Lagrangian Eulerian (ALE) method to model Removable Epoxy Foam (REF). The ALE method can both track the movement of a mesh inside a domain, as well as the interfaces between domains. This allows for the independent tracking of the solid, liquid, and gas states of the foam. In the ALE method, special attention must be paid to the original mesh as well as how the nodes are moved so that the mesh does not tangle. Sun combined the ALE method for tracking the liquefaction of the foam and a previously developed model to simulate the decomposition of the solid foam. Sun's results matched experimental data qualitatively; however, the liquid domain moved through the volume about four times faster than seen in experiments.

Other front tracking methods exist and can be used for a range of physics, not just flow. Conformal Decomposition Finite Element Method (CDFEM), has been explored by Noble *et al* [31]. In this method, an unstructured background mesh is created. As the simulation goes forward in time, the background mesh is then decomposed into the subdomains using level set fields, where the mesh conforms to the geometry of the phase. The advantage of tracking the boundary in this manner is that the mesh does not tangle as in the ALE method. This method can be used to create radiation enclosures that change over time.

An ever present issue with numerical models determining the material and chemical properties of the materials being modeled. Statistical methods can be useful in this regard. For example, genetic algorithms (GA) have been used to determine the kinetics of open cell polyurethane from TGA data [32]. This class of algorithms, known as global methods, have also been useful in determining thermal properties. Burns *et al.* [33] used sequential quadratic programming algorithm (SQP) to compare different model forms for non-isothermal TGA data for polyethylene and polymethylmethacrylate (PMMA). Garcia *et al*. [34] used a GA to obtain thermal properties (conductivity, specific heat, Rosseland-mean extinction coefficient, and scattering albedo) in two scenarios: an anisotropic composite material and an isolative foam (polystyrene). They found that when parameters were correlated, which often occurs, that the genetic algorithms can succeed in obtaining results, whereas linear methods will tend to fail. Chaos *et al.* [35] used shuffled complex evolution (SEC) along with a GA to obtain the material properties from pyrolysis data. They showed that SEC tended to converge faster, and with a better goodness of fit than GA.

Statistics can be brought to bear not only on model calibration but also model uncertainty. Overholt *et al.* used a Bayesian inference approach to calculate probability distributions for heat release rate and location of a fire in fire scene reconstructions and suggests that the probability distributions can be used for uncertainty propagation through the model [36]. Bruns *et al.* propagated the error for the kinetic parameters for several polymers into a condensed phase burning model, also using Bayesian inference [37]. The sensitivity of the physical and chemical properties to the burning rate for polymers was studied by Stoliarov *et al* [38]. They showed that understanding the decomposition reactions (pre-exponential factor, activation energy, heat, and char yield) proved most important to accurately predicting the peak and average burning rates. Linteris [39] showed that for PMMA's mass loss rate, the parameters that were most important were, in the order of decreasing importance: heat of reaction, thickness, specific heat, absorption coefficient, thermal conductivity, and activation energy. Matala *et al.* conducted Monte Carlo fire simulations using Latin hypercube sampling to estimate the time dependent probability of power cable failure in a fire [40]. Summers *et al.* [41], [42] conducted a validation and sensitivity analysis of a thermal-structural model to predict the failure of compressively loaded fiber-reinforced polymer laminates that were heated by a fire, finding that the model was particularly sensitive to the thermal expansion coefficient and the elastic modulus. Finally, Bal and Rein [43, 44] have shown that once uncertainty is propagated through a high number of reaction mechanisms, the resulting spread in the simulated data can be larger than when using a smaller number of mechanisms.

2. BACKGROUND

2.1. Foam in a Can (FIC) Experiment Description

The experimental data that is used for validation is referred to as Foam in a Can (FIC). The experimental configuration consists of a stainless steel cylindrical container filled with foam and an embedded metal object (Figure 1a and 1d). This experiment has been performed in the upright and inverted orientations (Figure 1c) [14], [15]. The sidewalls of the container are seamless tubing, 8.89-cm (3.5-in) outside diameter and 1.60-mm (0.063in) wall thickness. The raw tube material purchased for the sidewalls had a wall thickness of 4.76-mm (0.1875 in); thus, it was machined down for use in the test articles. The heated plate was machined from SS304L, 10.8 mm (0.425-in) thick. The base plate was a similar thickness but included an embedded mass. The encapsulated SS304L mass was 4.45 cm (1.75 in) in diameter and consisted of a solid and a hollow end. The exterior surfaces of the can were painted with Pyromark^{TM} 2500 series flat black paint to ensure consistent, uniform radiative properties. Foam samples are cast oversized and then machined to a snug fit in the container and around the encapsulated mass. The foam samples were polymeric methylene diisocyanate (PMDI)-polyether-polyol based polyurethane foam with a density of approximately 320 kg/m^3 (20 lb/ft^3). Mass of the individual foam samples was documented and the range was 60 to 65g.

The radiant heat flux from the array of silicon rod heaters directed at the lid of the can causes the polymer to decompose and the container to pressurize. Temperatures were measured during the experiment using thermocouples (TC) mounted on the exterior of the can and by embedded thermocouples in the object, lid, and base (Figure 1b). Thermocouples 1-4 and 20-27 were ungrounded, 1.62-mm (0.063-in) diameter Inconel™-sheathed K-type thermocouples that were imbedded in drilled holes within the test article. Thermocouples 5-19 and 28-30 were ungrounded, 1.02-mm (0.040-in) diameter Inconel™-sheathed K-type thermocouples that were tacked welded to the can sleeve using nichrome strips. The error associated with the mounting method was incorporated into the experimental uncertainty. A pressure transducer was used to measure pressure response during the experiment, which was connected to the vent tube shown in Figure 1d. Measurement error on thermocouples and transducer was ± 2%. X-rays were also used to observe physical changes of the foam as a function of time throughout the experiment. This experimental test series yielded eight experiments using a nominally 320 kg/m^3 (20 lb/ft^3) density PMDI sample with the lid heated to 1073K (800°C) at a rate of 150 K/min and 50 K/min, four each in the upright and inverted orientation. The experiment ended when the can breached due to foam decomposition pressurization of the can. Test to test variability was small, as a result, a subset of experiments (one upright and one inverted) were selected for discussion.

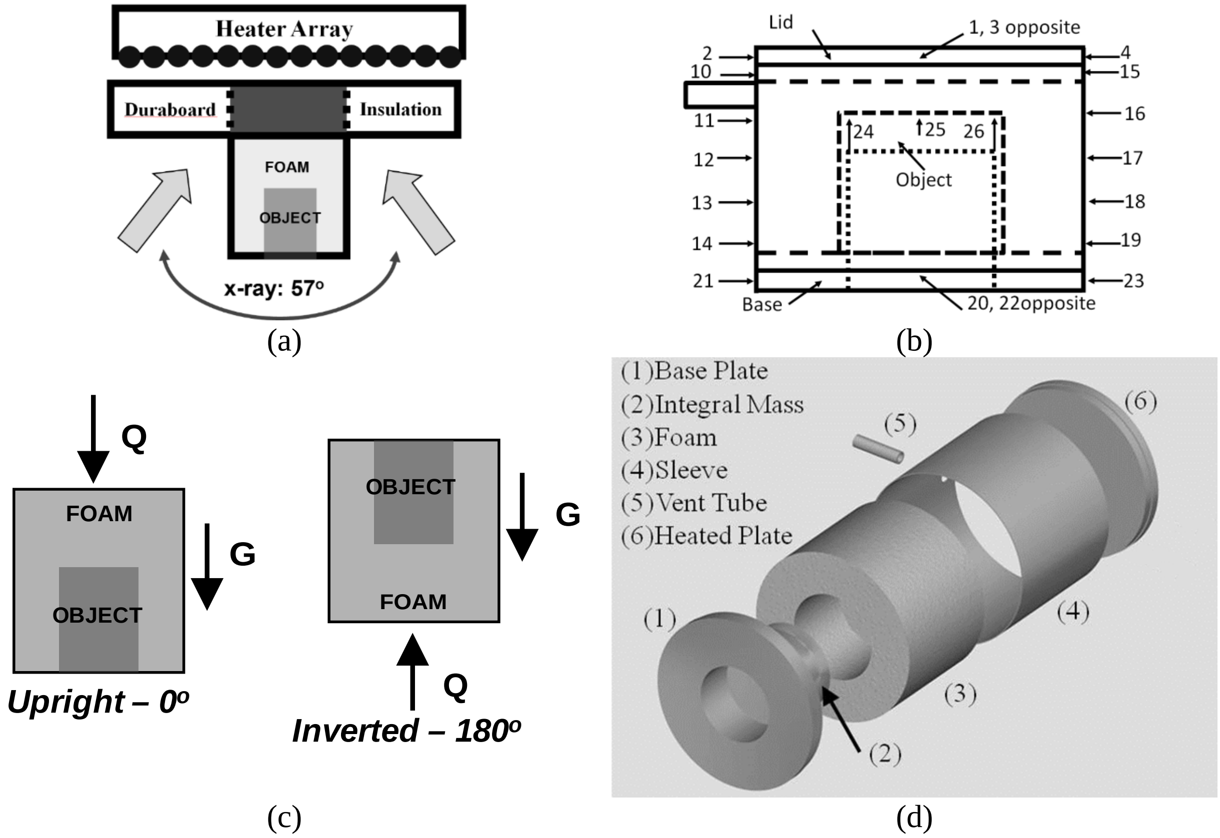

Figure 6: FIC Experiment: (a) experimental setup of the foam in a can experiments, (b) the location of thermocouples, (c) description of upright and inverted heating, and (d) an exploded view of the geometry.

2.2. FIC Experimental Results

In 2012 and 2013, a series of experiments were conducted by Suo-Anttila *et. al.* where the FIC filled with PMDI polyurethane foam at a density of 20lb/ft^3 (320 kg/m^3) was heated to 800C at two rates, 50 C/min [46] and 150 C/min [45].

Figure 7 shows representative temperature responses of select thermocouples along the outside of the can for both the 50 C/min and the 150 C/min experiments (see Figure 6b for a map of the thermocouples). The inverted experiments tend to be shorter in duration than the upright experiments, due to a steeper pressure rise, as seen in Figure 10. This orientation dependent response is caused by motion of the liquid foam decomposition products. X-ray images (Figure 8) show that in the upright orientation the foam decomposes, liquefies, and moves away from the heated plate. While in the inverted orientation, the liquefied foam decomposition products drip down onto the heated lid, increasing the rate of gasification, and thus pressurization. In addition, liquefaction and flow appear to be exacerbated by erosive channeling of hot gases and vapors penetrating into the bulk foam. One can also see from Figure 7 that, for both the 50 C/min and 150 C/min experiments, the inverted can breaches at approximately the same time the can reaches its set temperature (signified by a plateau in in the temperature). The inverted temperature is also slightly higher for the thermocouples further from the hot plate (e.g. TC 18) in the inverted orientation. This might be due to buoyancy induced flow on either the inside or outside of the can.

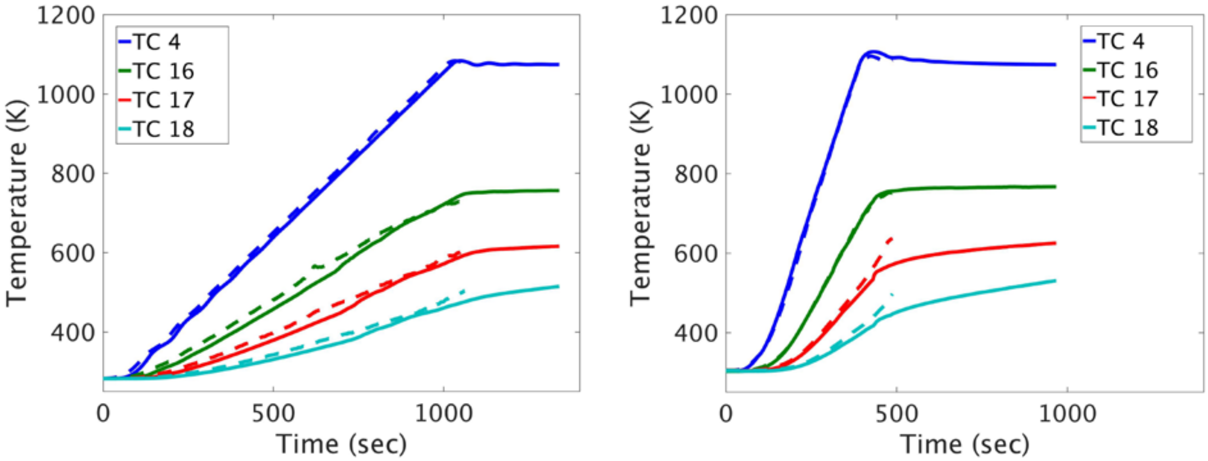

(a) (b)

Figure 7: Representative nominal experimental results: (a) 50 C/min and (b) 150 C/min upright (solid line) and inverted (dashed line) temperature vs time along the external side of the can.

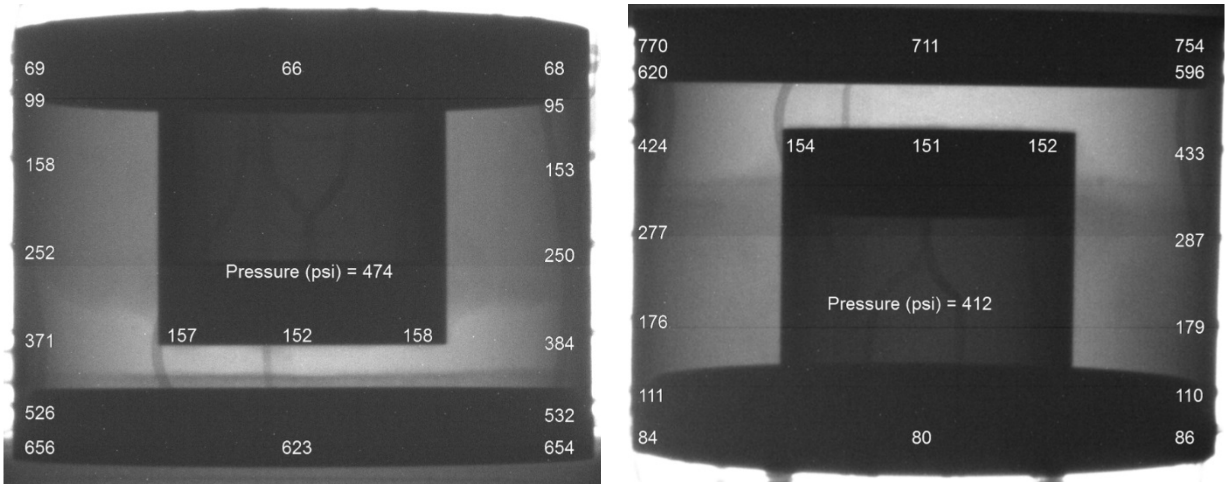

(a) (b)

Figure 8: X-Ray of the 50 C/min experiments when TC 25 is approximately 150C (423K) degrees in the (a) inverted and (b) upright orientations. The numbers on the image are the temperature (in C) of the thermocouple in that location. The pressure is also noted. These frames correlate with 850 seconds for the inverted and 1017 seconds in the upright.

Figure 9 shows the temperature of TC 25 in both the upright and inverted orientations for both heating rates. There are several interesting phenomena to note. First, the final temperature in the inverted case is always less that in the upright. This can be explained by the shorter duration of the experiment, allowing less time for the slug to heat up. However, for the same point in time, the inverted experiment has a higher slug temperature than the upright. Two possible explanations for the enhanced heat transfer to the slug in the inverted orientation are enhanced convective heat transfer due to buoyant flow of the decomposition product gases, and condensation of hot gas decomposition products onto the cooler slug (a heat-pipe like effect).

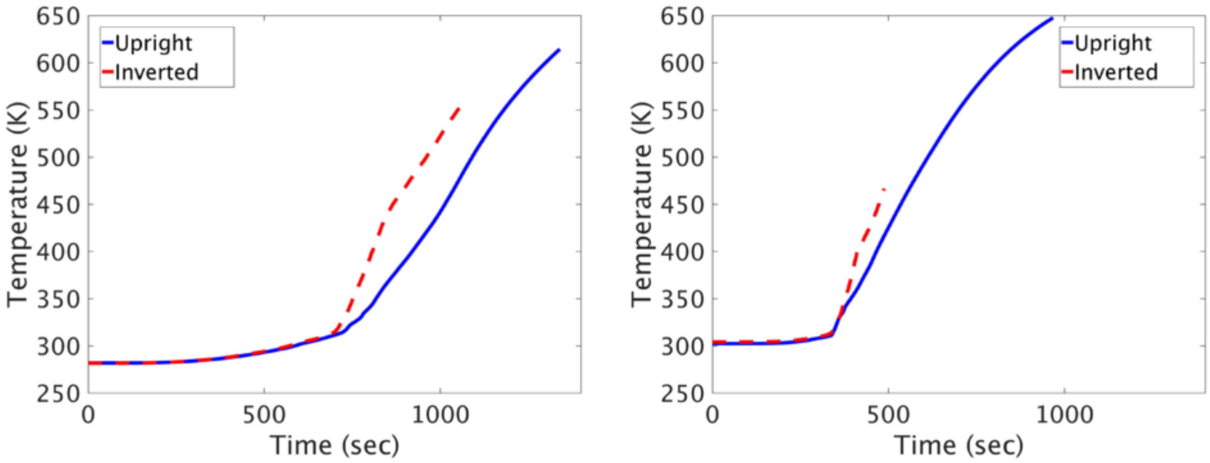

(a) (b)

Figure 9: Representative nominal experimental results: (a) 50 C/min and (b) 150 C/min upright (solid line) and inverted (dashed line) temperature vs time for thermocouple 25.

One other notable difference between the 50 C/min and 150 C/min experiments is that, while the upright experiment final slug temperatures are within 50C, the inverted experiment has over a 100C final temperature difference between the two heating rates. This may be a result of the presence of liquid decomposition products. More liquid products were observed in the 50 C/min than 150 C/min experiments. This is because there is a longer period of time in which the temperature and the pressure in the can are conducive to the existence of a liquid phase. As seen in Figure 10, the slope of the inverted orientation pressure curve is not as steep for the slower heating rate. There is not as much change in the slope of the upright curve. The vaporization of the liquid decomposition products may be what is causing this difference. In the lower heating rate, the hot plate is at a lower temperature for longer. While this will not have a large impact on the upright configuration, in the inverted case this would mean that the liquid foam drops down onto a cooler surface and remains in the liquid phase, thus lowering the pressure rise. The pool of liquid on the heated plate then slowly boil off (as the plate increases in temperature). These organic gases could then condense on the slug, in effect creating a heat pipe. This effect would be more pronounced in the inverted than upright configuration. It’s also possible that when the liquid foam drops down onto the heated plate at a higher heating rate, rather than go through a phase change, it goes through a further decomposition. The products that are formed in this decomposition would then have different boiling points than the original material, which may not be able to condense on the slug. The lower heating rate may also have an effect on the flow velocity, altering the rate of heat transfer.

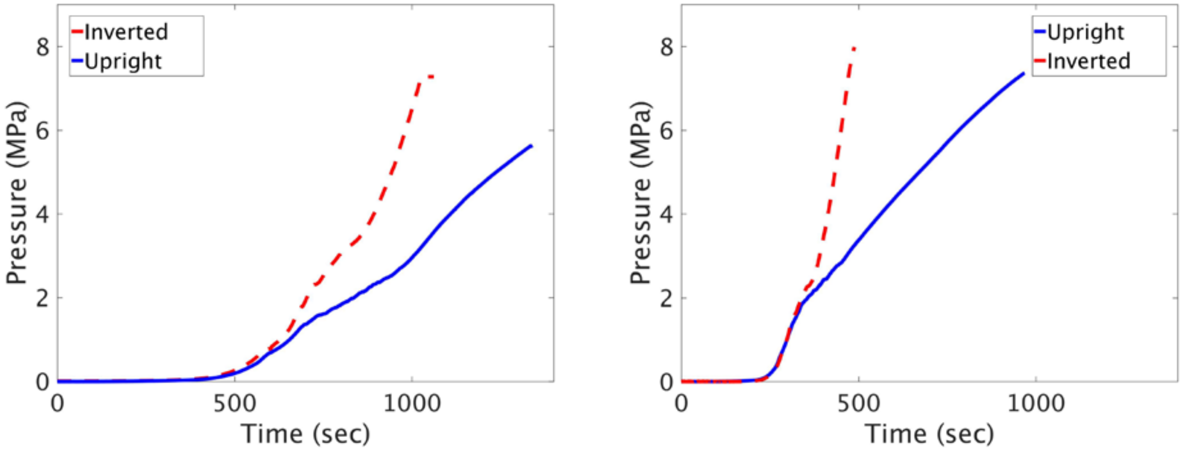

(a) (b)

Figure 10: Representative nominal experimental results for upright (solid line) and inverted (dashed line) internal can pressure vs time for (a) 50 C/min and (b) 150 C/min

A series of thermocouples were placed on either side of the exterior of the can, separated by 180 degrees (Figure 11). While there is circumferential variability due to the nature of the foam decomposition, only one series of external thermocouples will be presented when comparing to the simulations, though through experimental error, the variability will be captured.

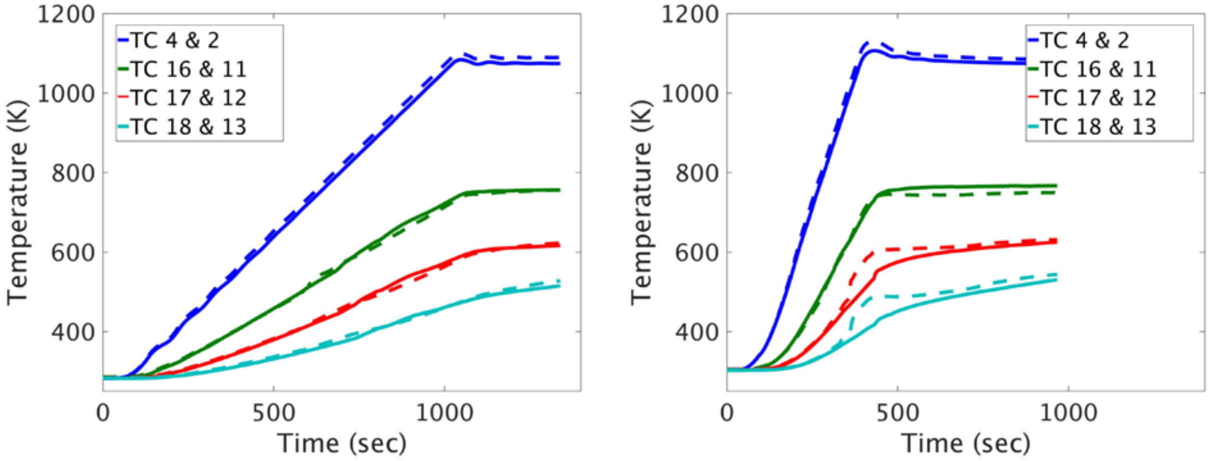

(a) (b)

Figure 11: Time vs temperature for the thermocouples separated by 180 degrees on outside of the can for the upright configuration, where the solid line are thermocouples 4, 16, 17, and 18 and the dashed lines are 2, 11, 12, and 13 (a) 50 C/min and (b) 150 C/min.

2.3. Description of No Flow decomposition and pressurization model

In previous work at Sandia National Laboratories, Erickson *et al* [3] developed a conduction-radiation approach for modeling decomposing organic materials that pressurize a sealed container. This approach uses temperature response to provide the basis for predicting gas-vapor generation rates and container pressure. Radiation heat transfer was modelled using the diffusion approximation.

In this model, the energy balance for heat transfer through the foam is given by:

$$\rho c \frac{\partial T}{\partial t} = \nabla(k + k_e)\nabla T + \sum_i \rho r_i(-\Delta H_i) \qquad 7$$

Where ρ is the bulk mass density of the foam; c is the specific heat; T is temperature; t is time; k is the thermal conductivity; k_e is an effective conductivity for radiant heat transfer in optically thick material; r_i are the overall rates of the reactions describing formation of final condensed and gas phase products during foam decomposition; and ΔH_i are the overall heats of reaction of the initial foam to form final products. The equations describing reaction rates r_i and time-dependent container pressure are discussed below. The pressure was solved using a user-defined subroutine which was sub-cycled at each time step during the solution of Equation 7.

Rate expressions for the r_i describing polymer decomposition and gas formation were based on the following reaction scheme (see Table 3). Thermal decomposition chemistry of the foams was examined using thermal analysis and infrared spectroscopy techniques discussed previously [7]. Resulting parameter values for PMDI-based foam are given in Table 3 and Table 4.

Table 3: Decomposition reaction scheme.

Initial Foam	Reaction	Decomposition Products
$0.45\,FOAMA + 0.15\,FOAMB + 0.4\,FOAMC$	→	
FOAMA	r_1	$0.56\,CO_2 +\ 0.44\,Oragnic\ Vapors$
FOAMB	r_2	$Oragnic\ Vapors$
FOAMC	r_3	$0.5\,Oragnic\ Vapors + 0.5\,Char$

Table 4: PMDI reaction properties where M is the molar mass, ΔH is the heat of reaction, k^0 is the frequency factor, and E_a/R is the activation temperature

Initial Foam	Decomposition Species	M (kg/mole)	ΔH kJ/kg	k^0 (s^{-1})	E_a/R (K)
FOAMA	CO_2	44	0	$8.0\text{x}10^{12}$	21,600
	Organic vapors	80			
FOAMB	Organic vapors	120	0	$1.8\text{x}10^{11}$	21,600
FOAMC	Organic vapors	120	0	$8.9\text{x}10^{9}$	21,600
	Char	NA			

The reaction rates for this problem are first order Arrhenius, therefore:

$$r = -\frac{d(FOAM)}{dt} = k\ FOAM(t) = k^0 \exp\left(\frac{-E_a}{RT}\right) FOAM(t) \qquad 8$$

Where $FOAM(t)$ is the fraction of $FOAM$ remaining at time t and $FOAM$ can be $FOAMA$, $FOAMB$, or $FOAMC$.

Equations for calculating the container pressure, P, are based on the ideal gas law $PV_g = n_g RT$ or $P = \left(n_g/V_g\right)RT = \bar{\rho}_g RT$ and on the assumption that pressure gradients relax rapidly, so that pressure is independent of position (in the sealed volume) and is only a function of time. Then,

$$P = \frac{n_g R}{\int_{V_g} \frac{1}{T}\, dV_g} = \frac{n_g R}{\int_{V_{vac}} \frac{1}{T}\, dV_{vac} + \int_{V'_{pore}} \frac{1}{T}\, dV'_g} = \frac{\left(n_{fv}^0 + n'_g + n_\phi^0\right)R}{\int_{V_{vac}} \frac{1}{T}\, dV_{vac} + \int_{V_{foam}^0} \frac{\Phi}{T}\, dV_{foam}^0} \qquad 9$$

Where:

- n_g is the total number of moles of gas and vapor in the contiguous gas-vapor phase volume V_g;
- n_{fv}^0 is the number of moles of gas in the initial vacant volume in the system, V_{vac};
- n'_g is the number of moles of decomposition products in the contiguous gas-vapor phase;
- $n_\phi^0$is the initial number of moles of gas in the cells of the foam;
- V'_g is the volume of the contiguous gas-vapor phase within the initial bulk volume of the foam, V_{foam}^0;
- V_{fv} is the initial vacant volume the container;
- the total gas-vapor phase volume is the sum of the initial vacant volume and the gas-vapor volume within the bulk of the foam, $V_g = V_{vac} + V'_{pore}$;
- Φ is the porosity and is a function of extent of reaction.

Convective and radiative boundary conditions were applied to all sides with the exception of the heated surface, which has direct view of the heating rods and thermal radiation is the dominant mechanism for coupling of the heated surface to the energy source. The silicon rod heater radiation source is idealized as a uniform far field radiation source of time-varying temperature. A PID (proportional-integral-derivative) controller modeling scheme was developed to regulate this radiating temperature to simulate the specified temperature history in the lid of the can [47].

All parameter values used to model the FIC experiments were determined from independent laboratory-scale experiments. These experiments were discussed in detail previously [3], [4], [7]. Values for the foam specific heat and foam bulk thermal conductivity were obtained from published reports. The data for PMDI foam specific heat (Table 5) as well as the data for bulk thermal conductivity (Table 6) were taken from Taylor et al. [48]. Data for bulk conductivity given by Neet [49] and Jinn et al. [50] were similar. The value used for ρ_c^0 (density of initial polymer matrix) was estimated to be about 1500 kg/m^3.

Table 5: PMDI Foam Specific Heat.

Temperature (K)	50	296	323	373	423	473	523	>523
Specific Heat (J/kgK)	1269	1269	1356	1497	1843	1900	2203	2203

Table 6: PMDI 320 kg/m^3 Foam Bulk Thermal Conductivity

Temperature (K)	Conductivity (W/mK)
300	0.049
523	0.071
Temp. > 523	0.071

The effective conductivity k_e for radiant heat transfer in the initial foam, denoted by k_e^0 was based on values of the absorption and scattering coefficients [51] that were determined using an integrating sphere apparatus to measure transmittance and reflectance in unreacted foam and an analytical two-flux representation for radiative transfer [52]. Because a vapor space develops between the heated plate and the reacting foam in the container, the expression for k_e in Eq. 7 was modified to mimic an increased radiation contribution during foam decomposition. The resulting expression is:

$$k_e = k_e^0 / f_{rxn} \qquad 10$$

Where k_e^0 is the effective conductivity for radiative heat transfer in the unreacted PMDI-based foam and f_{rxn} is the progress of the reaction. k_e^0 is defined as:

$$k_e^0 = \frac{16}{3\beta_R}\sigma T^3 \qquad 11$$

where β_R is the Rosseland-mean extinction coefficient, σ is the Stefan-Boltzmann constant, and T is the temperature. In this case, the β_R used is 1990 mK.

f_{rxn} is defined as follows: if $CO_2 \leq 0.1$:

$$f_{rxn} = FOAMA(t) + FOAMB(t) + FOAMC(t) + CO_2(t) + Char(t) \qquad 12$$

And if $CO_2 > 0.1$:

$$f_{rxn} = FOAMA(t) + FOAMB(t) + FOAMC(t) + Char(t) \qquad 13$$

3. NO FLOW MODEL

A validation and uncertainty quantification study was conducted in order to determine if the No Flow model (described in the previous section) would be appropriate to model the PMDI polyurethane FIC problem. To do this, a 3-D finite element model composed of tetrahedral elements was evaluated in the Sierra Thermal/Fluids [16] radiation-conduction code to computationally simulate the FIC experimental configuration (Figure 12).

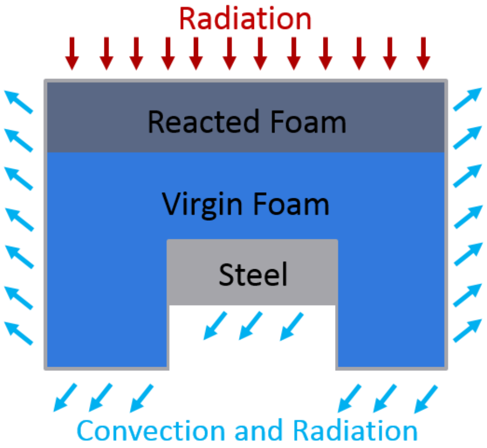

Figure 12: Schematic of the No Flow model

As described in the previous section, the model solves the heat conduction equation with effective conductivity and foam porosity as a function of reaction. The other material properties were constant or a function of temperature. A three-step reaction mechanism reacts PMDI polyurethane foam from into carbon dioxide, light and heavy molecular weight organics, and char. Pressurization is calculated using the ideal gas law, with the assumption that gradients relax quickly. A radiative boundary condition is used to heat one end of the can, while convection and radiation cool the remaining surfaces.

A 3-D model was used to simulate these experiments for two reasons. First, there is no axis of symmetry due to the presence of the vent tube. Second, since this work is validating a foam model that will be used in system level simulations, it is useful to know how the model behaves in 3-D, for example, in relation to wall clock simulation time. The computational model was them compared to the experimental data presented in Chapter 2.

While validation can be conducted by comparing nominal computational results to the experiment, it is more rigorous to perform an uncertainty quantification (UQ) study. In a UQ study, input parameters that one is uncertain of are perturbed, and the effect of the response is measured. An example of this is a heat transfer problem where the conductivity is the parameter and the temperature is the response. By varying the parameters, uncertainty bounds are created. These can be interpreted in a similar as the error in experimental data. The parameters that were examined in this study include material properties and boundary conditions. Specifically, these were: the thermal conductivity and specific heat of the stainless steel and foam; stainless steel emissivity; density of the foam; activation energy of the decomposition reaction; temperature of the heated surface; convective heat transfer coefficient; and the far field temperature.

This section presents the methodology and results for the validation of the No Flow model including the mesh resolutions study, the methodology behind propagating the uncertainty (the mean value method), and finally the comparison of experiment to simulation.

After the validation was performed, a new functionality was implemented which allowed for the inclusion of radiation enclosures. The last section of this chapter will present the No Flow model with the addition of radiation enclosure.

3.1. Mesh Resolution Study

When performing any computer analysis of partial differential equations, the continuous mathematical problem must be converted into a discrete representation. Doing so requires the generation of a mesh, which discretizes the continuous model into finite elements, for solving and storing the approximate solution. An unavoidable consequence is that information is lost relative to the original continuous problem, resulting in numerical discretization error. The quantification of the sensitivity of the solution to the mesh size is accomplished through a mesh resolution study involving a family of topologically similar meshes with a range of characteristic length scales. The finest mesh in the set is considered to be the 'true' solution, because as the mesh size decreases, the mesh-based approximations to the continuous derivatives also improve. When the coarser meshes are compared to the 'true' solution, the error associated can be assessed.

A mesh resolution study is performed to ascertain the effect of the mesh on the solution of the problem using the methodology presented in Scott *et al.* [53]. The mesh with 1024 times as many elements as the coarsest mesh was taken as the 'true' solution because it was the most refined mesh generated. As it is not actually the true mathematical solution, mesh convergence can only be assessed in the Cauchy sense, as discussed in Hughes [54]. Thus, the rate of convergence can be identified, but the difference between the nominal and 1024 mesh only provides an estimate for the absolute difference between the numerical results and analytic solution. Two standard norms were used to assess the rate of convergence: the L_2 and L_∞ norms. The L_∞ norm is the absolute maximum difference between the two solutions, also normalized by the fine mesh. For the temperature, the norm is mathematically defined as (in 1D):

$$L_\infty = \lim_{n \to \infty} \frac{\left(\int_\Omega \left(T_F(x) - T_C(x)\right)^n dx\right)^{1/n}}{\left(\int_\Omega T_F^n(x)\, dx\right)^{1/n}} \qquad 14$$

where Ω is the domain, $T_F(x)$ is the temperature of the fine mesh at location x and $T_C(x)$ is the temperature of the course mesh at location x. The L_∞ norm is expected to converge as h^{-1}, where h is the mesh length scale. It provides a measure of the worst-case local error that can occur and is useful for verifying that lower dimensional parts of the mesh are accurate, such as faces and contacts. In contrast, the L_2 norm measures the mean square error between two solutions, normalized by the fine mesh, and is expected to converge as h^{-2}. It is useful for assessing the overall quality of the solution.

Solution trends are presented in Figure 13a showing a comparison of the temperature fields at a location of interest for three different mesh resolutions. Although only one location is shown, all the temperature measurements converged in a similar manner. While Figure 13a qualitatively indicates convergence, the L_2 and L_∞ norms shown in Figure 13b quantitatively proves it. According to Hughes [54], when plotted on a log-log scale, the slope of the best fit lines in this figure should be -1 for L_∞ and -2 for L_2 to show convergence. The series of tested meshes have an L_2 convergence rate of -1.76 and a L_∞ convergence rate of -0.83, which is close to the theoretical expected values in [54]. Based on the results, it was determined that a mesh with an element edge length of approximately 2mm (or 16 times more elements than the coarsest mesh) was optimal, since it is within the linear convergence regime, but at the coarse end, allowing for shorter computation times.

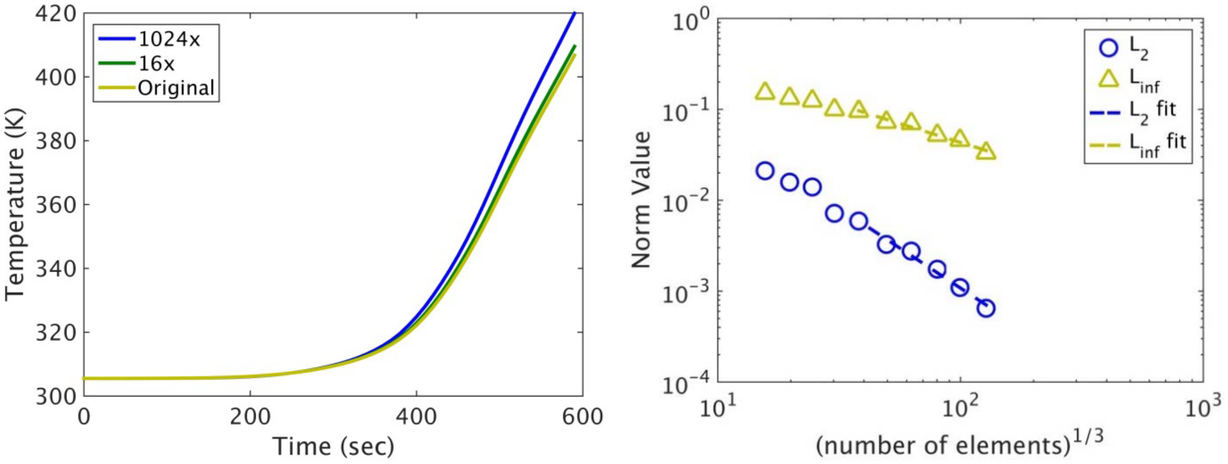

(a) (b)

Figure 13: Mesh resolution study results: (a) temperature vs time of the embedded mass for the original (coarsest) mesh and for the 32x and 1024x more elements than the original mesh and (b) L_2 and L_∞ norms with best fit lines (L_2 best fit slope = -1.76 (R^2 = 0.99), L_∞ best fit slope = -0.83 (R^2 = 0.97)).

3.2. Mean Value Method

The mean value method is one of the methods used to propagate uncertainty through the model. This approach requires input of gradients of the response functions (*i.e.* temperature, pressure) with respect to the input parameters (*e.g.* thermal conductivity of the foam). In other words, each input parameter is perturbed in order to understand the effect of the perturbation of the response. The advantage of this method is that $2n+1$, where n is the number of parameters, simulations must be run to complete the study. However, since the formulation assumes a linear response, this method is only acceptable for a subset of problems. For this study, processing of the input files and the responses was performed using Microsoft Excel and a series of MATLAB [55] and Python scripts [56].

Let a vector representing mean values of N normalized parameters of interest to the problem be defined as $\bar{P}$ so that each parameter (P_i) is dimensionless and of unit value when it is at its expected value. A vector of M responses, defined as $\bar{R}$, represents the responses of the simulation. For the current effort, responses are measured temperatures and the pressure. All of the parameters (P) are constant through a model run and the responses are all functions of time. In the case of temperature dependent properties, parameters are applied as a multiplier on the nominal value, i.e., thermal conductivity, $k(T) = P_k k_{nom}(T)$. The sensitivity of the j^{th} response to the i^{th} parameter is estimated by central differencing as:

$$\frac{\partial R_j}{\partial P_i} \approx \frac{R_j\{\bar{P} + \delta P_i\} - R_j\{\bar{P} - \delta P_i\}}{2\delta P_i} \qquad 15$$

Where $R_j\{\bar{P} + \delta P_i\}$ and $R_j\{\bar{P} - \delta P_i\}$ represent the j^{th} responses for the system with the i^{th} parameter incremented up by δP_i and down by δP_i respectively, where δP_i is the perturbation of the parameter. As P_i is dimensionless, the sensitivity has the same units as the corresponding response variable. For example, if the response is temperature (K), its sensitivity with respect to a (dimensionless) parameter is the change in temperature (K) per fractional change in the parameter. Estimates of the standard deviations of the parameters are represented by the vector, defined as $\bar{\sigma}$. The variance for the system response considering all the parameter uncertainties is estimated as:

$$\sigma_{R_j}^2 = \sum_{i=1}^{N} \left(\frac{\partial R_j}{\partial P_i} \sigma_i \right)^2 \qquad 16$$

Dividing by $\sigma_{R_j}^2$ gives a relative contribution of each parameter to the variance such that:

$$I_{ij} = \left(\frac{\partial R_j}{\partial P_i} \frac{\sigma_i}{\sigma_{R_j}} \right)^2 \qquad 17$$

is the *importance* of the i^{th} parameter to the j^{th} response. The input parameter variation used in the mean value method is shown in Table 7. Most of the values came from engineering judgment. However, the activation energy was determined through bounding the experimental TGA data. The activation energies were all varied together as to shift the entire reaction mechanism. The pre-exponential factors were not changed as the activation energy and pre-exponential factors are linked and should not be simultaneously changed in this type of study. The uncertainty in the foam density is associated with accuracy of measuring mass of the foam. All other parameters, are held constant, either because they were not used in the calculation, such as foam emissivity, or their variation was already accounted for, such as steel density (since the specific heat was varied).

Table 7: Input parameters used in mean value method

Input parameter	σ_i	δP_i	Input parameter	σ_i	δP_i
Foam Conductivity	0.1	0.1	Steel Conductivity	0.1	0.1
Foam Specific Heat	0.1	0.1	Steel Specific Heat	0.1	0.1
Foam Density	0.01	0.01	Steel Emissivity	0.1	0.1
Foam Activation Energy	0.02	0.02	Convective heat transfer coefficient	0.2	0.2
Far Field Temperature	0.05	0.05	Temperature of heated surface	0.01	0.01

3.3. Comparison of model and experiments

3.3.1. 150 C/min

The computational model results with mean value generated uncertainties and the experimental results for select thermocouples and for pressure in both orientations are compared in Figure 14 and Figure 15. These results are shown with $\pm 2\sigma_R$ propagated uncertainty for the computational results and ±2% error for the experimental results. Figure 14 and Figure 15a show generally good agreement between the computational and experimental results, especially for thermocouples farther from the heated surface. For the locations closer to the heated surface, the model slightly over predicts the experimental response. In these simulations, a constant convective heat transfer coefficient was used for all locations. Using a temperature dependent value could potentially alleviate this mismatch. In addition, the thermal model geometry has been simplified such that there is no gap between the lid of the stainless steel can and the walls. There is a weld in this region, but there is also potential for a gap and contact resistance between portions of these surfaces.

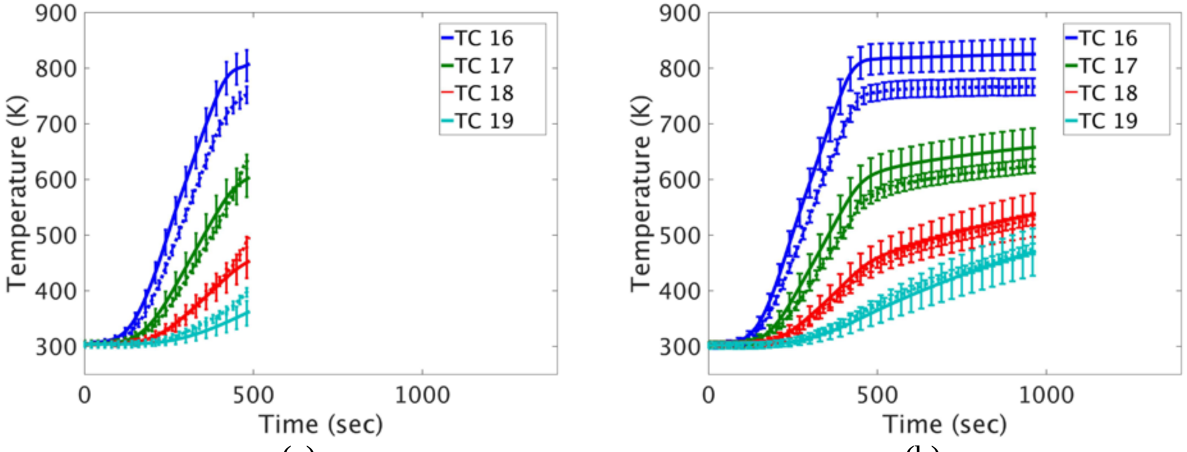

(a) (b)

Figure 14: Computational results (solid) with $\pm 2\sigma_R$ uncertainty and experimental results (dashed) with ±2% error for the exterior side thermocouples temperature vs time in the (a) inverted and (b) upright orientations.

Figure 15b shows the inverted and upright experimental and model pressure responses. Since there are no gravity dependent physics in this model, there is no difference between the upright and inverted model's response. In addition, neither the upright nor inverted pressure response predict the slope change seen in the experiments at approximately 400 seconds.

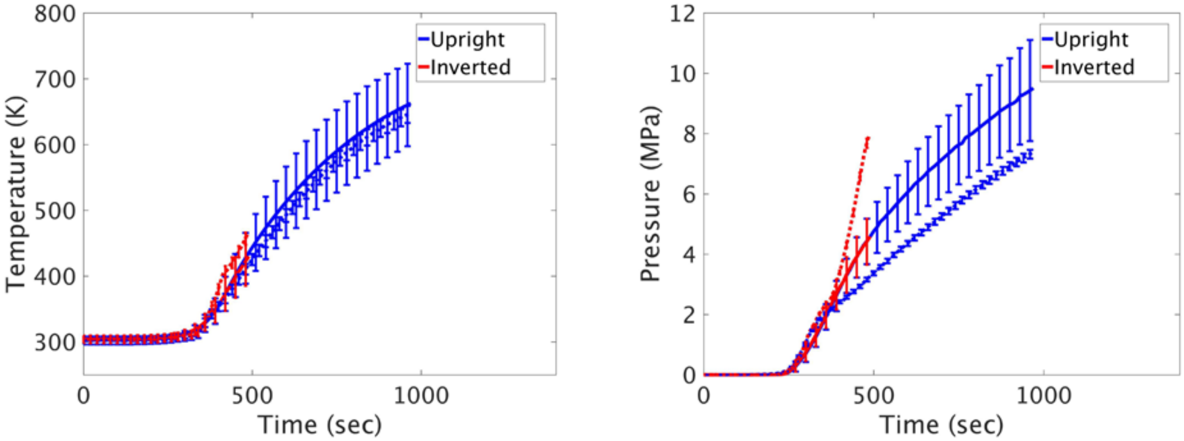

(a) (b)

Figure 15: Inverted and upright computational results (solid) with ±2σ_R uncertainty and experimental results (dashed) with ±2% error for (a) temperature vs time for TC 25 and (b) pressure vs time.

The model under predicts the pressure response in the inverted case and over predicts the pressure response in the upright case. The assumption that all of the decomposition products reside in the gas phase and that all of the volume in both the reacted and unreacted pore space is available to the gases may contribute to these issues. In addition, since the model does not take gravity into account, there is fundamentally no difference between the upright and inverted simulations, except for the heating boundary condition (since that matches the individual experiment). These assumptions do not differ between models, and as a result, the predictions are very similar between the upright and inverted simulations. Excluding physics such as the flow of gas and liquid decomposition products and the distribution of decomposition products between the gaseous and liquid phases lead to the lack of accurate prediction.

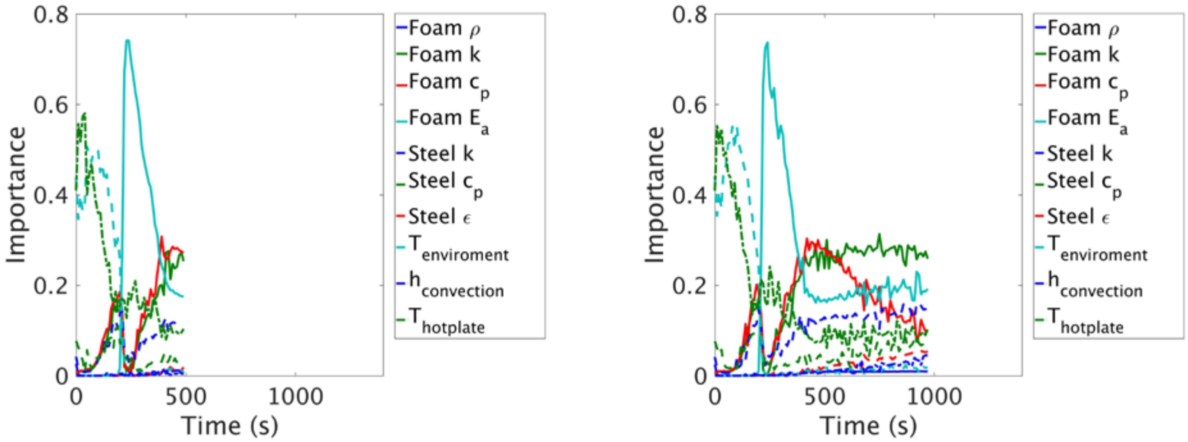

(a) (b)

Figure 16: Parameter importance vs time for pressure for (a) inverted and (b) upright.

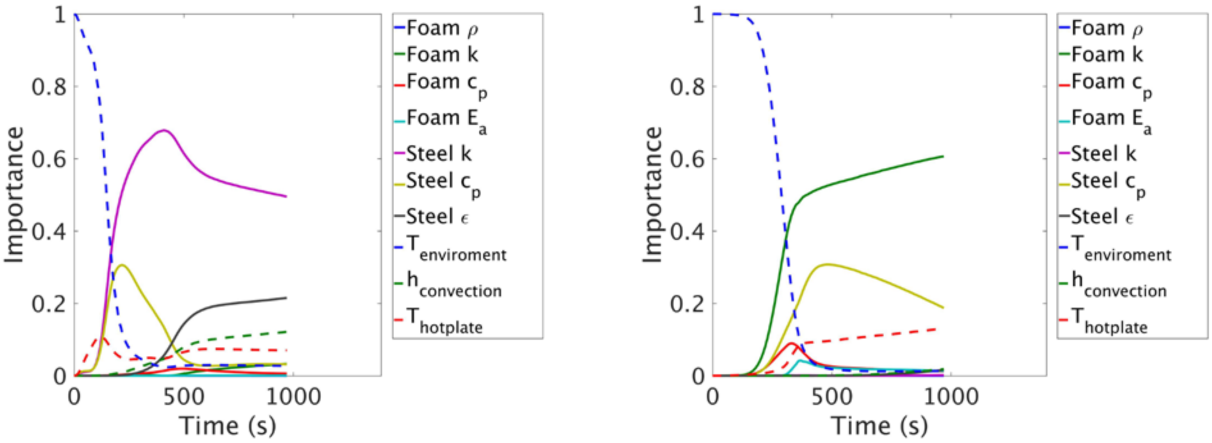

(a) (b)

Figure 17: Parameter importance vs time for (a) TC 17 and (b) TC 25 for the inverted configuration.

By investigating sensitivity for each input parameter for a given response, the effect of uncertainty in the value of that parameter on the simulation results can be quantified. The results of this analysis show that the dominant importance factor is also dependent on the model response that is being investigated. When measuring the response of pressure (Figure 16), the activation energy for foam decomposition followed by the conductivity and specific heat of the foam dominates the importance factors. This was true in both the upright and inverted cases. When measuring the response of temperature on the outside of the can (Figure 17a) the conductivity of steel is dominant followed by the specific heat of the steel; while for the embedded object (Figure 17b) it is the effective conductivity of the foam followed by the specific heat of the steel for both the inverted and upright cases, although only inverted are shown. For both thermocouples and the pressure response, early in time, the temperature of the environment is dominating because the flow of heat from the heated surface has not yet reached the location of interest or pressure has not begun to increase yet.

3.3.2. 50 C/min

The computational model results with uncertainties and the experimental results for temperature and pressure in both orientation are shown in Figure 18 and Figure 19. As with the faster heating rate, these results show generally good agreement between the computational and experimental results for the thermocouples along the side of the can. Again, the model over predicts nearer the heated plate, for the same reasons as previously discussed.

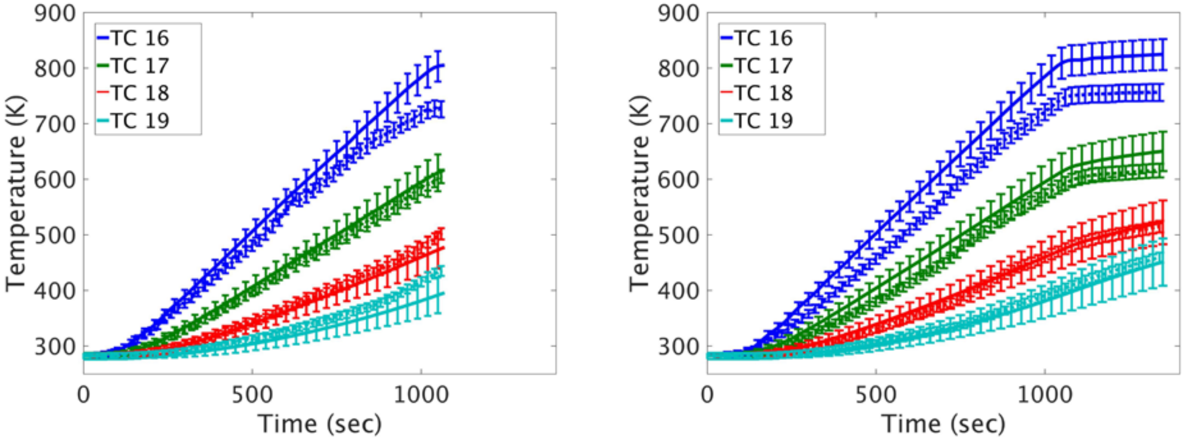

(a) (b)

Figure 18: Computational results (solid) with ±$2\sigma_R$ uncertainty and experimental results (dashed) with ±2% error for the exterior side thermocouples temperature vs time in the (a) inverted and (b) upright orientations.

Figure 19a shows the temperature on the slug. The model under predicts the temperature in the inverted orientation and does not capture the slope change that occurs at approximately 700 seconds. Since the model predicts the upright temperature well, it is likely that heat transfer is due to advection. This could be due to higher gas velocities, driven by buoyant flow, increasing the rate of convective heat transfer. Another possibility is that the hot gases are condensing on the cooler slug, and increasing its temperature through this mechanism. Figure 15b (150 C/min) shows a similar difference between the upright and inverted, but not nearly as exaggerated as seen at the lower heating rate.

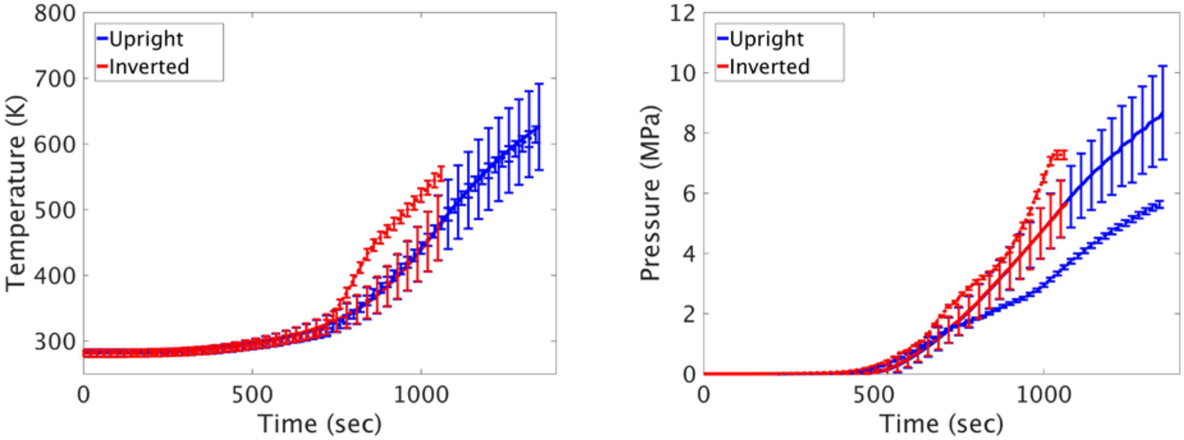

(a) (b)

Figure 19: Inverted and upright computational results (solid) with ±$2\sigma_R$ uncertainty and experimental results (dashed) with ±2% error for (a) temperature vs time for TC 25 and (b) pressure vs time.

The pressures shown in Figure 19b are similar to those shown in the faster heating rate. Again, the model shows no differentiation between upright and inverted, landing between the two experimental results. The parameter importance for the simulation is shown in Figure 20 and

Figure 21. The results are similar to the faster heating rate: the activation energy is most important to the pressure; the steel conductivity is most important for the thermocouples on the outside of the can; and the effective conductivity of the foam is most important for the embedded object.

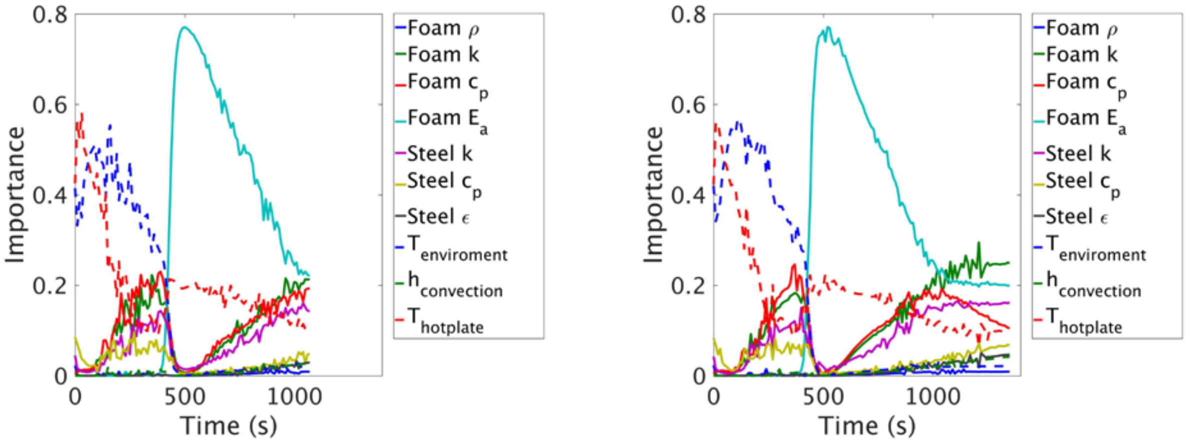

(a) (b)

Figure 20: Parameter importance vs time for pressure for (a) inverted and (b) upright.

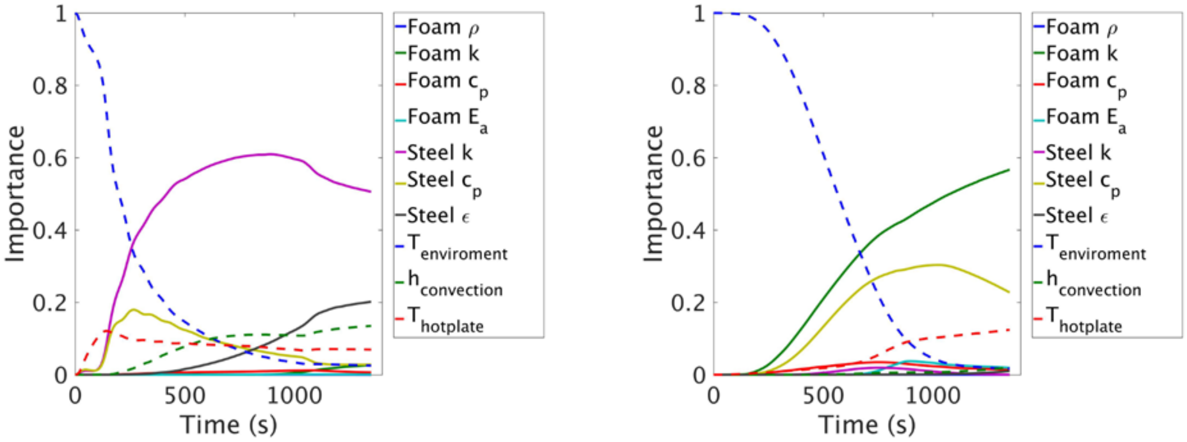

(a) (b)

Figure 21: Parameter importance vs time for (a) TC 17 and (b) TC 25 for the upright configuration.

3.4. Addition of enclosure radiation

3.4.1. Description of interface tracking method

The objective of this model is to incorporate interface tracking and enclosure radiation to better model radiative heat transfer through regions where the foam has fully decomposed and not left a stable char behind. To achieve this, an interface tracking method was used to divide the foam volume and to create a radiation enclosure. In the enclosure, it is assumed any material in that area is optically thin and a viewfactor based enclosure radiation calculation is used to model radiative heat transport between the exposed surfaces of the surrounding can and the foam on the other side of the enclosure. For the foam that remains outside the enclosure, the radiation-diffusion approximation is used. The inclusion of the radiation enclosure and the removal the diffusion approximation within the decomposed foam are the only difference between this and the previously discussed No Flow model.

In order to track the foam decomposition front, the conformal decomposition finite element method (CDFEM) [31], [57] implemented in the Sierra Thermal/Fluids radiation-conduction code is used. In CDFEM an isosurface of a nodal field is used to define the position of the interface, and the finite element mesh is locally refined to create faces that conform to that interface. A simple example of this refinement process is depicted in Figure 22. The most physically justifiable interface definition for this problem would be to choose a threshold based on extent of the decomposition reaction. Unfortunately, the model implementation solves the reaction ODEs at the integration points of the finite elements, and as a result there is no nodal field to use for the interface definition. Instead this work defines the interface based on the temperature field as the isosurface where $T = T_{decomp}$. The threshold temperature is used as a fitting parameter. The radiation enclosures also introduce the issue of the emissivity of the interior of the can and of the decomposed foam. Since neither of these is known, a range of parameters is explored.

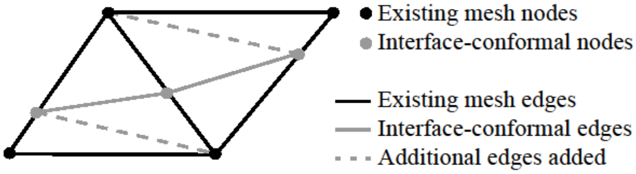

Figure 22: Example decomposition of two linear triangle elements using CDFEM. Additional nodes are added at the interface location on the existing mesh edges. Interface edges are then added to connect the new nodes and create a surface that boundary conditions may be applied to. Finally, edges are added to divide any quadrahedra back into triangles.

3.4.2. Results

The inverted 50 C/min inverted experiment was modeled using a foam threshold temperature of 600 K. A comparison of the computational and experimental results is shown in Figure 23 and Figure 24. As seen in Figure 23a, along the sides of the can, the model over predicts the experiment closest to the heated surface. There are several possible reasons for this. First, there is no contact resistance anywhere in the model. Second, the convective coefficient is constant for the entire side of the can, whereas in reality it varies with temperature. Finally, in the x-ray images it can be seen that there is a significant amount of pooling of liquid decomposition products as well as motion of gases. This would alter the heat transfer from the radiation-conduction model that was used and disproportionally affect the temperature nearer the heated surface.

Figure 23b compares temperatures on the embedded object between the experiment and simulation. The model predicts the temperature of the embedded object well, however it does not capture the slope changes at approximately 800 and 900 seconds. These slope changes are most likely due to unmodeled physics, such as the liquid decomposition products and gas phase motion.

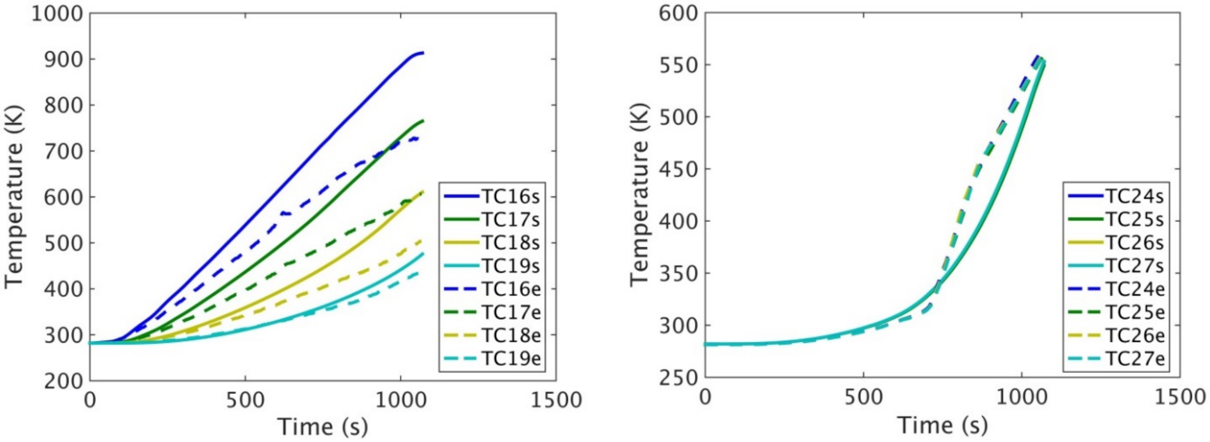

(a) (b)

Figure 23: Comparison of simulations (s) and experiment (e) for (a) one set of thermocouples on the side of the can and (b) the embedded object.

The pressure response for the experiment and simulation are shown in Figure 24. Similar to the embedded object, the model predicts the pressure response relatively accurately. However, the slope changes, such the one seen at approximately 800 seconds, are not predicted by the model.

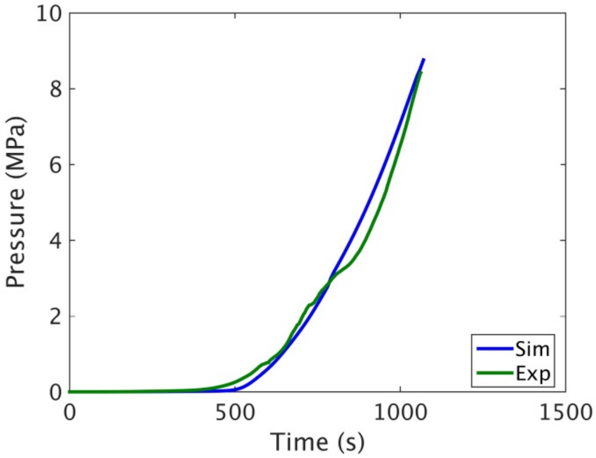

Figure 24: Comparison of pressure for simulation and experiment

While the exact threshold temperature is unknown, Figure 25, does inform a range of temperatures for this value. TGA experiments previously conducted at Sandia National Laboratories shows that the sample begins losing mass at around 550 K and finishes at approximately 750 K.

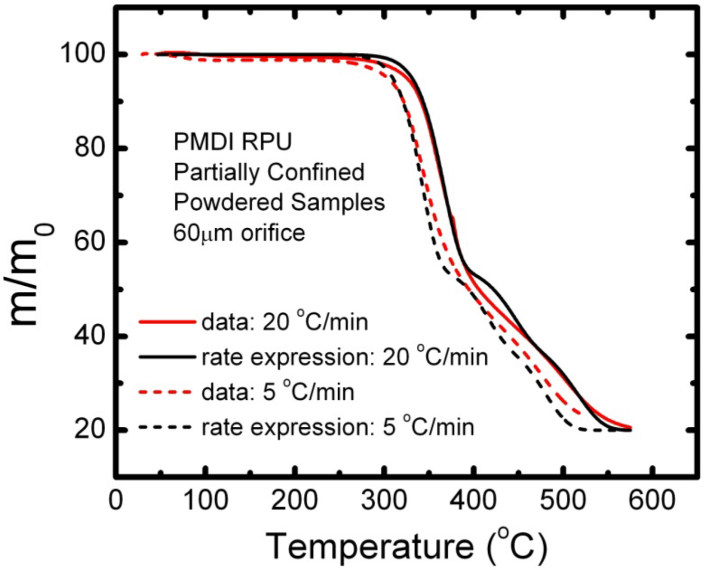

Figure 25: Mass loss versus temperature for PMDI from TGA experiment

Simulations with the threshold temperature set at 550 K and 650 K (which coincides with the first slope change) were also run in order to understand the effect this would have on the result. Figure 26 and Figure 27 show the results of the three threshold temperatures, the standard No Flow model (labeled NoCDFEM), and the experiment. Figure 26a and b, which show thermocouples along the side of the can, show that the threshold temperature does not have a large effect on the temperature response (the traces lie on top of each other such that only the 650K is visible on the plot). However, including the enclosure radiation has a large response when compared to the baseline model. In the case of TC 16 (which is closest to the heated surface) the addition of the radiation enclosure causes an increase in the model's over prediction. Figure 26b shows the inclusion of the radiation enclosure for thermocouple 19 (furthest from the heated surface) is an improvement over the baseline model, even though it over-predicts.

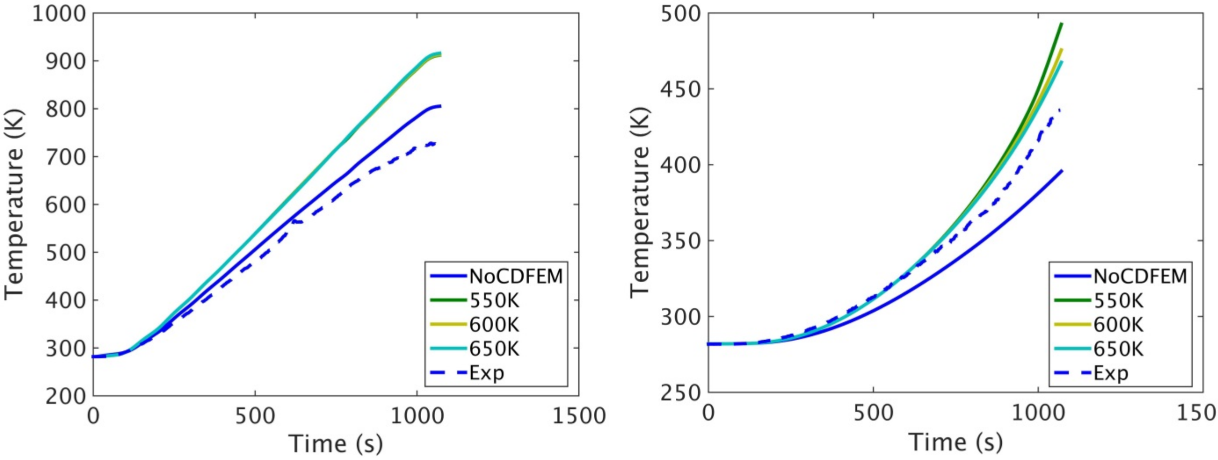

(a) (b)

Figure 26: Comparison of three CDFEM threshold temperatures (550K, 600K, 650K), the simulation without CDFEM, and the experiment for (a) TC 16 and (b) TC 19.

Figure 27a shows the temperature response for a thermocouple on the embedded object. Threshold temperature has a stronger effect on this response than the thermocouples on the sides of the can.

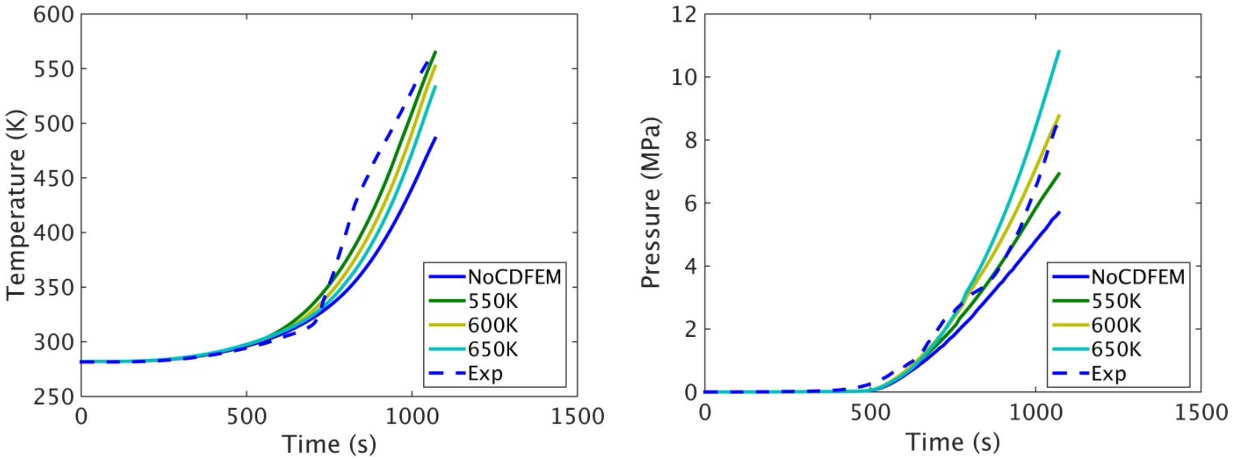

(a) (b)

Figure 27: Comparison of three CDFEM threshold temperatures (550K, 600K, 650K), the simulation without CDFEM, and the experiment for (a) TC 25 and (b) pressure.

Pressure showed the largest response to altering the threshold temperature, as shown in Figure 27b. As the threshold temperature increases, so does the pressure response for a given point in time. This is most likely happening because the heat transfer through the high temperature region is reduced (due to the removal of the radiation contribution to the conductivity through the diffuse approximation) causing the reaction to occur slower.

In order to better understand which temperature best follows the decomposition front, visualization of the experiment and of the simulations are compared. In Figure 28 and Figure 29 the experiment and simulation are compared at 630 seconds. Qualitatively, the 650 K decomposition temperature most accurately predicts the location in of the front. Figure 30 and Figure 31 show the same information, but at 780 seconds. Again, 650 K most accurately places the front.

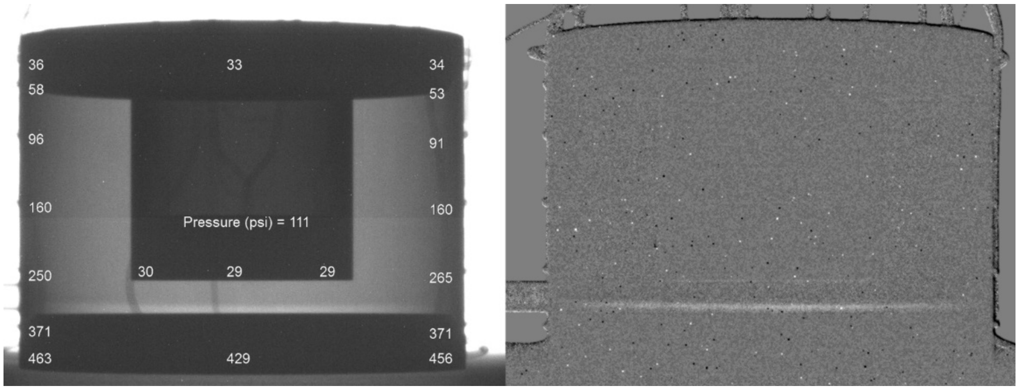

Figure 28: X-Ray image of experiment after 630 seconds showing the foam receding from the heated plate.

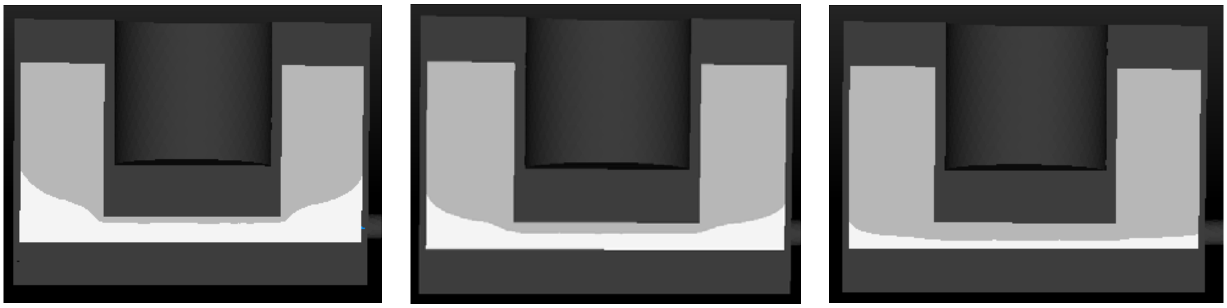

(a) (b) (c)

Figure 29: Cross-section of simulation after 630 seconds showing the foam receding past the embedded object when the threshold temperature is set at a) 550 K b) 600 K and c) 650 K. The darker gray represents the low temperature region and the lighter grey the high temperature region.

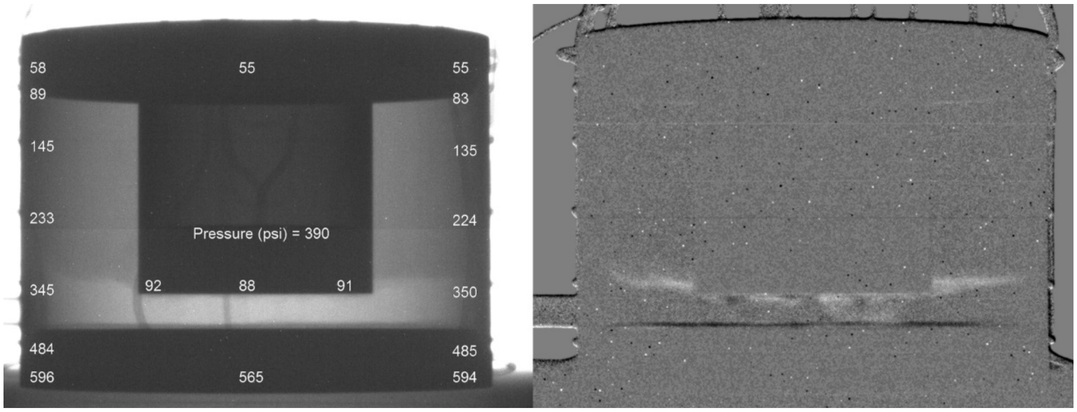

Figure 30: X-Ray image of experiment after 780 seconds showing the foam receding past the embedded object.

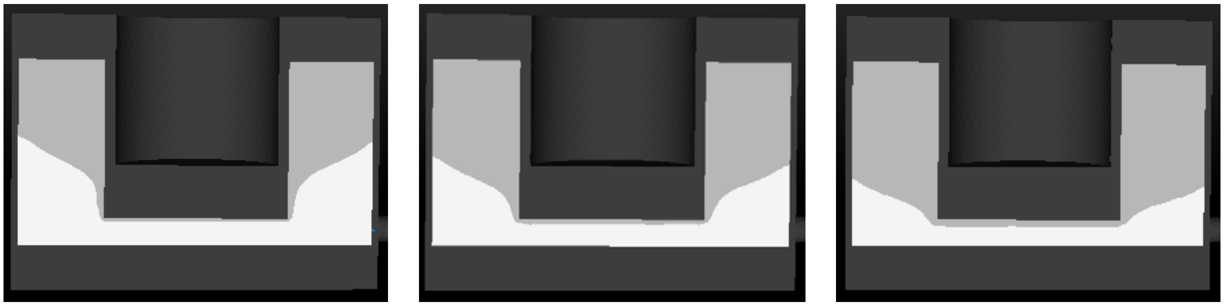

(a) (b) (c)

Figure 31: Cross section of simulation after 780 seconds showing the foam receding past the embedded object when the threshold temperature is set at a) 550 K b) 600 K and c) 650 K. The darker gray represents the low temperature region and the lighter grey the high temperature region.

One interesting side effect of using temperature rather than extent of reaction to create the radiation enclosure is that, if the temperature used is not the decomposition temperature, the enclosure can move in front of or behind the actual front. Figure 32 show the percent of CO_2 as a measure of extent of reaction for a decomposition temperature of (a) 600 K and (b) 650 K with (c) a comparison to the No Flow model. The radiation surface is also drawn on to (a) and (b), showing again that the 650 K decomposition temperature agrees well with the actual decomposition front.

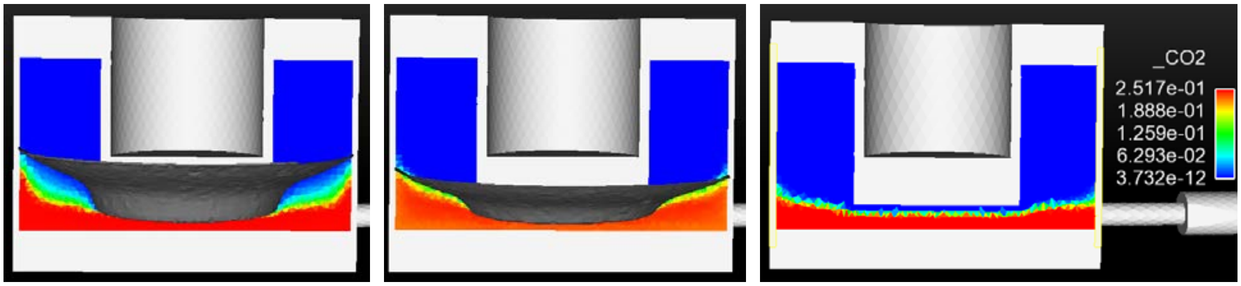

(a) (b) (c)

Figure 32: (a) 600 K (b) 650K threshold temperature simulation after 780 seconds showing the percentage of CO_2 with the decomposition surface drawn over the cross section of the FIC and (c) baseline simulation.

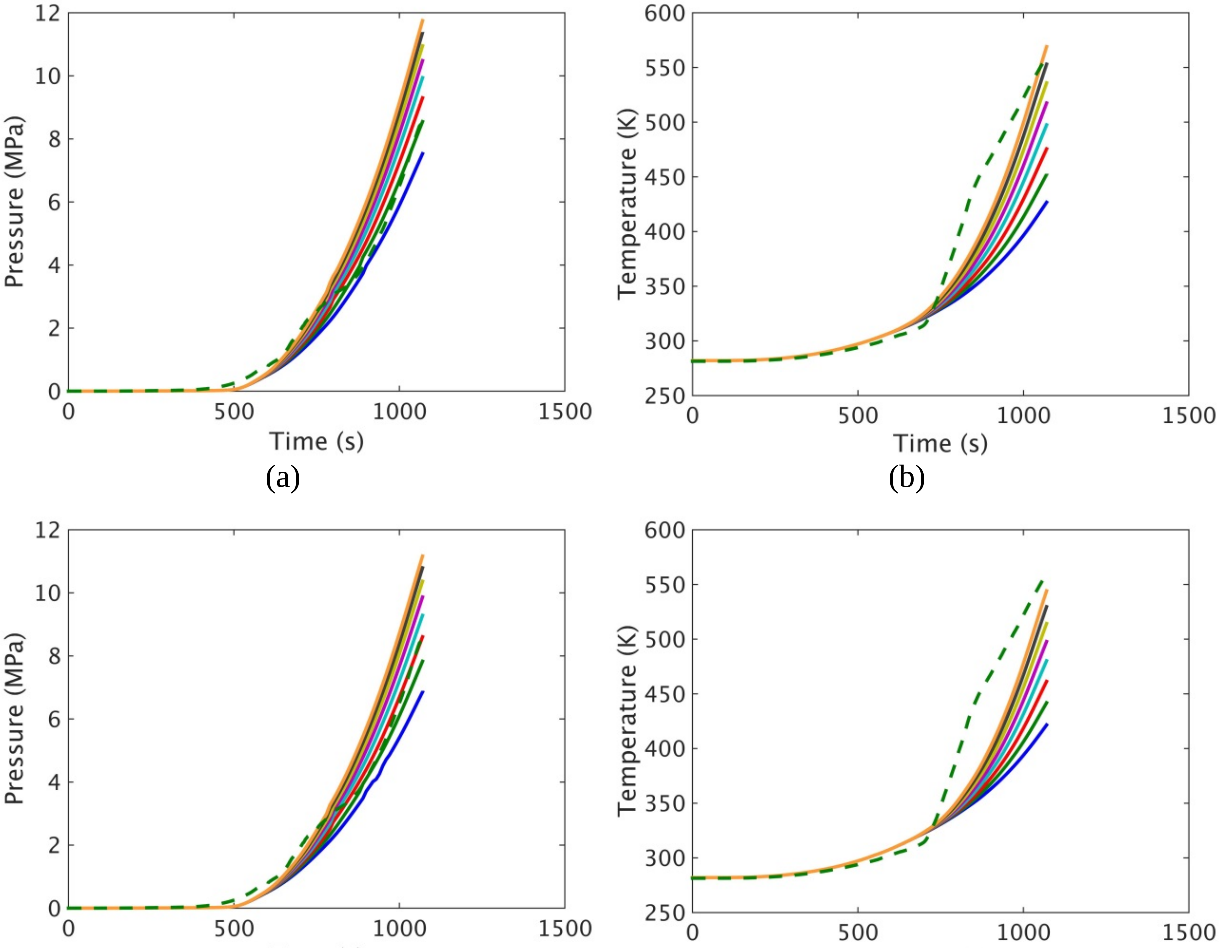

(a) (b)

(c) (d)

Figure 33: Comparison of pressure, (a) and (c), and temperature, (b) and (d), for varying emissivity (ranging from 0.2, the blue line, to 0.9, the gold line, in increments of 0.1) for the can in (a) and (b) and the foam in (c) and (b). Each results is compared with the experiment (green dashed)

One of the issues with included the radiation enclosure is that the emissivity of the can and the foam must be known. This is difficult because the decomposing foam leaves a residue behind on the can, which may change its emissivity. Also, the emissivity partially decomposed, possibility liquefied foam, is also unknown. Thus a range of emissivities were explored in order to understand how this parameter would affect the responses of interest, primarily the pressure and the temperature of the slug. Figure 33a shows the change in pressure when the emissivity of the can is varied between 0.2 and 0.9 and Figure 33b shows the change in temperature on the slug for the same rage of emissivities. Figure 33c and d show the same information, but this time varying the emissivity of the foam while the can is held constant. The result is similar in both cases; the final pressure changes approximately 5 MPa and the final temperature about 150 K over the range of emissivities investigated. This suggests that in future work, the actual quantity of these parameters should be further investigated.

3.5. Remarks

Pressure and temperature responses from a computational model and experiments were examined for the Foam in a Can apparatus. Uncertainties in input parameters for the model were propagated through the simulation using the mean value method. While the computational and experimental results agreed well for most cases, in the inverted case, the rate of pressurization in the experiments increases drastically near the end of the test, a response not seen in the model. Since the model does not explicitly consider the gravity-induced movement of gaseous or liquid products of decomposition, it does not differentiate between the inverted and upright orientations. However, the experiments do show a change in the pressure response based on orientation. In order to properly predict these trends, additional physics needs to be included in the model.

In an attempt to explore missing physics in the model, radiation enclosures were added to the standard No Flow model. However, this inclusion did not help the model capture slope changes in the pressure and temperature traces. In addition, it added in two additional unknowns: the decomposition temperature and the emissivity of the foam and the can. It was shown that the pressure and temperature response were both sensitive to these parameters, making it increasingly problematic that they are unknown.

Since the radiation enclosures did not improve qualitative agreement to the experiments, this would seem to indicate that a model that includes fluid motion and convective heat transfer involving both gas-vapor and liquid phases would possibly be a more beneficial path forward. The next two chapters will examine such models.

4. POROUS FLOW MODEL

In the previous chapter, the No Flow model was compared to experimental results for Foam in a Can. Since gravitational effects clearly play a differentiating role in the pressure and temperature results – one not captured by the No Flow model – a new model was implemented. The Porous Media model uses Darcy's law to calculate the gas velocity through the virgin and decomposed foam.

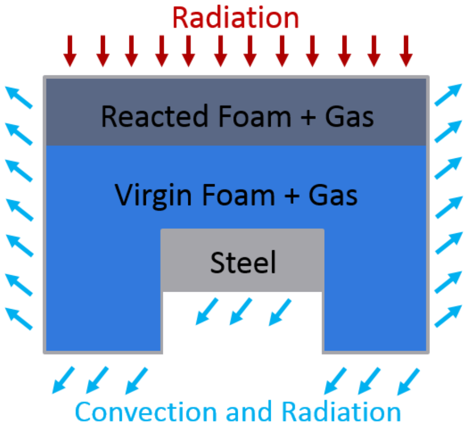

Figure 34: Schematic of the Porous Media model

A 3-D finite element model composed of tetrahedral elements was evaluated in the Sierra Thermal/Fluids [16] radiation-conduction code to computationally simulate the FIC experimental configuration (Figure 34). A three-step reaction mechanism reacts PMDI polyurethane foam into carbon dioxide, light and heavy molecular weight organics, and char. Pressurization is calculated using the ideal gas law. A radiative boundary condition is used to heat one end of the can, while convection and radiation cool the remaining surfaces. Foam effective conductivity, porosity and permeability are a function of reaction while other properties are constant or a function of temperature. The continuity, species, and enthalpy equation are solved in both the condensed and gas phases. The following section will give a detailed description of the model.

4.1. Description of model

The Porous Media model approach assumes that the whole can is filled with foam and that there are two phases, the condensed phase and the gas phase. The foam has a certain porosity, which is a function of reaction. In the gas phase, Darcy's law is used to approximate the flow of the fluid and the continuity, species, and enthalpy equations are solved. In the continuity equation, density is related to pressure through the ideal gas law so that the gas pressure can be solved. In the condensed phase the species and enthalpy equations are solved, and the two phases are coupled through a source terms in the species equation and a volumetric heat transfer term in the enthalpy equations. This derivation is based on the model in Lautenberger *et. al.* [15]

The solid phase continuity equation is:

$$\frac{\partial \rho_b}{\partial t} = -\dot{\omega}_{fk}''' \qquad (18)$$

Where ρ_b is the bulk density, and $\dot{\omega}_{fk}'''$ is the formation rate of gas phase mass for the *k^th^* species from the solid phase.

The porous gas phase continuity equation is:

$$\frac{\partial(\bar{\psi}\rho_g)}{\partial t} + \frac{\partial(\rho_g u_{j,g})}{\partial x_j} = \dot{\omega}_{fk}''' \qquad (19)$$

Where $\bar{\psi}$ is the mixture averaged condensed phase porosity, $\rho_g$is the gas density, and $u_{j,g}$ is the velocity of the gas using the Darcy approximation:

$$\bar{\psi} v_{j,g} = u_{j,g} = -\frac{\bar{K}}{\mu_g}\left(\frac{\partial p_g}{\partial x_j} + \rho_g g_j\right) \qquad (20)$$

Where $\bar{K}$ is the mixture averaged solid phase permeability tensor, μ_g is the gas phase viscosity and g_j is the gravity vector. The ideal gas law is used to relate the pressure to the density

$$\rho_g = \frac{\bar{M} p_g}{R T_g} \qquad (21)$$

Where $\bar{M}$ is the mass averaged molecular weight, R is the gas constant, and T_g is the gas temperature. The final porous gas phase continuity equation is then:

$$\frac{\partial}{\partial t}\left(\frac{\bar{M} p_g \bar{\psi}}{R T_g}\right) + \frac{\partial}{\partial x_j}\left(\frac{\bar{M} p_g}{R T_g}\frac{\bar{K}}{\mu_g}\left(\frac{\partial \rho_g}{\partial x_j} + \frac{\bar{M} p_g}{R T_g} g_j\right)\right) = \dot{\omega}_{fk}''' \qquad (22)$$

The condensed phase species equation is:

$$\frac{\partial(\rho_b Y_k)}{\partial t} = \dot{\omega}_{fk}''' - \dot{\omega}_{dk}''' \qquad (23)$$

Where $\dot{\omega}_{fk}''' - \dot{\omega}_{dk}'''$ is the difference between the formation and destruction rates of gas phase mass for the k^{th} species and Y_k is the condensed phase mass fraction of the k^{th} species.

The gas phase species is:

$$\frac{\partial\left(\bar{\psi}\rho_g Y_{k.g}\right)}{\partial t}+\frac{\partial\left(\rho_g u_{j,g} Y_{k.g}\right)}{\partial x_j}=-\frac{\partial q_{k,j}^{Y,g}}{\partial x_j}+\left(\dot{\omega}_{s,fk}'''-\dot{\omega}_{s,dk}'''\right)+\left(\dot{\omega}_{g,fk}'''-\dot{\omega}_{g,dk}'''\right) \tag{24}$$

Where $Y_{k.g}$ is the gas phase mass fraction of the *kth* species, $\left(\dot{\omega}_{s,fk}'''-\dot{\omega}_{s,dk}'''\right)$ is the difference between the formation and destruction rates for heterogeneous reactions and $\left(\dot{\omega}_{g,fk}'''-\dot{\omega}_{g,dk}'''\right)$ is for homogenous reactions. $q_{k,j}^{Y,g}$ is the gas phase species diffusion flux, defined as:

$$q_{k,j}^{Y,g}=-\bar{\psi}\rho_g D_{k.g}\frac{\partial Y_{k.g}}{\partial x_j} \tag{25}$$

Where $D_{k.g}$ is the gas phase mass diffusivity for the *kth* species.

The gas phase enthalpy is:

$$\begin{aligned}&\frac{\partial\left(\bar{\psi}\rho_g h_g\right)}{\partial t}+\frac{\partial\left(\rho_g u_{j,g} h_g\right)}{\partial x_j}\\&\qquad=-\frac{\partial q_{k,j}^{h,g}}{\partial x_j}+\frac{\partial\left(\bar{\psi}p_g\right)}{\partial t}+h_{cv}\left(\bar{T}-T_g\right)+\sum_k\left(\dot{\omega}_{s,fk}'''-\dot{\omega}_{s,dk}'''\right)h_{k.g}\end{aligned} \tag{26}$$

Where h_g is the mixture averaged gas phase enthalpy, h_{cv} is the volumetric heat transfer coefficient, $\bar{T}$ is the porous condensed phase temperature, $h_{k.g}$ is the gas phase enthalpy of the *kth* species. $q_j^{h,g}$ is the gas phase energy diffusive flux and is modeled as:

$$q_j^{h,g}=-\bar{\psi}\rho_g D_g\frac{\partial h_g}{\partial x_j} \tag{27}$$

Where D_g is the mixture averaged gas phase mass diffusivity.

The condensed phase enthalpy is defined as:

$$\frac{\partial\left(\bar{\rho}\rho_g\bar{T}\right)}{\partial t}=-\frac{\partial q_j^h}{\partial x_j}+h_{cv}\left(T_g-\bar{T}\right) \tag{28}$$

Where q_j^h is the condensed phase energy diffusive flux:

$$q_j^{h,g}=-(k+k_e)\frac{\partial\bar{T}}{\partial x_j} \tag{29}$$

Where k is the thermal conductivity and k_e is the effective conductivity for radiant heat transfer in optically thick media.

4.1.1. PMDI Parameter Specification

The formation rate of gas phase mass for the k^{th} species, $\dot{\omega}_{fk}'''$, follows reaction scheme in Table 8.

Table 8: Decomposition reaction scheme.

Initial Foam $0.45\,FOAMA + 0.15\,FOAMB + 0.4\,FOAMC$	Reaction $\rightarrow$	Decomposition Products
FOAMA	$\dot{\omega}_{f1}'''$	$0.56\,CO_2 + 0.44\,Organic\,Vapors$
FOAMB	$\dot{\omega}_{f2}'''$	$Organic\,Vapors$
FOAMC	$\dot{\omega}_{f3}'''$	$0.5\,Organic\,Vapors + 0.5\,Char$

The reaction rates for this problem are first order Arrhenius, therefore:

$$\dot{\omega}_f''' = -\frac{d(FOAM)}{dt} = k\,FOAM(t) = k^0 \exp\left(\frac{-Q}{RT}\right) FOAM(t) \qquad 30$$

Where $FOAM(t)$ is the fraction of $FOAM$ remaining at time *t* and $FOAM$ can be $FOAMA$, $FOAMB$, or $FOAMC$.

Table 4, Table 5, and Table 6 in Chapter 2 give the values for the reaction properties and specific heats.

The effective conductivity for radiative heat transfer is defined as:

$$k_{e,i} = \frac{16}{3\beta_{R,i}} \sigma T^3 \qquad 31$$

Where $\beta_{R,i}$ is the Rosseland-mean extinction coefficient, σ is the Stefan-Boltzmann constant, and T is the temperature. The effective conductivity is volume averaged on an element basis to change it as the foam decomposes. For PMDI, the β_R used is 1990 mK for the unreacted foam. β_R for the char will be discussed in the Parameter Calibration section.

As with the No Flow case, convective and radiative boundary conditions were applied to all sides of the can, with the exception of the heated surface, which has direct view of the heating rods and thermal radiation is the dominant mechanism for coupling of the heated surface to the energy source. The silicon rod heater radiation source is idealized as a uniform far field radiation source of time-varying temperature. A PID controller modeling scheme was developed to regulate this radiating temperature to simulate the specified temperature history on the lid of the can [47].

4.1.2. The Ideal Gas Law

Both the No Flow and Porous Media model assumes the ideal gas law. The No Flow model uses it to calculate pressure, and the porous flow model requires it to relate density to the state variables. However, it is well known that the ideal gas law tends to no longer be applicable at high pressures.

One method to check if the ideal gas law is valid is through the concept of a compressibility factor (Z).

$$Z = \frac{PV}{nR_uT} = \frac{v_{actual}}{v_{ideal}} \qquad 32$$

Where P is the pressure, V is the volume, n is the number of moles, R_u is the universal gas constant, T is the temperature, v_{actual} is the actual specific volume, and v_{ideal} is the specific volume were it to follow the ideal gas law. This indicates that Z=1 allows the use of the ideal gas law.

By transforming the pressure and temperature into the reduced pressure and temperature, a generalized compressibility chart can be used to help guide this discussion.

Erickson [7] and Nemer [8] list the following molecules as the most prominent in decomposition:

Table 9: Thermochemical information for major decomposition products

Molecule	Formula	Molar Mass	Critical temperature (K)	Critical pressure (MPa)
Phenyl isocyanate [e]	C_7H_5NO	119	650	4
Aniline [b]	$C_6H_5NH_2$	93	698	4.89
4-methylaniline [c]	C_7H_9N	107	667	2.4
Propylene glycol [d]	$C_3H_8O_2$	76	624	6.1
Water vapor [a]	H_2O	18	647	22.06
Ammonia [a]	NH_3	17	405	11.28
Carbon dioxide [a]	CO_2	44	304	7.39

[a] Cengel, [b] https://en.wikipedia.org/wiki/Aniline_(data_page)#Thermodynamic_properties, [c] http://pubchem.ncbi.nlm.nih.gov/compound/p-Toluidine#section=Fire-Potential , [d] http://stenutz.eu/chem/solv6.php?name=propylene%20glycol, [e] http://pubs.acs.org/doi/pdf/10.1021/je060269j

Using this information, the compressibility of each component was determined for 550 K and 12 MPa.

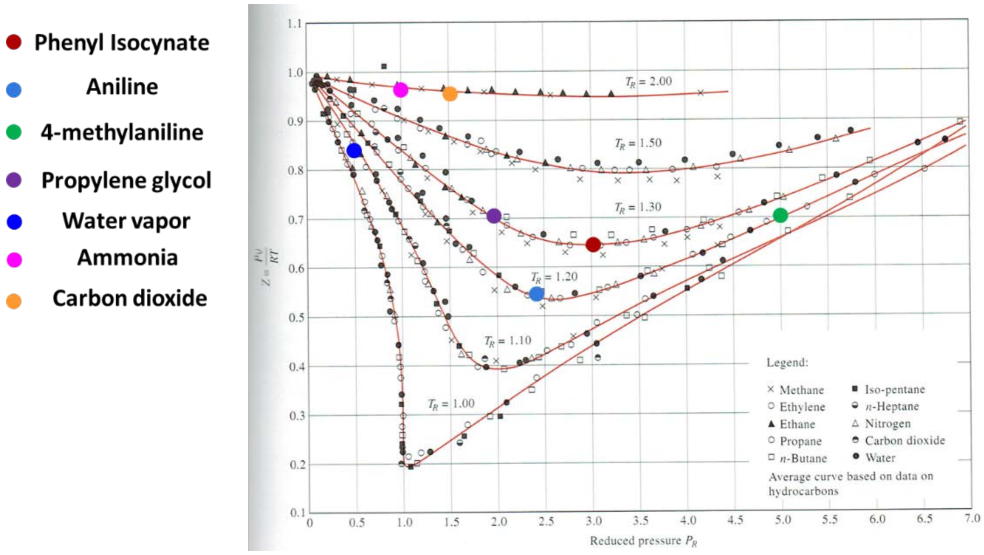

Figure 35: Generalized compressibility chart [58] with decomposition products indicated for 550 K and 12 MPa.

One reassuring result of this analysis is that the ideal gas assumption for carbon dioxide is good in our range of temperatures and pressures. However, all the organics deviate from the ideal gas assumption. Particularly worrying is aniline, since it is listed by Nemer as the largest constituent of the liquid phase (40% by area).

This analysis does not take into account that due to partial pressure, each of the constituents will not ‘feel’ the full pressure. Decreasing the pressure will, for most of these products, improve their Z number.

The global reaction for PMDI RPU, as determined by Ericson [3], [4], [7], is:

$$PMDI\ RPU \rightarrow 0.25\ CO_2 + 0.20\ LMWO + 0.35\ HMWO + 0.2\ char \qquad 33$$

It is important to again note that the coefficients in this equation are for the mass fractions. In order to calculate the partial pressure, the mole fraction of the gas species needs to be determined. Assuming one gram of PMDI RPU, the mass of each product can be calculated. The char is then discarded, as it is not available to the gas phase. A new total mass of only gas phase products can then be found. This can then be used to determine the mole fraction. In an ideal gas, the ratio of the partial pressure to the total pressure is equal to the mole fraction. (Which is problematic since an attempt if being made to prove the ideality of the gas.)

$$\frac{P_i}{P} = \frac{N_i}{\sum N_i} = \frac{{m_i}/{M_i}}{\sum {m_i}/{M_i}} \qquad 34$$

Table 10: Mass and Mole fraction information using Ericson’s global decomposition formula

Total Reaction		Gas Phase Only			
Mass Frac [g/g]	Mass [g] (for 1 g)	Mass [g] (for 1 g)	Mass Frac [g/g]	Molar Mass	Mole Frac [mol/mol]

					[g/mol]	
CO2	0.25	0.25	0.25	0.3125	44	0.51
LMWO	0.2	0.2	0.2	0.25	80	0.23
HMWO	0.35	0.35	0.35	0.4375	120	0.26
Char	0.2	0.2	0	--	--	--

Table 10 shows that about half of the gas is carbon dioxide, a quarter is low molecular weight organics (LMWO), and a quarter is high molecular weight organics (HMWO). Using Ericksons molecular weight recommendation for ‘low’ and ‘high’, each decomposition was assigned a mole fraction, assuming that it was the only component in that category (Table 11).

Table 11: Critical Pressure and Temperature information using partial pressures

Molecule	Molar Mass	T_c (K)	T_r	P_c (MPa)	x_i	P_i (MPa)	P_r
Phenyl isocyanate[e]	119	650	1.27	4	0.26	3.1	0.78
Aniline[b]	93	698	1.18	4.89	0.23	2.8	0.56
4-methylaniline[c]	107	667	1.23	2.4	0.26	3.1	1.30
Propylene glycol[d]	76	624	1.32	6.1	0.23	2.8	0.45
Water vapor[a]	18	647	1.27	22.06	0.25	3.0	0.14
Ammonia[a]	17	405	2.03	11.28	0.25	3.0	0.27
Carbon dioxide[a]	44	304	2.71	7.39	0.51	6.1	0.83

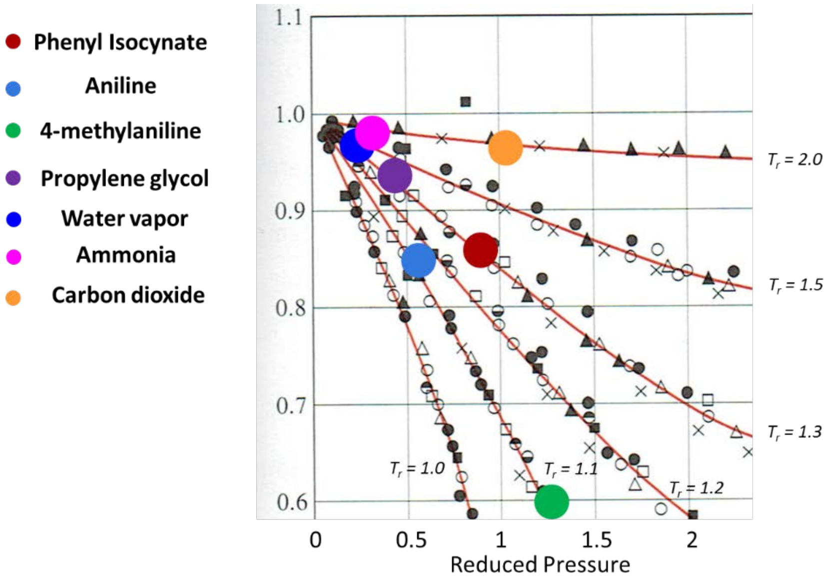

Figure 36: Generalized compressibility chart [58] with decomposition products indicated for 550 K and the partial pressure indicated in Table 11

Using the partial pressures and over estimating the contribution of each organic, most of the organics have a Z factor greater than 0.85. However, this still fails to take into account the interaction of the gases with each other. Experimental data on the real gases that trace the temperature and pressure would be best. For the moment, the use of the ideal gas law is not completely objectionable; however, it should be revisited when the decomposition products are better understood.

4.2. Mesh Resolution Study

Since the equation sets that are being solved in this Porous Media model are unlike those in the No Flow model, it was necessary to perform a new mesh resolution study. While the methodology used is the same as that presented in Section 3, the physics, and thus the results, are different.

Ten meshes of the geometry were created, ranging from 45 thousand to 11 million elements (Table 12). Each mesh was run on approximately 500 elements per processor (except in the case of the finest mesh due to a limit on the number of available processors). The run time for the inverted case scaled well with element count, however, the upright did not. In the upright runs, there were a larger number of failed time steps, resulting in a higher number of iterations before convergence.

Table 12: Mesh resolution study

Mesh Name	Number of Elements	Number of Processors	Inverted Runtime (hr:min:sec)	Upright Runtime (hr:min:sec)
1x	45,056	80	0:51:55	0:54:51
5x	228,393	448	1:30:24	1:46:42
8x	360,448	736	2:13:00	2:15:42
11x	479,987	944	1:42:59	2:29:08
15x	677,971	1344	1:56:08	2:59:03
24x	1,102,778	2192	2:07:23	4:13:51
48x	2,158,146	4304	2:54:24	7:37:31
64x	2,883,584	5632	3:06:42	8:10:06
82x	3,689,835	7376	3:30:25	12:05:07
240x	10,825,690	7680	7:04:32	22:56:00

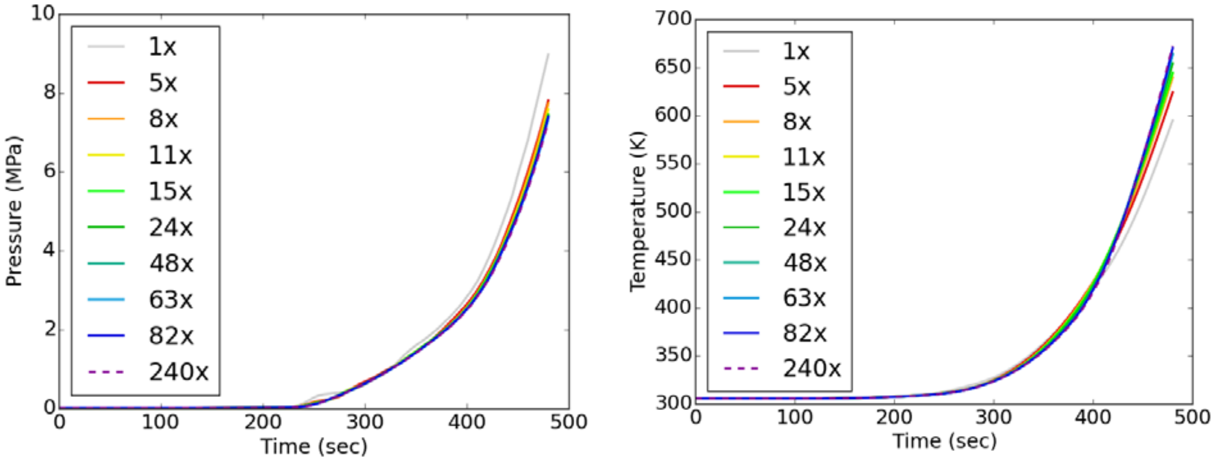

(a) (b)

Figure 37: Inverted (a) pressure vs time and (b) temperature vs time of the embedded mass for the meshes investigated in this study.

Figure 37 through Figure 40 show the temperature and pressure histories over time for each of the meshes, along with the difference between each coarser mesh and the finest (240x) mesh for the responses of interest. From Figure 39 and Figure 40, it is clear that the difference between the coarser and finest mesh becomes less as the element count of the coarser mesh increases. This visual aid is particularly helpful in the case of the average pressure, as there is no formal convergence theory for this quantity.

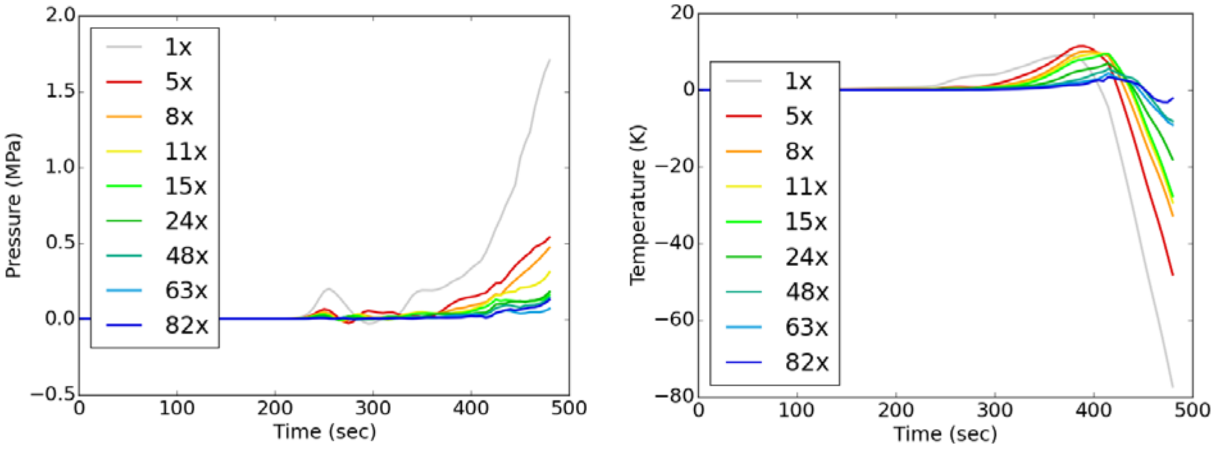

(c) (d)

Figure 38: Inverted (a) pressure vs time and (b) temperature vs time for the difference between the finest (240x) and the mesh of interest.

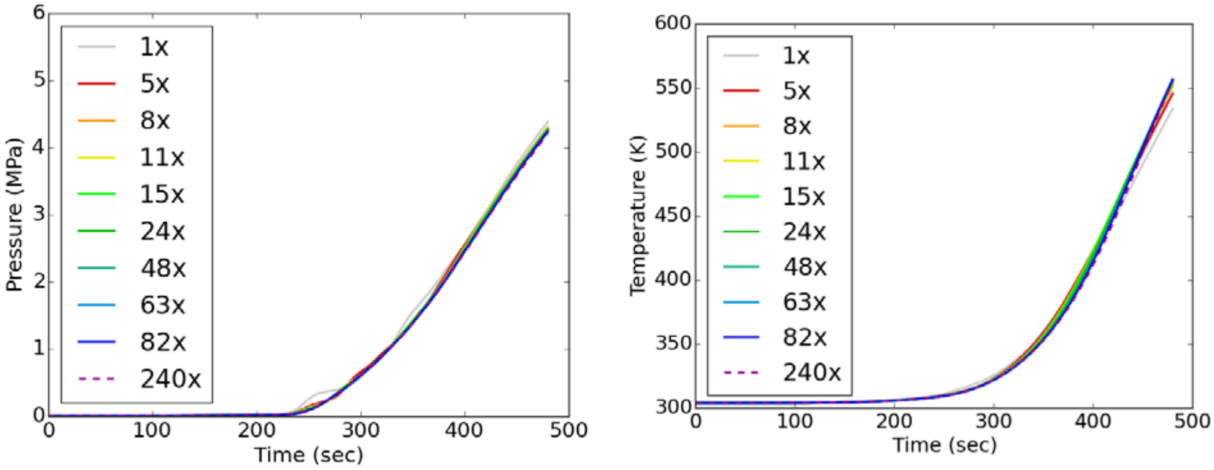

(a) (b)

Figure 39: Upright (a) pressure vs time and (b) temperature vs time of the embedded mass for the meshes investigated in this study.

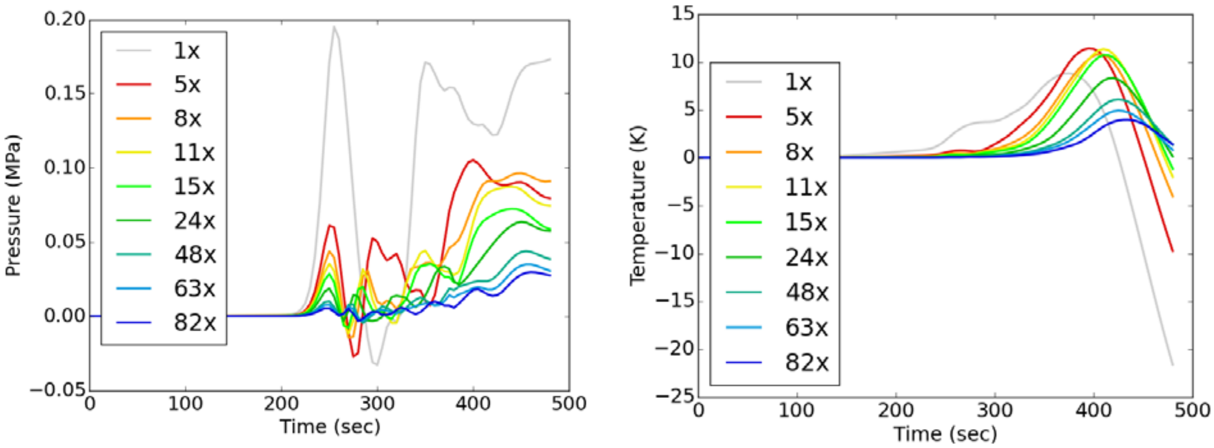

(c) (d)

Figure 40: Upright (a) pressure vs time and (b) temperature vs time for the difference between the finest (240x) and the mesh of interest.

For the solid and gas phase temperature, the time averaged L_2 and L_∞ norms are presented in Figure 41 and Figure 42 for the inverted and upright configurations. The expected convergence rate is -1, due to the solution stabilization scheme used in this problem. Of note is the L_∞ norms for the gas phase. Unlike with the solid phase temperature, there is a difference in the convergent rates between upright and inverted in the gas phase. This is consistent with the buoyance driven flow being different in the upright and inverted orientations. It is also important to note that a gas phase temperature only exists for the foam.

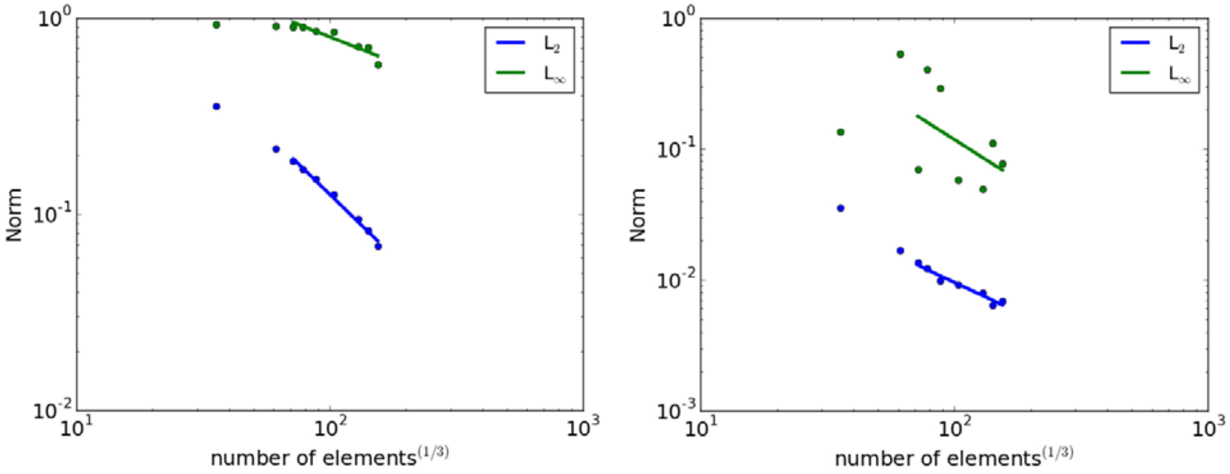

(a) (b)

Figure 41: Inverted Configuration. Time averaged L_2 and L_∞ convergence rates for (a) the solid temperature vs elements and (b) the gas temperature vs elements. The convergence rates for the temperature in the solid phase are $L_2 = -1.25$ and $L_\infty = -0.51$. In the gas phase, the rates are $L_2 = -0.91$ and $L_\infty = -1.23$

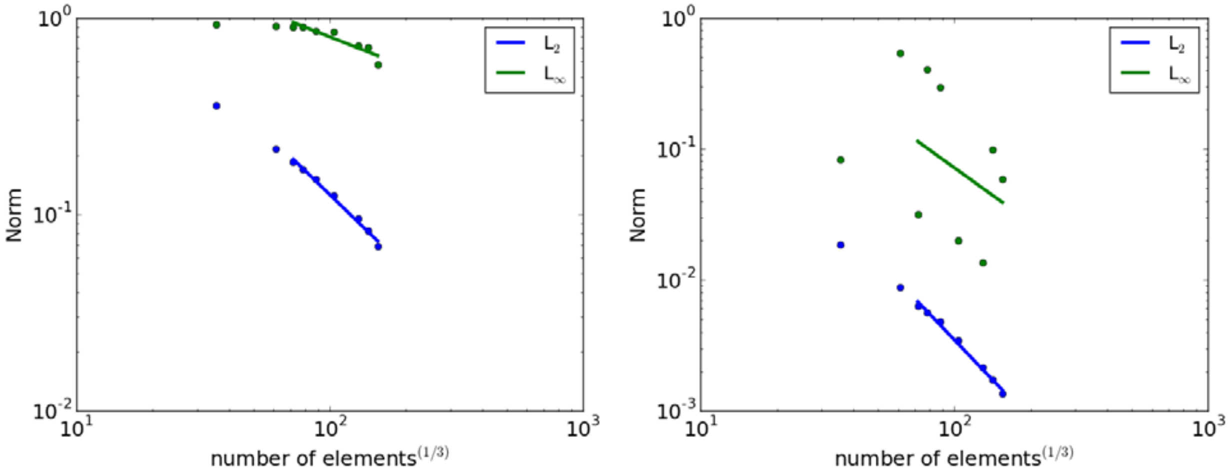

(a) (b)

Figure 42: Upright Configuration. Time averaged L_2 and L_∞ convergence rates for (a) the solid temperature vs elements and (b) the gas temperature vs elements. The convergence rates for the temperature in the solid phase are $L_2 = -1.25$ and $L_\infty = -0.51$. In the gas phase, the rates are $L_2 = -2.03$ and $L_\infty = -1.40$

Also of interest in Figure 41 and Figure 42 is the two distinct convergence lines that form in the gas phase L_∞ norms. This is explained by Figure 43. The buoyant gas plumes that appear along the heated plate vary in size and shape in these four meshes, however, they do not appear to change in a mesh convergent way. So, while the average error (L_2) for the gas temperature is convergent, the maximum error (L_∞) is effected more by the element as the interface between the hot plate and the foam, rather than the overall mesh size.

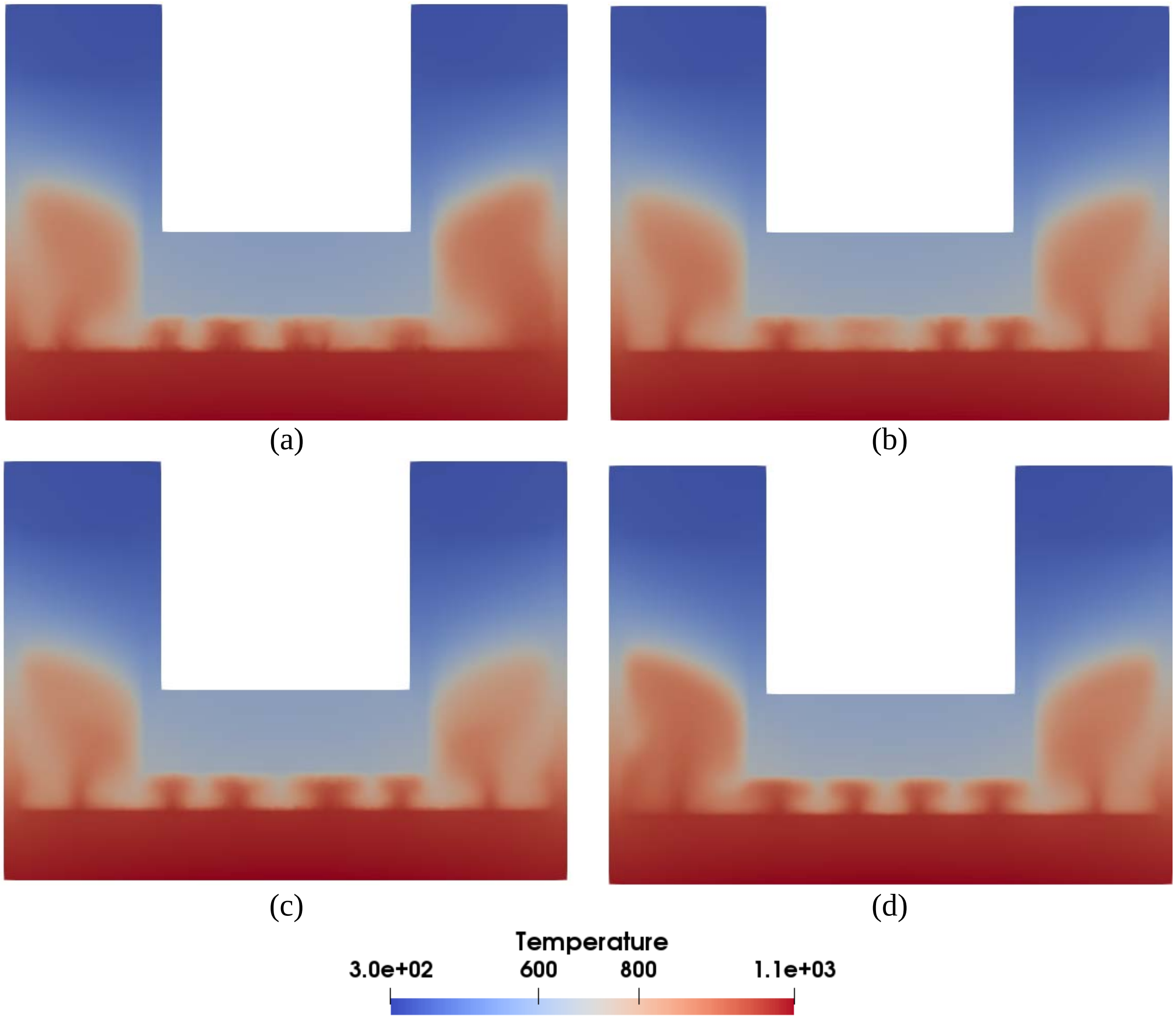
(a) (b)

(c) (d)

Figure 43: Cross sectional views of the temperature of the gas (foam region) and of solid temperature (can region) of the inverted mesh resolution study at (a) 10x, (b) 48x, (c) 63x, and (d) 240x

Since the average quantities for the mesh were convergent, it was deemed that the 15x mesh would be used to conduct future studies. Table 13 presents the maximum mesh error for the quantities of interest.

Table 13: Max error in quantity of interest for 15x mesh

	Upright	*Inverted*
Pressure	4.9%	5.0%
Temperature at TC25	2.5%	2.1%

4.3. Parameter Calibration

In previous unpublished work at Sandia, a parameter study of the Porous Media model was conducted using the TDI polyurethane foam material properties and decomposition mechanism.

The results of that study showed that four parameters had a large effect on the results: the permeability (K) of the virgin and char foam (Eq 20 and 22), the organic liquid fraction ($organic$ in Eq 36 through 38) and the Rosseland-mean extinction coefficient for the char (β_R in Eq. 31).

PMDI is a closed cell foam under normal conditions; as such, it has zero permeability. However, it is possible that the cell walls rupture at elevated temperatures and pressures before chemical decomposition sets in. There is no validated model for this type of onset of permeability, therefore, in the interest of promoting numerical stability, the virgin foam was assigned a non-zero permeability. However, the char is permeable, but it is impossible to know what the value of this quantity is in situ.

The organic liquid fraction is the fraction of the organic decomposition products that will go into solid vs gas phase. While many of the decomposition products are known to be in both the vapor and liquid phase for the pressures and temperatures seen in the experiments, the exact vapor/liquid split is unknown (and will be discussed in the next chapter). Eq 35 through 38 show the decomposition mechanism for PMDI polyurethane and how $organic$ affects the mechanism. When $orgnaic$ is 0, LMWO and HMWO are in the gas phase; when it is 0.44, they are in the condensed phase.

$$PMDI\ RPU\ = 0.45\ FOAMA + 0.15\ FOAMB + 0.4\ FOAMC \tag{35}$$

$$FOAMA\ \rightarrow [0.56\ ]CO_2 + [\ 0.44 - organic]LMWO + [organic]char \tag{36}$$

$$FOAMB\ \rightarrow\ [1 - 2 * organic]HMWO + [2 * organic]char \tag{37}$$

$$FOAMC\ \rightarrow [0.5 - organic]HMWO + [0.5 + organic]char \tag{38}$$

The Rosseland-mean extinction coefficient (β_R) is used to calculate the contribution of radiation in the pore space to the conductivity ($k_{e,i}$). Once calculated, $k_{e,i}$, is used in Eq 29. β_R can be measured and is equal to the absorption plus the scattering. However, like the char porosity, these quantities cannot be measured in situ.

To calibrate the parameters, the results of the simulation were compared to represented results from the 150 C/min data set (Figure 44). The temperature at TC 25 and the pressure in the can were the responses of interest.

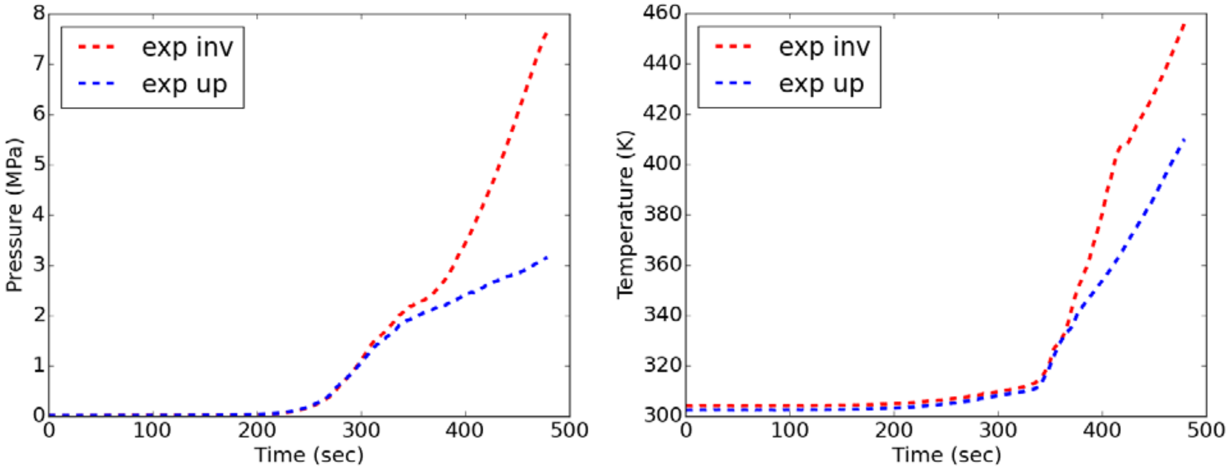

(a) (b)

Figure 44: Inverted and upright experimental results for the 150 C/min experiments (a) temperature vs time for TC 25 and (b) pressure vs time.

The optimization was performed in Dakota [59] using a global (rather than gradient) based method to find the set of parameters that would reproduce the experiments. Due to a limitation of Dakota, the results and the experiments needed to be normalized so that pressure would not be favored over temperature (since pressure is on the order of 10^6 and temperature on the order of 10^3). Both the inverted and upright temperatures and pressures were normalized by the maximum value of the inverted experiment.

4.3.1. Original Calibration

The original calibration optimized the virgin foam permeability, the char foam permeability, the organic gas fraction, and char β_R. The ranges for these parameters and the optimized values are shown in Table 14. The values explored in the study are shown in Figure 45 with the optimized value, run #114, highlighted. There was a problem in this optimization: the char β_R upper value was higher than physically possible. The char foam should not have lower radiative contribution than the virgin foam, thus the upper bound of char β_R should be 1990 mK. This was corrected in later studies. While this is an issue, the results of this study were still instructive and used to guide later work.

Table 14: Parameters optimized in calibration

	Low Bound	High Bound	Optimized Value
Virgin Foam Permeability [m^2]	10^{-14}	10^{-9}	$10^{-9.01}$
Char Foam Permeability [m^2]	10^{-9}	10^{-6}	$10^{-7.5}$
Organic Liquid Fraction	0.25	0.44	0.347
Char β_R [mK]	200	40,000	21487

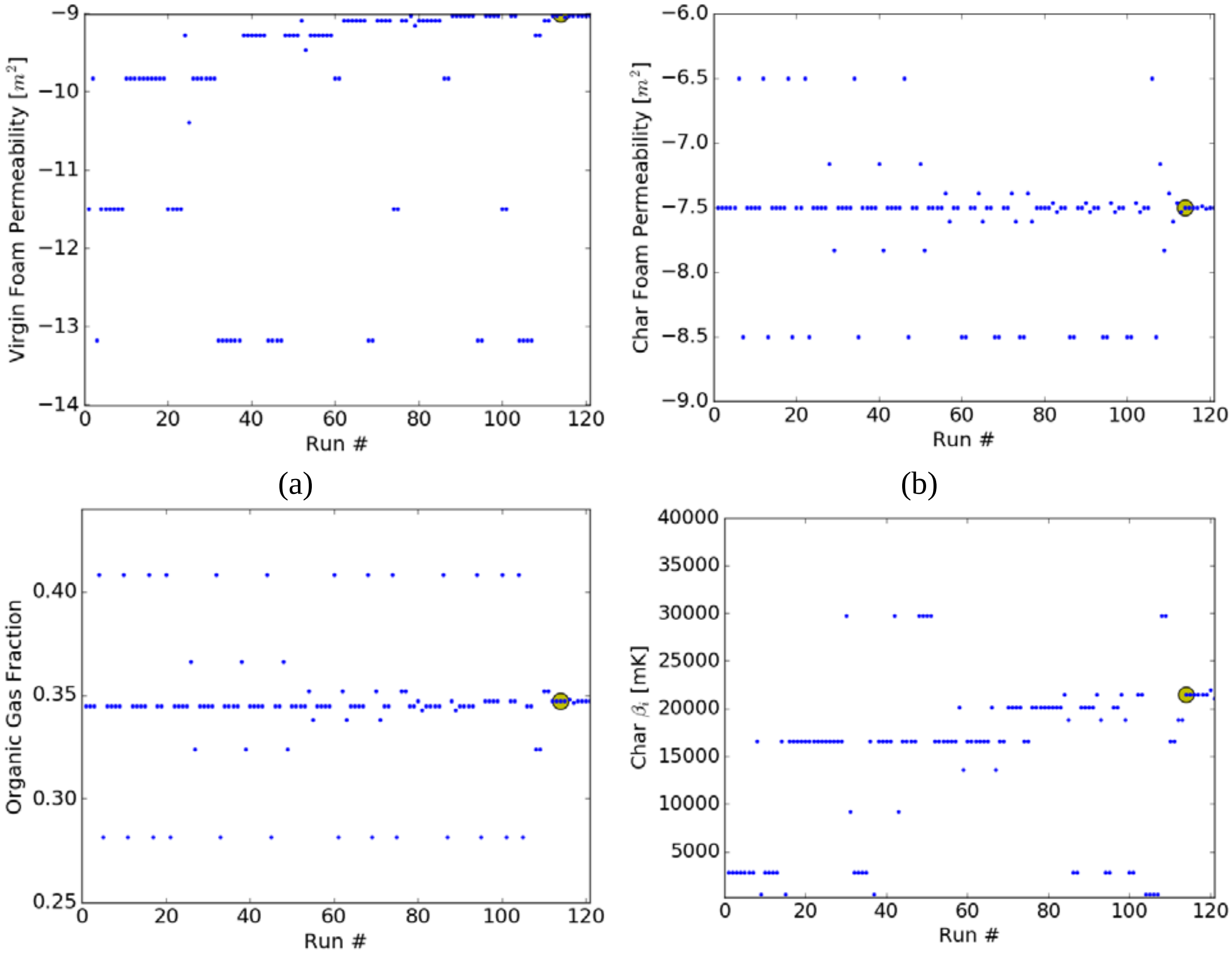

(a) (b)

(c) (d)

Figure 45: Values explored for each run with optimized value highlighted for (a) virgin foam permeability, (b) char foam permeability, (c) organic gas fraction, and (d) char β_R

Figure 46 shows the simulated results compared with the experiment. For pressure, the results are quite promising: the simulation returned different pressures for upright vs inverted, which had been lacking in the No Flow model. However, the shape of the curve is not well matched. The experiments have an inflection change at approximately 350 seconds that the simulation fails to capture. For temperature, the prediction is poor. First, both upright and inverted are over predicting and do not match the shape of the cuve. Also, upright is predicting a higher temperature than inverted, which is opposite of the experiments.

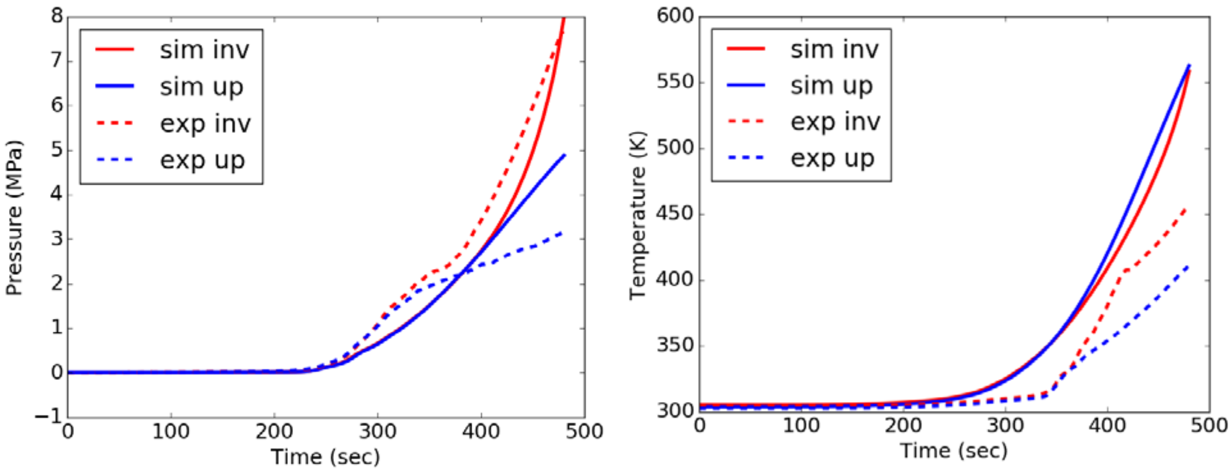

(a) (b)

Figure 46: Inverted and upright experimental results for the 150 C/min experiments (a) temperature vs time for TC 25 and (b) pressure vs time.

These results led to the following idea: calibrating for pressure and temperature separately might yield insight into the poor results.

4.3.2. Temperature and Pressure Calibrations

While attempting to optimize these parameters for PMDI polyurethane foam for the Porous Media model, it was found that the optimization struggled to produce a set of parameters that would fit the temperature at a location interest (TC 25) and pressure in the can simultaneously. In an effort to understand this, additional optimizations were performed, specifically optimizing the problem for either temperature or pressure, rather than both simultaneously (Figure 47 and Figure 48).

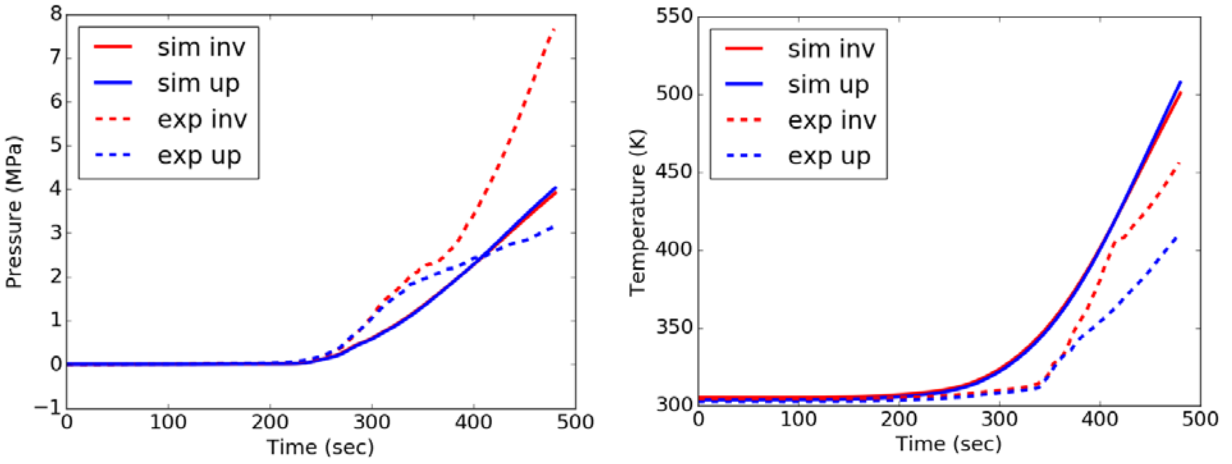

a b

Figure 47: Pressure (a) and Temperature (b) compared to experiment when optimizing for only temperature

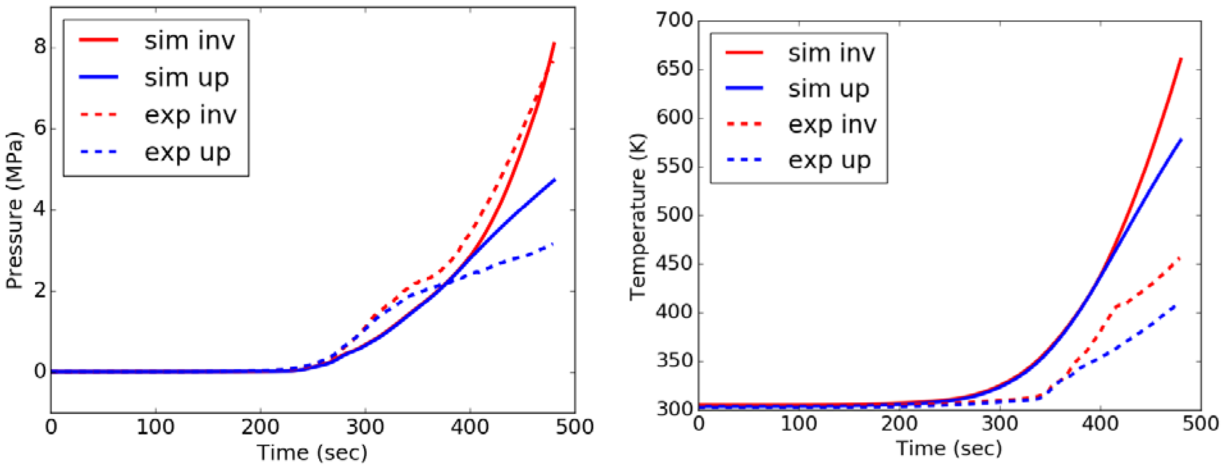

a b

Figure 48: Pressure (a) and Temperature (b) compared to experiment when optimizing for only pressure

Table 15: Parameters optimized in calibration

	Low Bound	**High Bound**	**Optimized Value**	
			Temperature	**Pressure**
Virgin Foam Permeability [m^2]	10^{-12}	10^{-8}	$10^{-11.97}$	$10^{-7.17}$
Char Foam Permeability [m^2]	10^{-8}	$10^{-6.5}$	$10^{-7.99}$	$10^{-10.25}$
Organic Liquid Fraction	0.25	0.44	0.439	0.439
Char β_R [mK]	200	1990	1961	439

When reviewing the parameters chosen by the optimizer in the temperature only versus pressure only studies, it became clear that for the temperature only case, all the parameters where chosen to limit heat transfer to TC 25. Since the No Flow model had shown good agreement with the validation experiments for TC 25, it was concluded that the flow must be affecting the heat transfer.

4.3.3. Thermal Conductivity

To simplify the problem, a cube of non-reacting polyurethane foam was considered. In the No Flow case, the energy equation is:

$$\rho c \frac{\partial T}{\partial t} = \nabla(k_b + k_e)\nabla T \qquad 39$$

where ρ is the bulk mass density of the foam; c is the specific heat; T is temperature; t is time; k_b is the thermal conductivity; k_e is an effective conductivity for radiant heat transfer in optically thick media.

In the Porous Media case, the equation is more complicated. The gas phase enthalpy is:

$$\frac{\partial(\bar{\psi}\rho_g h_g)}{\partial t}+\frac{\partial(\rho_g u_{j,g} h_g)}{\partial x_j}=-\frac{\partial q_{k,j}^{h,g}}{\partial x_j}+\frac{\partial(\bar{\psi}p_g)}{\partial t}+h_{cv}(\bar{T}-T_g) \qquad 40$$

Where h_g is the mixture averaged gas phase enthalpy, h_{cv} is the volumetric heat transfer coefficient, $\bar{T}$ is the porous condensed phase temperature, $h_{k.g}$ is the gas phase enthalpy of the k^{th} species. $q_j^{h,g}$ is the gas phase energy diffusive flux and is modeled as:

$$q_j^{h,g}=-\bar{\psi}\rho_g D_g\frac{\partial h_g}{\partial x_j} \qquad 41$$

where D_g is the mixture averaged gas phase mass diffusivity.

The condensed phase enthalpy is defined as:

$$\frac{\partial(\bar{\rho}\rho_g\bar{T})}{\partial t}=-\frac{\partial q_j^h}{\partial x_j}+h_{cv}(T_g-\bar{T}) \qquad 42$$

Where q_j^h is the condensed phase energy diffusive flux:

$$q_j^{h,g}=-(k_b+k_e)\frac{\partial\bar{T}}{\partial x_j} \qquad 43$$

where k is the thermal conductivity and k_e is the effective conductivity for radiant heat transfer in optically thick media.

The bulk conductivity, k, that was being used for the Porous Media model was the same as that used in the No Flow model, k_b, which was experimentally measured.

Table 16: Measured thermal conductivity with respect to temperature

Temperature [K]	Thermal Conductivity [W/mK]
303.15	4.86E-02
523.15	7.06E-02

However, since the Porous Media models an open cell, rather than closed cell foam, using this value for the solid phase could ‘double count’ the gas contribution to the heat transfer. To test this theory, a cube of non-reacting foam was simulated (Figure 49), where sides 1 through 5 had an adiabatic boundary condition and side 6 was at a constant temperature of 400K.

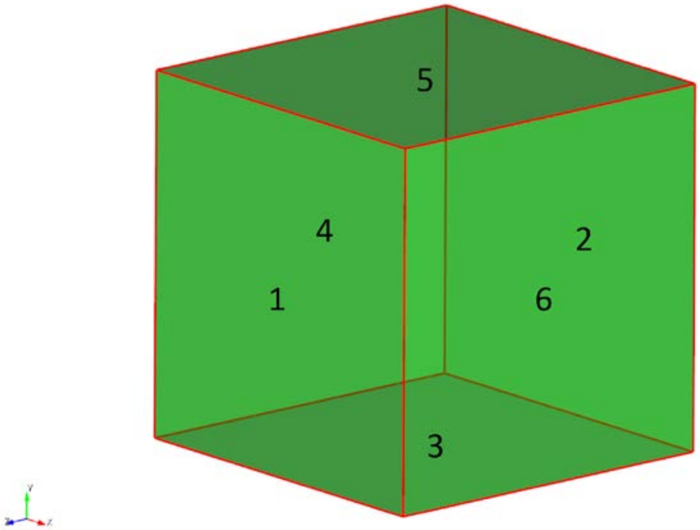

Figure 49: Cube of foam used to tests bulk conductivity theory. The cube is 1 cm cubed and sides 1 through 5 had an adiabatic boundary condition and side 6 was at a constant temperature of 400K.

The simulation was run for both the No Flow and Porous Media models. In the Porous Media case, it was run with gravity point in the direction of both side 4 and 6; there was no difference caused by orientation. For both the No Flow and the Porous Media, sides 1, 2, 3, and 5 were the same temperature (as would be expected due to the symmetry of the problem). In addition, a version of the Porous Media model was run where the gas and solid phase temperatures were not coupled (i.e., no heat transfer between the gas and solid phase). The results (Figure 50) show that decoupling the gas from the solid brings the Porous Media results into line with the No Flow results.

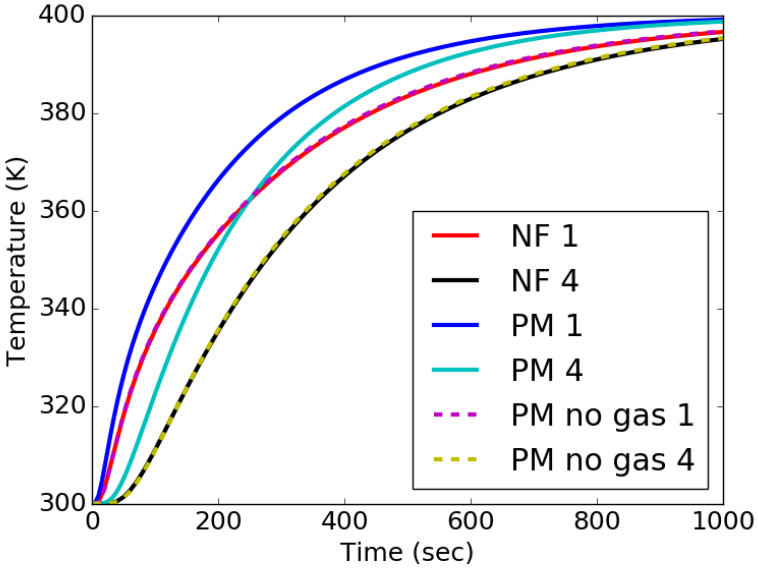

Figure 50: Temperature in the middle of side 1 and side 4 for the No Flow (NF), Porous Media (PM), and the decoupled Porous Media (PM no gas)

Since decoupling the problem is not a permanent solution, it was decided to lower the bulk conductivity by the amount that the gas phase was contributing. Assuming constant specific heat, equation 41 can be rewritten as:

$$q_j^{h,g} = -\bar{\psi}\rho_g D_g c \frac{\partial T_g}{\partial x_j} = -k_g \frac{\partial T_g}{\partial x_j} \quad 44$$

Where k_g is the gas conductivity. Table 17 lists the values used to calculate the gas conductivity. Once calculated, a new bulk conductivity can be calculated, which does not account for the gas that was present when the foam's bulk conductivity was measured (Table 18).

Table 17: Calculating the gas conductivity, k_g

Mass Diffusivity [m^2/s]	2E-5
Density [kg/m^3]	1.76
Porosity	0.787
Specific Heat [J/kg K]	1000
Gas Conductivity [W/mK]	2.78E-02

Table 18: Measured thermal conductivity with respect to temperature. NF bulk conductivity refers to the experimentally measured thermal conductivity that was used in the No Flow model, PM bulk conductivity refers to the bulk conductivity with the gas contribution removed, and PM solid conductivity refers to the conductivity of the solid phase alone (no pore space).

Temperature [K]	NF Bulk Conductivity (k_b) [W/mK]	PM Bulk Conductivity (k_b) [W/mK]	PM Solid Conductivity ($k_{s,i}$) [W/mK]
303.15	4.86E-02	2.08E-02	9.77E-02
523.15	7.06E-02	4.28E-02	2.01E-01

An additional change was made to the conductivity. In the original model, conductivity was only a function of temperature, rather than a function of temperature and reaction. In addition, this conductivity was the bulk conductivity (i.e., the conductivity of the solid and the pour space). When the gas contribution to the conductivity was removed, as discussed above, its quantity was still the bulk conductivity. In order to change the conductivity to be a function of reaction, the solid conductivity of the foam was the input given to the code, and Aria solved for the bulk conductivity through the following equation:

$$k_b = \sum_i \frac{V_{s,i}}{V_{total}} k_{s,i} \quad 45$$

where $V_{s,i}$ is the solid volume of the i^{th} species, V_{total} is the total volume, and k_b is the bulk conductivity, and $k_{s,i}$ is the solid phase conductivity of the i^{th} species.

As seen in Figure 51, making this change to the conductivity bring the temperatures in line with the No Flow model.

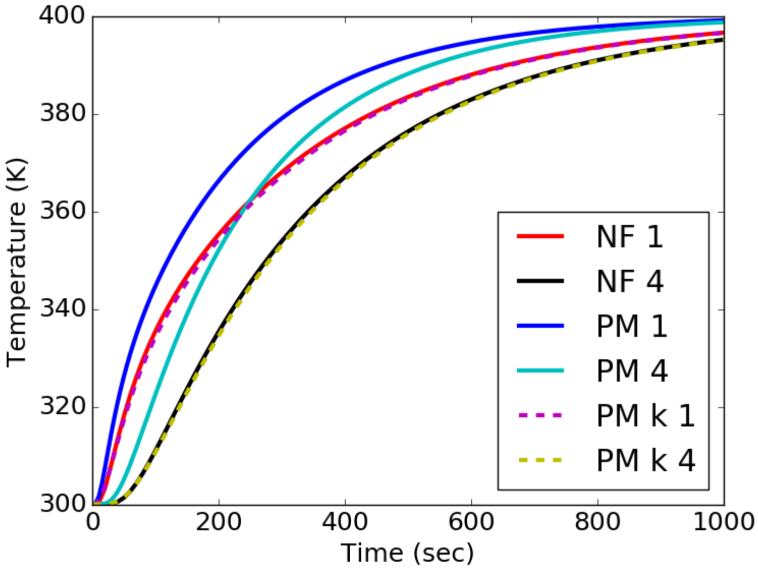

Figure 51: Temperature in the middle of side 1 and side 4 for the No Flow (NF), Porous Media with the original conductivity (PM), and Porous Media with volume averaged conductivity (PM k)

4.3.3.1. Application to Foam in a Can and Mass Diffusivity

Using these new conductivity values in the Foam in a Can geometry only lowered the temperature at TC 25 by approximately 20K (Figure 52). By calculating the density of the gas and the porosity of the foam using the PMDI reaction mechanism, the gas conductivity over the reaction range can be determined. This calculation assumes that density and specific heat are constant. Table 19 shows the result. Compared to NIST's measured values of thermal conductivity for carbon dioxide [60], the calculated values are two orders magnitude off.

Diffusivity does vary with pressure and temperature. Using Chapman-Enskog theory [61], a pressure and temperature dependent diffusivity can be defined as shown in equation 46:

$$D_g(T,p) = C_M \frac{T^{3/2}}{p_g} = \frac{D_0\, p_0}{T_0^{3/2}} \frac{T^{3/2}}{p_g} \qquad 46$$

where C_M is a constant derived from molecular properties, D_0 is the diffusivity at standard conditions, p_0 is the standard pressure, and T_0 is the standard temperature. Using this diffusivity rather than a constant value leads to a result that is of the same order of magnitude as the NIST values (Table 19).

Table 19: Values of gas conductivity, experimentally measured by NIST, calculated using constant mass diffusivity, and calculated using the Chapman-Enskog theory.

	NIST values k [W/mK]	Constant Diffusivity k [W/mK]	Varying Diffusivity k [W/mK]
0.5	3.36E-02	1.13E-01	4.93E-02
1	3.38E-02	2.42E-01	5.48E-02
2.5	3.42E-02	6.82E-01	5.91E-02
5	3.51E-02	1.43E+00	6.19E-02
7.5	3.61E-02	2.21E+00	6.42E-02
10	3.73E-02	3.03E+00	6.64E-02
12.5	3.86E-02	3.94E+00	6.88E-02
15	4.01E-02	4.90E+00	7.13E-02

The results of using a varying mass diffusivity is shown in Figure 52. This change resulted in a much lower temperature than either than the original implementation or the constant diffusivity case.

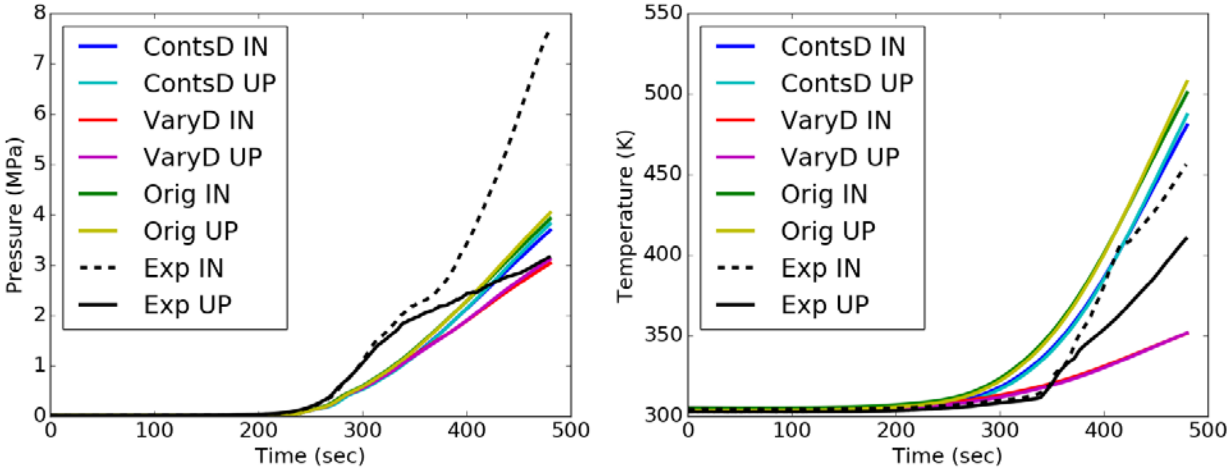

(a) (b)

Figure 52: Pressure (a) and Temperature (b) for Constant Mass Diffusivity (ConstD), Varying Mass Diffusivity (VaryD), and Original Implantation (Orig) compared with experimental results (Exp) in the inverted (IN) and upright (UP) orientations.

4.3.4. Optimization After Revisions to the Model

After making the additions and revisions to the model described in Section 4.3.3, the optimization was redone. The ranges for these parameters (as well as the others investigated in the calibration) are shown in Table 20.

Table 20: Parameters optimized in calibration performed after model changes

	Low Bound	High Bound	Optimized Value
Virgin Foam Permeability [m^2]	10^{-14}	10^{-8}	$10^{-11.6}$
Char Foam Permeability [m^2]	10^{-8}	$10^{-6.5}$	$10^{-7.18}$
Organic Liquid Fraction	0	0.44	0.38
Char β_R [mK]	200	1990	388

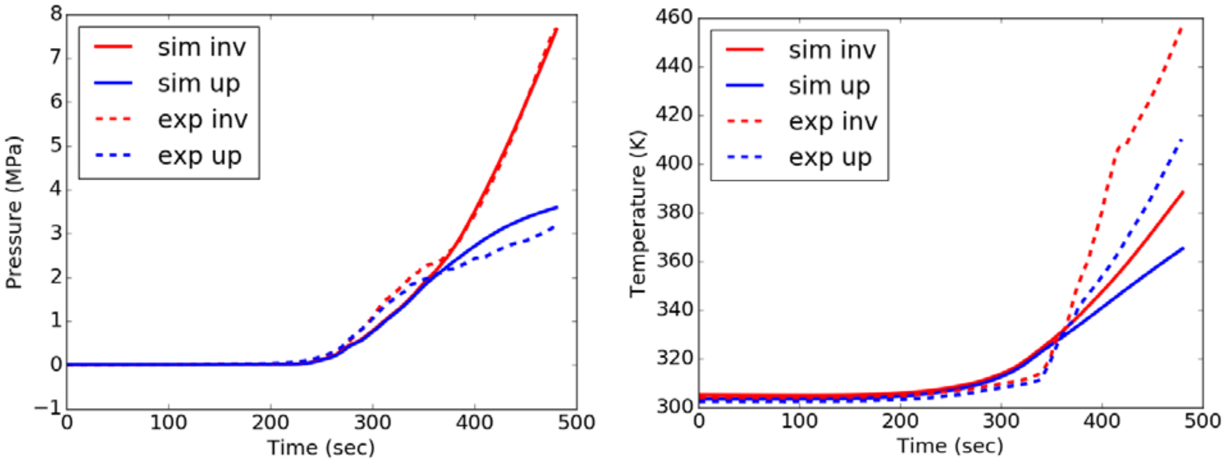

(a) (b)

Figure 53: Optimized simulation results (solid) with experimental values (dashed) for upright (blue) and inverted (red) for the 150 °C/min heating rate for (a) pressure and (b) temperature of the embedded object (TC 25).

Figure 53 shows the outcome of the optimization. The inverted pressure (Figure 53a) agrees well with experimental results, and the upright pressure is also a good match, although it under-predicts pressure early in time and over predicts late in time. The temperature of the slug, however, does not agree well. It appears that, though the responses were normalized in an attempt to have them both considered to the same degree, the pressure was still favored over the temperature in the optimization. While it is possible that there are more improvements to be made to the optimizing procedure, it was decided that at this juncture, the results were of suitable quality to move on to the validating the model. This decision was made because it requires months to run each optimization, and continuing to optimize to this single data set without an evaluation of how well the model is doing could waste immense amounts of time trying to correct details that would be better addressed through other methods, such as alternations the underlying physics.

4.4. Validation of Calibrated Model

4.4.1. 150 C/min

While the model was calibrated to the 150 C/min data, it was only calibrated to the pressure and the temperature at TC25 for the first 480 seconds. Thus, it is informative to evaluate the other thermocouples locations, as well at the remaining 500 seconds of the upright configuration.

Figure 54 shows that the upright temperature and pressure trends continue past 480 seconds – the pressure over predicts and the temperature under predicts. Figure 55 shows the thermocouples along the side of the can. The thermocouples closest to the heated plate over predict the temperature, while the thermocouples lower on the can are in good agreement. This behavior was also seen in the No Flow model, while the under prediction of TC25 was not. As was seen in Section 3.3, TC25 is much more sensitive to the foam's properties, thus making a fundamental change to the foam model (adding in the porous media equations) has had a drastic effect on TC25 and little effect on the thermocouples that line the outside of the can. However, adding the porous media equations have also allowed for differentiation between upright and inverted: the time at which they split from each other, ~325s, is well predicted.

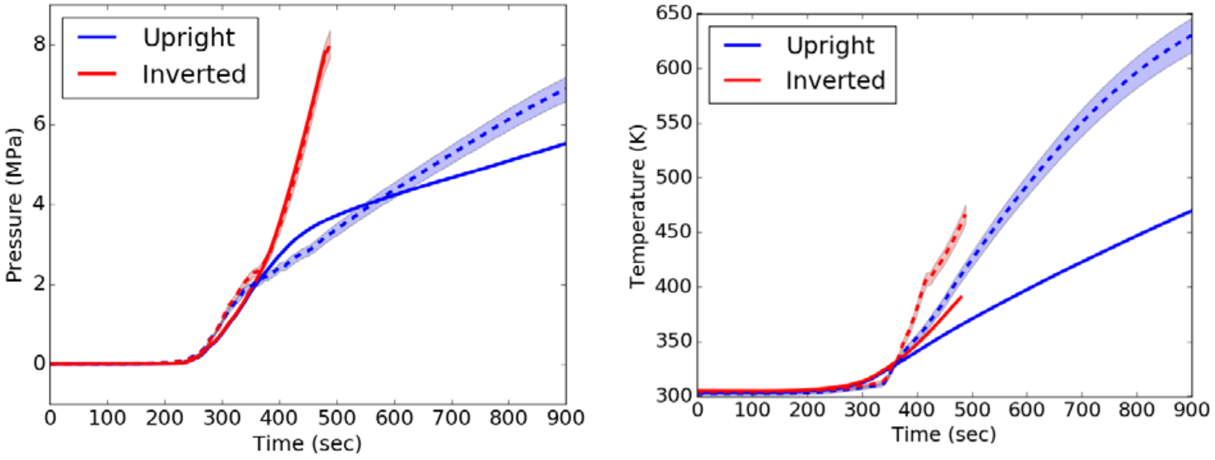

(a) (b)

Figure 54: Simulation results (solid) with experimental values (dashed) for the 150 °C/min heating rate for (a) pressure and (b) temperature of the embedded object (TC 25).

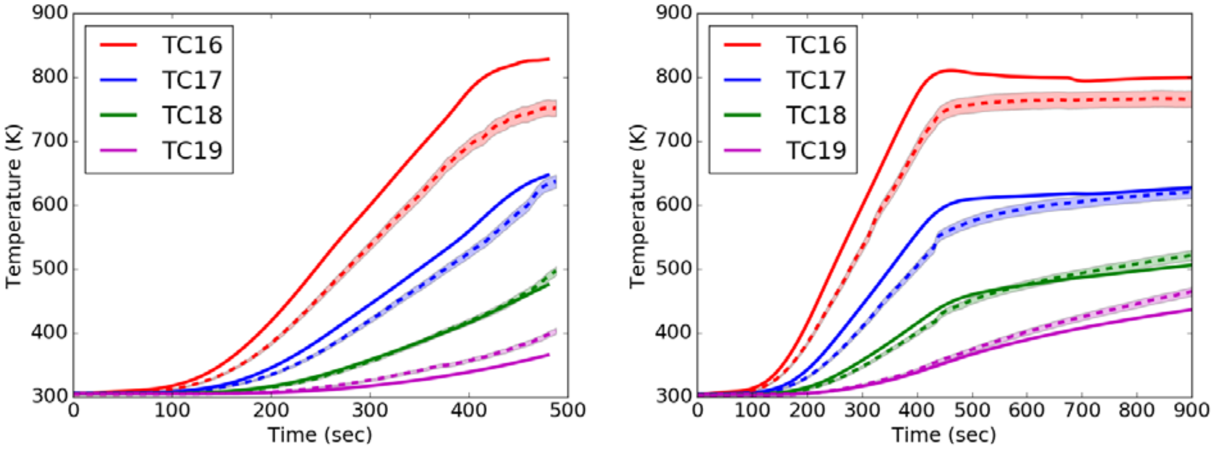

(a) (b)

Figure 55: Simulation results (solid) with experimental values (dashed) for the 150 °C/min heating rate for (a) inverted and (b) upright.

4.4.2. 50 C/min Heating Rate with Parameters from 150 C/min Optimization

The model, containing the parameters optimized for at the 150 C/min heating rate, was then validated using experimental data from the 50 C/min heating rate.

While the agreement is not as good as in the calibrated case, it does show promise (Figure 56). The upright pressure is well predicted, while the inverted pressure is too high. The temperature prediction for TC25 is of a similar quality as seen in the 150 C/min case, as are the thermocouples along the side of the can (Figure 57). The time at which the upright and inverted break away from each other is not as well predicted as it was in the 150 C/min case.

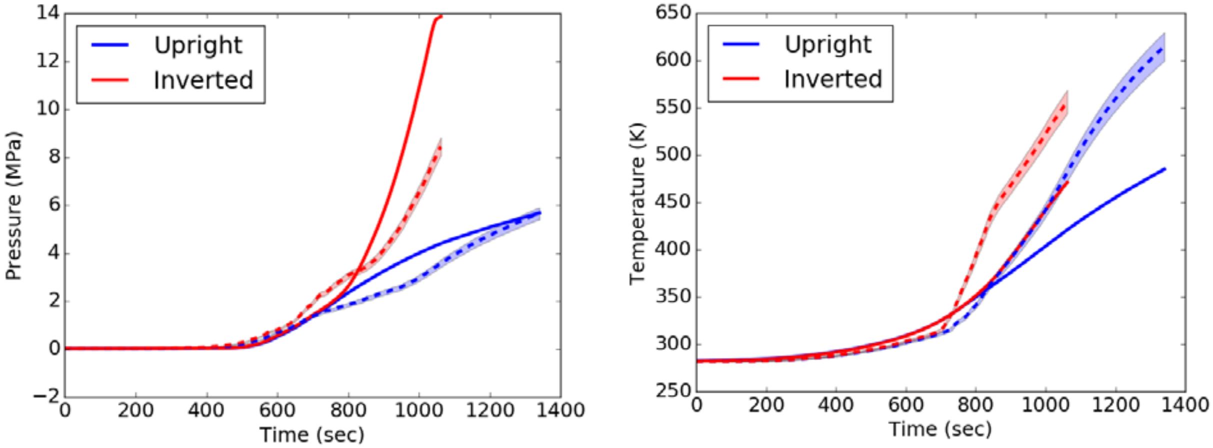

(a) (b)

Figure 56: Simulation results (solid) with experimental values (dashed) for the 50 °C/min heating rate for (a) pressure and (b) temperature of the embedded object (TC 25).

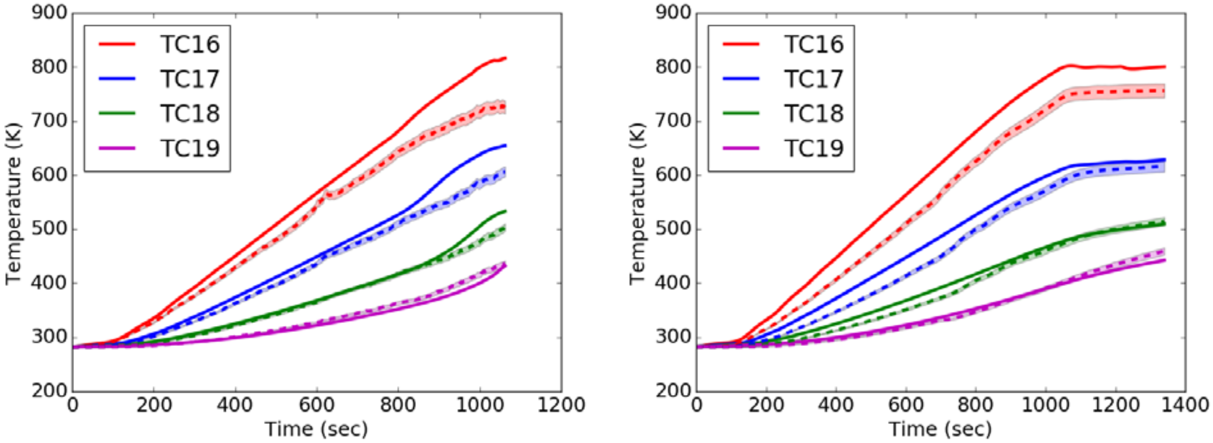

(a) (b)

Figure 57: Simulation results (solid) with experimental values (dashed) for the 50 °C/min heating rate for (a) inverted and (b) upright.

4.4.3. *The Phase of Decomposition Products*

As noted in the 50 C/min validation of the model, the upright and inverted temperature and pressures traces did not differentiate themselves from each other as early in time in the simulations as in the experiments. Upon reflection, this is likely caused by the only difference between the upright and the inverted simulations being the flow of gasses, whereas in reality, the phase of the decomposition products would be different between the two orientations. As previously discussed (Section 2.2), in the inverted orientation, liquid products may be boiling on the hot plate, increasing the rate of gasification. This would mean that in the inverted orientation, there are, on average, more decomposition products in the gas phase, were as in the upright configuration, there are more in the liquid phase.

Significant resources will be needed to include additional models into the simulations, thus a 'quick model' was created in order to understand the impact of this liquid phase. Using the same optimization framework described in this chapter, two separate organic liquid fraction values were used in the upright and inverted optimization to approximate the effects of mass motion that are not captured by the physics in this model. The ranges for these parameters, as well as the optimal results, are shown in Table 21.

Table 21: Parameters optimized in two organic liquid fractions calibration

	Low Bound	**High Bound**	**Optimized Value**
Virgin Foam Permeability [m^2]	$1\text{x}10^{-14}$	$1\text{x}10^{-8}$	$7.76\text{x}10^{-13}$
Char Foam Permeability [m^2]	$1\text{x}10^{-8}$	$3.15\text{x}10^{-7}$	$1.48\text{x}10^{-8}$
Upright Organic Liquid Fraction	0	0.44	0.37
Inverted Organic Liquid Fraction	0	0.44	0.22
Char β_R [mK]	200	1990	340

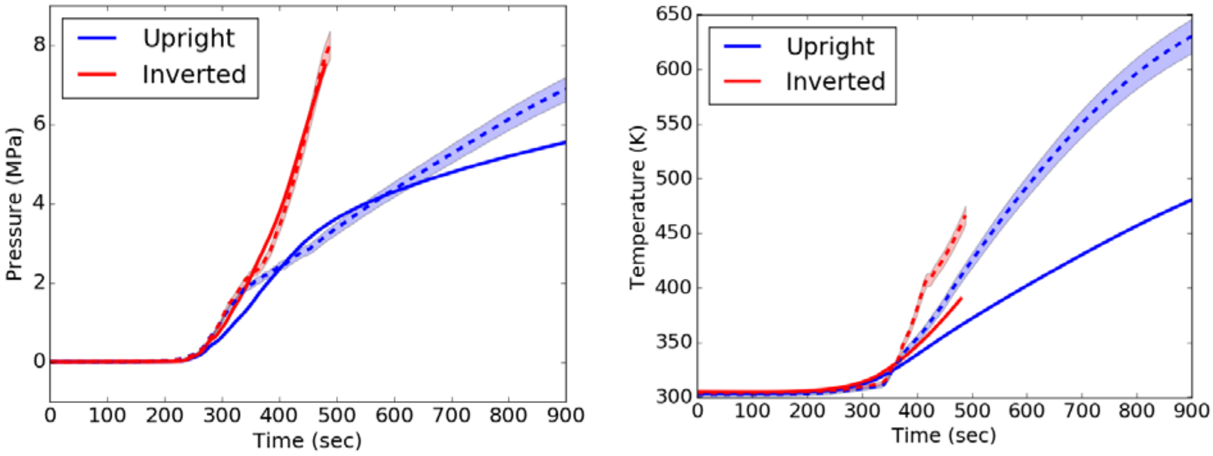

(a) (b)

Figure 58: Optimized separate organic liquid fraction simulation results (solid) with experimental values (dashed) for upright (blue) and inverted (red) for the 150 C/min heating rate for (a) pressure and (b) temperature of the embedded object (TC 25).

Figure 58 shows the results of the optimization using two organic liquid fractions. Again, the inverted pressure has the best match, again most likely being an artifact of how the optimization was performed. In this case, the upright and inverted differentiate from each other much earlier in time (~275 seconds) compared to the one organic liquid fraction (~375 seconds). There was little difference in the temperatures predicted at TC25 or along the edges of the can.

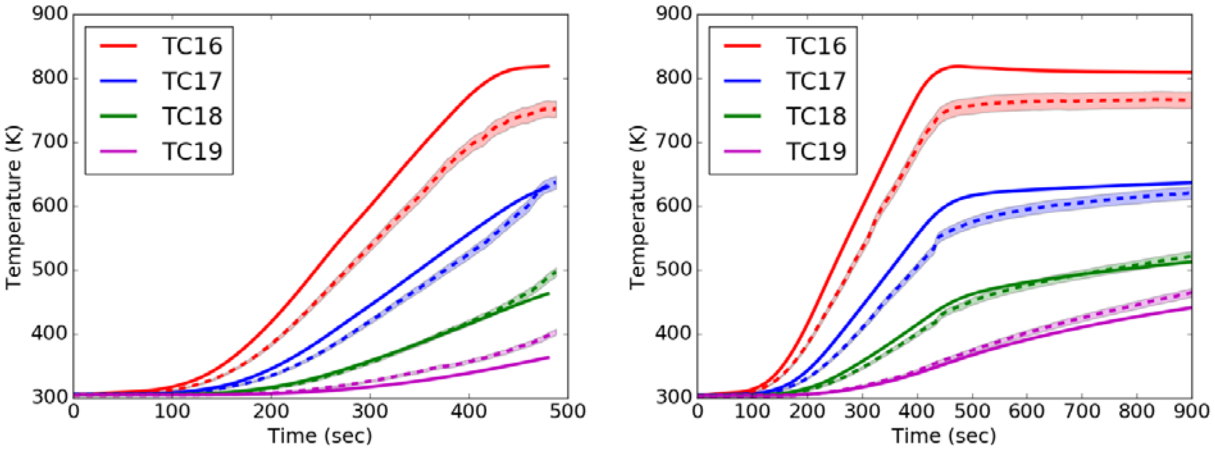

Figure 59: Separate organic liquid fraction simulation results (solid) with experimental values (dashed) for the 150 C/min heating rate for (a) inverted and (b) upright.

Comparing the optimized parameters from both studies, the permeabilities and char β_R are similar in both cases, however, there is enough difference to suggest that the parameters are not completely independent of the organic liquid fraction. The organic liquid fraction is interesting, as in the case were there is one, it is almost the average value of when there are two.

Table 22: Comparing optimized vales of 1 and 2 organic liquid fractions calibrations

	1 organic liquid fraction	**2 organic liquid fractions**
Virgin Foam Permeability [m^2]	1.55 x10^{-13}	7.76x10^{-13}
Char Foam Permeability [m^2]	7.59x10^{-8}	1.48x10^{-8}
(Upright) Organic Liquid Fraction	0.37	0.43
(Inverted) Organic Liquid Fraction		0.22
Char β_R [mK]	226	340

To validate the parameters obtained in the two Organic Liquid Fractions calibration, the 50 C/min experiments were modeled. Figure 60 shows the pressure and the temperature at TC 25. While the inverted case over predicts the pressure, it is promising that the change in slope at ~820 seconds is represented – even if the resulting slope is too high. The upright pressure is in reasonably good agreement, though the inflection of the curve is incorrect. This incorrect slope is most likely the effect of having the same fraction of excess gasses being sent to a condensed phase through the simulation. In reality, as the temperature rises, more products will be sent into the gas phase. The time at which the upright and inverted cases split from each other is also well predicted, whereas it was not in the 50 C/min 1 organic liquid fraction case. The temperatures, both of TC25 and along the sides of the can, are in similar agreement as in the 1 organic liquid fraction case.

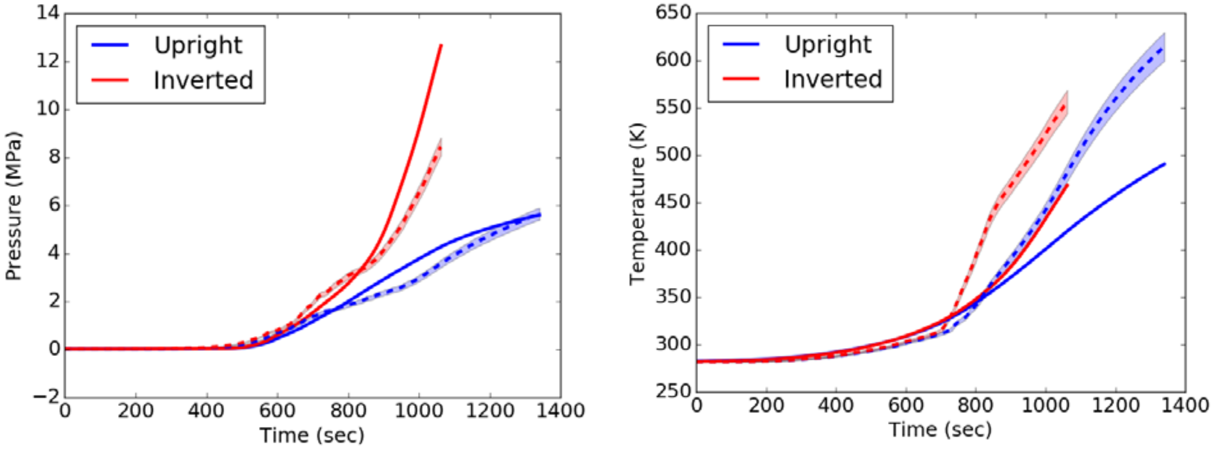

Figure 60: Simulation results (solid) with experimental values (dashed) for the 50 C/min heating rate for (a) pressure and (b) temperature of the embedded object (TC 25).

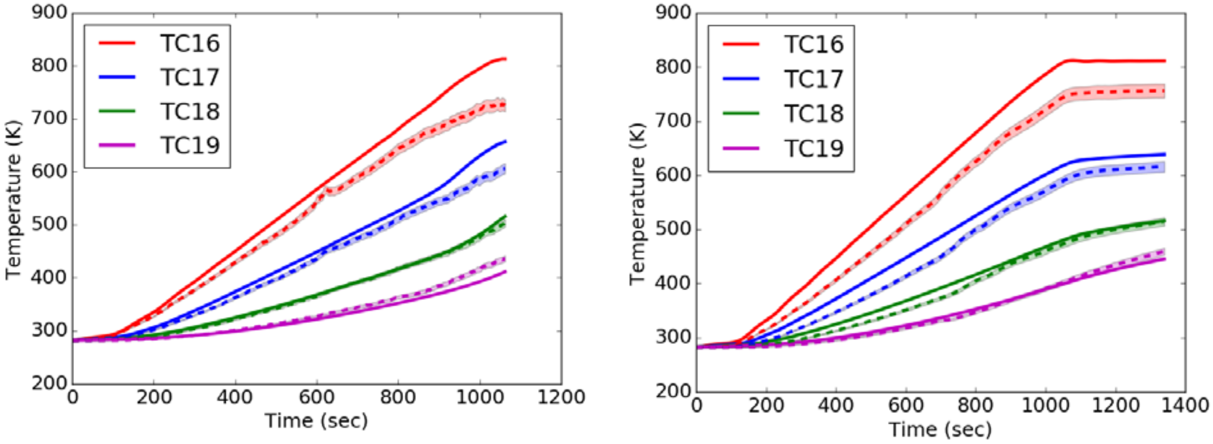

Figure 61: Simulation results (solid) with experimental values (dashed) for the 50 C/min heating rate for (a) inverted and (b) upright.

4.5. Remarks

The porous media formulation differentiates the temperature and pressure response as a function of orientation as seen in the experiments – something not previously achieved using the No Flow Model. Additional progress was made through the implementation of the orientation-dependent organic liquid fraction. While the Porous Media model could predict a dependence on orientation, brought on by buoyant flow, better agreement was found when orientation-dependent organic liquid fraction values were used, particularly in the 50 C/min case. This corroborates the idea that liquid foam is dripping onto the hot plate and causing more rapid decomposition in the inverted case. It also supports the case for developing a liquid vapor equilibrium model for the foam, as well as the ability to track the motion of the condensed phase.

The weak agreement of the thermocouples points to the need for further investigation into the mechanisms of heat transfer.

5. POROUS MEDIA WITH VAPOR LIQUID EQUILIBRIUM (VLE) MODEL

The use of separate organic liquid fractions for the inverted and upright orientations, as discussed in the previous section, illustrates the need for a more sophisticated method for determining the phase of the decomposition products. A vapor liquid equilibrium (VLE) model was implemented in order to determine the gas/vapor split of the decomposition products.

5.1. 5.1 Description of model

5.1.1. Fundamentals of VLE

For a pure substance, the Gibbs function is defined as:

$$G = H - TS \tag{47}$$

Where *H* is the enthalpy, *T* is the temperature, and *S* is the entropy. Using the definition of entropy, the differential Gibbs function for a pure substance can be written as:

$$dG = VdP - SdT \tag{48}$$

For a mixture, the total Gibbs function is a function of two independent intensive properties (e.g., temperature and pressure) and the composition. In differential form, it is:

$$dG = \left(\frac{\partial G}{\partial P}\right)_{T,n} dP + \left(\frac{\partial G}{\partial T}\right)_{P,n} dT + \left(\frac{\partial G}{\partial n_i}\right)_{T,P,n_j} dn_i \tag{49}$$

Where n_i is the number of mole of component *i* and n_j indicates that all species that are not species *i* are held constant. Combining Eq 48 and 49:

$$dG = VdP - SdT + \sum \mu_i dn_i \tag{50}$$

Where μ_i is the chemical potential of *i* and is defined as the change in the Gibbs function due to changing the number of moles, in a given phase, of species *i* while holding everything else constant [58].

$$\mu_i = \left(\frac{\partial G}{\partial n_i}\right)_{T,P,n_j} \tag{51}$$

A system at a constant temperature and pressure is said to be in equilibrium when the change in the Gibbs function is equal to zero. In other words:

$$(dG)_{T,P} = 0 \tag{52}$$

Evaluating Eq 50 at constant temperature and pressure yields the Gibbs-Duhem equation [62]:

$$(dG)_{T,P} = \sum \mu_i dn_i = 0 \tag{53}$$

If species *i* is split between two phases (in this case, liquid and gas), then,

$$(dG)_{T,P} = \sum (\mu_{l,i} dn_{l,i} + \mu_{v,i} dn_{v,i}) = 0 \tag{54}$$

Since any material that is moved out of one phase goes into the other:

$$(dG)_{T,P} = \sum \left(\mu_{l,i} - \mu_{g,i}\right) dn_i = 0 \tag{55}$$

If we assume that dn_i is not equal to zero, then the chemical potential in the liquid and gas phases must be equal to each other [62]. This is known as the vapor liquid equilibrium condition.

$$\mu_{g,i} = \mu_{l,i} \tag{56}$$

For species i, the following definition can be made:

$$\frac{G_i}{n_i} = G_{m,i} = \mu_i \tag{57}$$

Where $G_{m,i}$ is the molar Gibbs free energy. For a single component:

$$dG_{m,i} = V_{m,i} dP - S_{m,i} dT \tag{58}$$

If the temperature is held constant [62],

$$dG_{m,i} = V_{m,i} dP \tag{59}$$

Using the definition from Eq 57:

$$d\mu_i = V_{m,i} dP \tag{60}$$

In order to solve for μ, temperature can be held constant and the expression can be integrated with respect to pressure:

$$\int_{P^0}^{P_i} d\mu_i = \int_{P^0}^{P_i} V_{m,i} dP \tag{61}$$

Where P^0 is the reference state. While the left-hand side is trivial, the right hand side is not. There are a couple of ways this can be dealt with, for example, the ideal gas assumption. That leads to the following expression:

$$\mu_{v,i}(P_i) = \mu_{v,i}^0 + RTln\left(\frac{P_i}{P^0}\right) \tag{62}$$

Where μ^0 is the standard chemical potential evaluated at P^0 (typically 1 bar) and R is the universal gas constant [62].

For a more general case (either in the liquid or gas phase), the fugacity (*f)* can be used.

$$\mu_i(P_i) = \mu_i^0 + RTln\left(\frac{f_i}{f^0}\right) \tag{63}$$

The fugacity accounts for a substances deviation from ideal, while still allowing the use of an equation that takes a similar form as though the ideal gas law were used. For a pure vapor, the fugacity for a gas is defined as:

$$f^v = \phi_{pure}^v P \tag{64}$$

Where ϕ_{pure}^v is the fugacity coefficient for the pure substance. In other words, the fugacity coefficient is an experimentally determined factor that accounts for non-ideality. In a mixture, the fugacity is similar; however, the fugacity coefficient ϕ_i^v is not equal to the pure coefficient.

$$f_i^v = \phi_i^v P y_i \tag{65}$$

Also, the partial pressure rather than the total pressure is used. This requires that pressure be multiplied by y_i, the mole faction of in the gas phase. In other words:

$$y_i = \frac{n_i^v}{\sum n_i^v} \tag{66}$$

In a pure liquid, the fugacity is [63]:

$$f^l = \phi^{sat} P^{sat} exp\left[\frac{1}{RT}\int_{Psat}^{P} V_m^l dP\right] \tag{67}$$

This takes a similar form as the fugacity for a pure gas, but with an added exponential term. This is known as the Poynting factor and accounts for the pressure’s influence on the liquid. This is typically nearly equal to one, unless the pressure is high (around 5 MPa).

In a liquid solution, since there is no good model for the fugacity coefficient, the activity coefficient (γ) and the mole fraction in the liquid phase (x_i) are used to relate the fugacity of the pure species to that of the mixture.

$$f_i^l = \gamma_i x_i f^l = \gamma_i x_i \phi_i^{sat} P_i^{sat} exp\left[\frac{1}{RT}\int_{P_i^{sat}}^{P} V_{m,i}^l dP\right] \tag{68}$$

For clarity, the mole fraction in the liquid phase is defined as,

$$x_i = \frac{n_i^l}{\sum n_i^l} \tag{69}$$

Since the chemical potentials of the liquid and gas phase are equal at equilibrium, this leads to:

$$f_i^l = f_i^v \tag{70}$$

or:

$$\phi_i^v P y_i = \gamma_i x_i \phi_i^{sat} P_i^{sat} exp\left[\frac{1}{RT}\int_{P_i^{sat}}^{P} V_{m,i}^l dP\right] \tag{71}$$

It is convenient to define the K-value:

$$K_i = \frac{y_i}{x_i} \tag{72}$$

5.1.1.1. Raoult's Law

Many aspects of how to handle VLE calculations are described in Skogestad [63] including manipulations of Raoult’s and Henry’s laws. The majority of the following sections use that work as a reference.

Raoult's law is a simplification of Eq 71. It assumes an ideal liquid mixture and an ideal gas, therefore ϕ_i^v, ϕ_i^{sat}, γ_i are equal to one. In addition, the Poynting factor is equal to one. This results in the following:

$$P y_i = x_i P_i^{sat}(T) \tag{73}$$

Or

$$K_i = \frac{y_i}{x_i} = \frac{P_i^{sat}(T)}{P} \tag{74}$$

One limitation of Raoult’s law is that it cannot be used above the critical temperature, since $P_i^{sat}(T)$ is no longer defined. Since the critical temperatures of the decomposition products of interest range between 300 K and 700 K, another formulation should be considered.

5.1.1.2. Raoult's Law: Bubble Point

At the bubble point, gas is just starting to form. Thus, the liquid phase mole fractions, x_i, are known, since it’s just the mole fraction given by the decomposition equation. For a given temperature or pressure, the other must be adjusted to fit the constraint that the sums of the vapor fractions are one ($\sum y_i = 1$). From the definition in Eq 72, this means that,

$$\Sigma y_i = \Sigma K_i x_i = 1 \tag{75}$$

At this point, Raoult's law can be used to define K_i and solve for pressure.

$$P = \Sigma P_i^{sat}(T) x_i \tag{76}$$

5.1.1.3. Raoult's Law: Dew Point

At the dew point, the liquid phase is just starting to form. This time, it is the gas phase mole fractions, y_i, that are known. Since the sum of the mole fractions in the liquid phase must sum to one ($\sum x_i = 1$), Eq 72 gives:

$$\Sigma x_i = \sum \frac{y_i}{K_i} = 1 \tag{77}$$

At this point, Raoult's saw can be used to define K_i and solve for pressure.

$$\frac{1}{P} = \sum \frac{y_i}{P_i^{sat}(T)} \tag{78}$$

5.1.1.4. Henry’s Law

For dilute mixtures, there is generally a linear relationship between the gas phase fugacity and the liquid concentration.

$$f_i^l = H_i(T)\, x_i \tag{79}$$

This is known as Henry’s law, and H is Henry’s constant. Henry’s constant can be assumed to be only a function of temperature for intermediate pressure ranges (up to 5 MPa). Assuming the gas is ideal (and therefore the fugacity coefficient is 1) Eq 64 gives,

$$f_i^v = \phi_i^v P y_i = P y_i \quad (80)$$

Combing Eq 73 and 74 gives a relationship between the pressure and the mole fractions in the liquid and gas phase.

$$P y_i = H_i(T)\, x_i \quad (81)$$

Or

$$K_i = \frac{y_i}{x_i} = \frac{H_i(T)}{P} \quad (82)$$

This formulation is valid for dilute mixtures (x_i < 0.03) and low pressures (P < 2 MPa). In addition, since the mixture is dilute, Raoult's law can be used to determine the properties of the solvent.

A note on Henry's constant. There are several different ways that Henry's constant can be presented:

(1)	(2)	(3)	(4)	(5)
$K_H^{pc} = \frac{P}{c_{i,l}}$	$H^{cp} = \frac{c_{i,l}}{P}$	$K_H^{px} = \frac{P}{x_i}$	$H^{xp} = \frac{x_i}{P}$	$H^{cc} = \frac{c_{i,l}}{c_{i,g}}$
$\left[\frac{m^3\ Pa}{mol}\right]$	$\left[\frac{mol}{m^3\ Pa}\right]$	$[Pa]$	$[1/Pa]$	$[dimensionless]$

Eq 81 or 82 requires Henry's constant to be in the (3) presentation. Thus, the following conversions can be used:

$$H^{cc} = H^{cp}\, RT \quad (83)$$

$$H^{xp} = \frac{M_{solvent}}{\rho_{solvent}} H^{cp} \quad (84)$$

5.1.1.5. Henry's coefficient as a function of temperature

Many times, Henry's coefficient is only reported at room temperature, despite being temperature dependent. There are methods to extrapolate the constant to another temperature. The most applicable is the Van't Hoff extrapolation [64].

$$\frac{H_i(T_1)}{H_i(T_0)} \approx exp\left[\frac{\Delta H_{sol}}{R}\left(\frac{1}{T_1} - \frac{1}{T_0}\right)\right] \quad (85)$$

Where ΔH_{sol} is the solute enthalpy of solution over a modest temperature range.

5.1.1.6. Henry's Law: Bubble Point

Eq 75 still holds for Henry's law. What changes is how K_i is defined. Using Henry's law to define K_i and solve for pressure yields,

$$P = \Sigma H_i(T)x_i \qquad 86$$

5.1.1.7. Henry's Law: Dew Point

As in the bubble point case, Eq 77 holds and using Henry's law to define K_i and solve for pressure yields,

$$\frac{1}{P} = \sum \frac{y_i}{H_i(T)} \qquad 87$$

5.1.2. Composition

One method of calculating the fraction of each species in the liquid or gas phase at equilibrium is using a flash equation [63]. This equation supposes there is a feed of a specific, known, composition (z_i) that at a certain temperature and pressure will split into a liquid and a vapor. Conservation on a species basis gives:

$$Fz_i = Lx_i + Vy_i \qquad 88$$

Where *F* is the moles of feed, L is the moles of liquid, and *V* is the moles of vapor. Using the definition of the K-factor (Eq 72), y_i can be written in terms of x_i and plugged into Eq 88.

$$Fz_i = Lx_i + VK_ix_i \qquad 89$$

Solving for x_i:

$$x_i = \frac{Fz_i}{L + VK_i} \qquad 90$$

The conservation equation can also be written as:

$$L = F - V \qquad 91$$

And then plugged into Eq 90.

$$x_i = \frac{z_i}{1 + \frac{V}{F}(K_i - 1)} \quad 92$$

Since the definition of mole fraction is that the sum of all the mole fractions is equal to one, the following is also true:

$$\sum y_i - x_i = 0 \quad 93$$

Using Eq 72 and Eq 90, an expression for y_i is created.

$$y_i = \frac{K_i z_i}{1 + \frac{V}{F}(K_i - 1)} \quad 94$$

Plugging Eq 90 and 93 into 94:

$$\sum y_i - x_i = \sum \frac{K_i z_i}{1 + \frac{V}{F}(K_i - 1)} - \frac{z_i}{1 + \frac{V}{F}(K_i - 1)} = 0 \quad 95$$

Yields:

$$\sum \frac{z_i(K_i - 1)}{1 + \frac{V}{F}(K_i - 1)} = 0 \quad 96$$

That is known as the Rachford-Rice equation. This can be numerically solved for to find the vapor split. Once this is known, *V/F* can be plugged back into Eq 90 and 94, to determine x_i and y_i.

A convenient feature of this equation is the use of the K-factor, allowing the equation to be rather general, since most of the assumptions regarding how ideal the mixture is lies in the definition of *K*.

5.1.3. Vapor Quality

The quality of a mixture is a measure of the mass fraction of the mixture that is in the gas phase. It is defined as:

$$X_i = \frac{m_g}{m_g + m_l} \quad 97$$

From the conservation equation (Eq 91), the global vapor and liquid fraction can be written in terms of the vapor split (which was solved for in 96) [36]:

$$V = \frac{V}{F} F \tag{98}$$

$$L = F - V = F - \frac{V}{F} F = F\left(1 - \frac{V}{F}\right) \tag{99}$$

Since these equations are molar quantities, they need to be translated into mass quantities:

$$V_{mass} = M_{feed,total}\ \frac{V}{F} F \tag{100}$$

$$L_{mass} = M_{feed,total}\ F\left(1 - \frac{V}{F}\right) \tag{101}$$

Where

$$M_{feed,total} = \sum z_i M_i \tag{102}$$

Where M_i is the molar mass. With an expression for the total mass of liquid and gas, the mass of each species must be computed. First, the mole fraction must be rewritten as the mass fraction. The mass fraction of species *i* in the liquid phase is:

$$w_i = x_i\ \frac{M_i}{\sum x_i M_i} \tag{103}$$

And in the gas phase:

$$u_i = y_i\ \frac{M_i}{\sum y_i M_i} \tag{104}$$

Therefore, the quality is:

$$X_i = \frac{V_{mass} u_i}{V_{mass} u_i + L_{mass} w_i} = \frac{\frac{V}{F}\ u_i}{\frac{V}{F}\ u_i + \left(1 - \frac{V}{F}\right) w_i} \tag{105}$$

Similarly, the quality on a mole fraction basis would be:

$$X_{i,mole} = \frac{Vy_i}{Vy_i + Lx_i} = \frac{\frac{V}{F}\, y_i}{\frac{V}{F}\, y_i + \left(1 - \frac{V}{F}\right) x_i} \qquad 106$$

5.1.4. *Vapor Pressure*

If using Raoult's law is applicable, then it is necessary to know the saturation pressure at a given temperature. This can be found using the Antoine equation.

$$\log_{10}(P_{sat}) = A - \frac{B}{T + C} \qquad 107$$

Where *A*,*B,* and *C* are empirically derived constants. Another method is the Unger-Suuberg correlation (Eq 108), which was used successfully by Fletcher *et al.* to model vapor pressure for coal pyrolysis [65].

$$P_i^v = \alpha \exp\left(\frac{-\beta\, M_i^\gamma}{T}\right) \qquad 108$$

Where *M* is the molecular weight of the i^{th} polymer.

Table 23: Coefficients used by various authors (note that these constants require units of Kelvin and atm)

	α	β	γ
Unger-Suuberg	5756	255	0.586
Fletcher e*t al.*	87060	299	0.590

The boiling points at pressures ranging from 0.066 atm to 10 atm of 111 pure organic compounds that are thought to be products of coal pyrolysis were compared to the correlation, with good agreement. These organic compounds had molecular weights up to 244, but did not include long chain hydrocarbons or compounds with more than two oxygen atoms.

5.1.5. *Application of VLE to PMDI RPU Foam in a Can*

It is assumed that the global reaction for PMDI RPU, as determined by Ericson [6], is:

$$PMDI\ RPU\ \rightarrow 0.25\ CO_2 + 0.20\ LMWO + 0.35\ HMWO + 0.2\ char \qquad 109$$

However, it is important to note that the coefficients in this equation are for the mass fractions. The equation can be rewritten on a mole fraction basis, which only considers the gas and liquid decomposition products.

$$PMDI\ RPU_{gas,liqid} \rightarrow 0.51\ CO_2 + 0.23\ LMWO + 0.26\ HMWO \tag{110}$$

One issue with Ericson's formulation, when attempting to use it to implement a VLE, is the lack of information about how the low and high weight organics behave. However, both Ericson [7] and Nemer [8] have analyzed the decomposition products, thus there is some knowledge of what these organics could be.

Table 24: Thermochemical information for major decomposition products

Molecule	Formula	Molar Mass	Critical temperature (K)	Critical pressure (MPa)
Phenyl isocyanate [e]	C7H5NO	119	650	4
Aniline [b]	C6H5NH2	93	698	4.89
4-methylaniline [c]	C7H9N	107	667	2.4
Propylene glycol [d]	C3H8O2	76	624	6.1
Water vapor [a]	H2O	18	647	22.06
Ammonia [a]	NH3	17	405	11.28
Carbon dioxide [a]	CO2	44	304	7.39

[a] Cengel, [b] https://en.wikipedia.org/wiki/Aniline_(data_page)#Thermodynamic_properties, [c] http://pubchem.ncbi.nlm.nih.gov/compound/p-Toluidine#section=Fire-Potential, [d] http://stenutz.eu/chem/solv6.php?name=propylene%20glycol, [e] http://pubs.acs.org/doi/pdf/10.1021/je060269j

In order to simplify the problem, it has been assumed that all of the organic decomposition products can be represented at aniline.

$$PMDI\ RPU_{gas,liqid} \rightarrow 0.51\ CO_2 + 0.49\ Aniline \tag{111}$$

5.1.5.1. An Exploration of Vapor Pressure

Calculating the vapor pressure for a given temperature can be achieved by using the Antoine equation. Table 25 shows the coefficients for the major decomposition products.

Table 25: Antoine coefficients and the temperature range over which they are applicable for organic decomposition products, where the Antoine equation requires temperature in K and pressure in Pa [66]

Molecule	Temperature Range [K]	A	B	C
Phenyl isocyanate	283.8 - 438.8	9.52289	1800.757	-40.303
Aniline	304 - 457	9.34541	1661.858	-74.048
4-methylaniline	315 - 473.6	9.71884	1961.716	-57.00
Propylene glycol	318.7 - 461.4	11.07936	2692.187	-17.94

Figure 62 compares the Antoine equation, the Unger-Suuberg correlation with the original coefficients, and the Unger-Suuberg correlation with Fletcher *et al.*'s coefficients over the temperature range in which the Antoine coefficients were fit. It is interesting to note that the Unger-Suuberg coefficients tend to match the Antoine equation better, except in the case of phenyl isocyanate. This is perhaps because the Fletcher *et al.* coefficients were derived using heavier molecules.

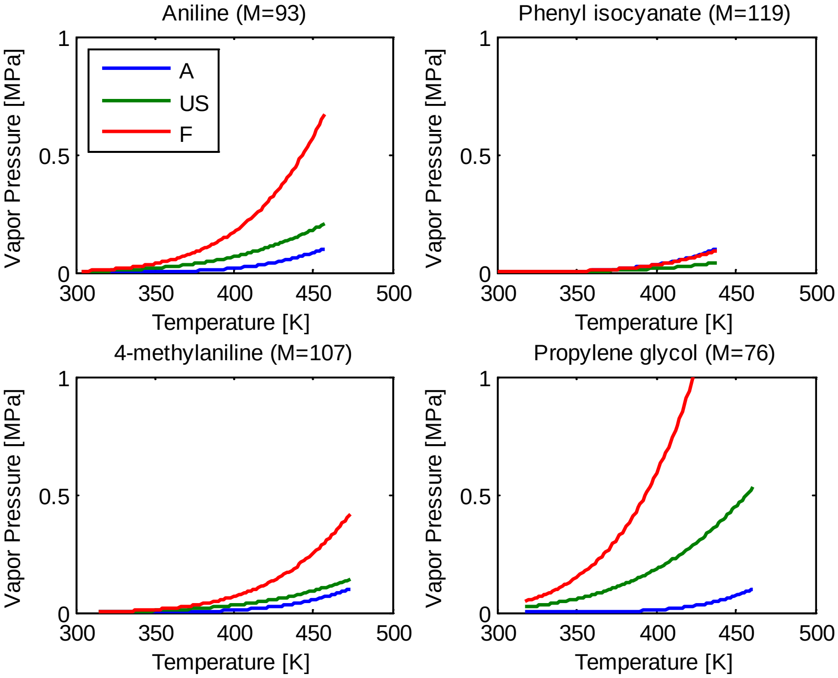

Figure 62: Vapor pressure vs temperature for the major organic decomposition products. The vapor pressure is calculated using the Antoine equation (A), the Unger-Suuberg correlation with the original coefficients (UG), and the Unger-Suuberg correlation with Fletcher *et al.'s* coefficients (F). The temperature is limited to the range over which the Antoine equation was derived.

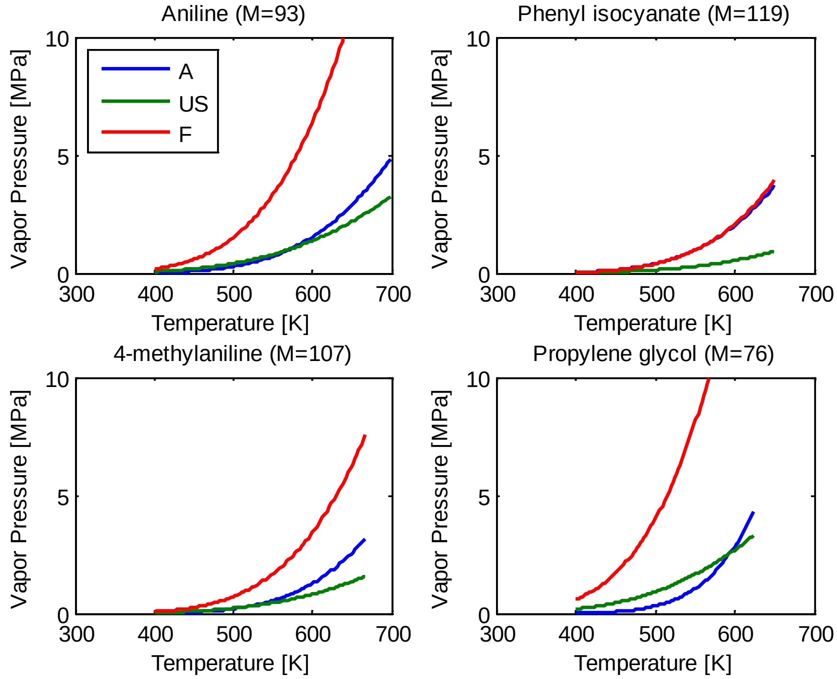

Figure 63: Vapor pressure vs temperature for the major organic decomposition products. The vapor pressure is calculated using the Antoine equation (A), the Unger-Suuberg correlation with the original coefficients (UG), and the Unger-Suuberg correlation with Fletcher *et al.'s* coefficients (F). The temperature is limited to the critical temperature.

One issue is that these constants were fitted from experiments in a particular temperature range, which is also stated in Table 25. Unfortunately, the FIC experiments exceed this temperature range. Figure 63 shows the three ways to calculate the vapor pressure extrapolated to the critical temperature of each organic.

Hobbs *et al.* used the Unger-Suuberg correlation with Fletcher e*t al.*'s coefficients to model the decomposition of TDI rigid polyurethane foam [67]. This method is convenient, because the only information about the molecules that is needed is their molecular weights and is therefore very useful when using a system like a kinetic bond-break scheme to create the decomposition products. The major difference between Hobbs' work and the current work is that this system is confined. Thus, the carbon dioxide, despite being supercritical, can dissolve into the liquid. The Unger-Suuberg correlation is not prepared to handle that, and thus Henry's law must still be relied upon.

5.1.5.2. Raoult's Law

Raoult's law is the simplest way to model a multi component system. However, in order for it to work, the constituents cannot be above the critical point. As seen in Table 24, our scenarios of interest violate this assumption for carbon dioxide. Therefore, it will only be used alongside Henry's law to determine the vapor split of this system.

5.1.5.3. Henry's Law

Since Henry's law can be used above a component's critical temperature, it is more appropriate to use for carbon dioxide at the relevant temperatures and pressures. The Henry's coefficient used was 1702 [Pa m^3/mol], and was measured at 292 K [68].

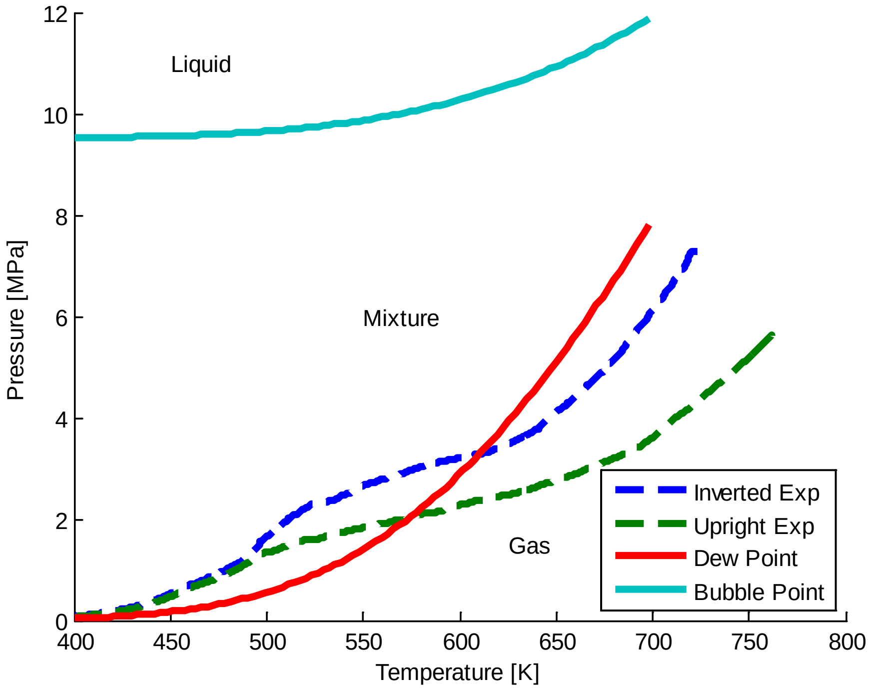

Figure 64: Average gas temperature vs Pressure for the 50 C/min experiment displayed with the dew and bubble point calculated using both Raoult's and Henry's Law

Figure 64 shows the dew and bubble points calculated using Henry's law for the carbon dioxide and Raoult's law for the aniline. The pressure and temperature traces for the inverted and upright experiments are also shown. This indicates that there is most likely a mixture of liquid and vapor decomposition products when the foam decomposes.

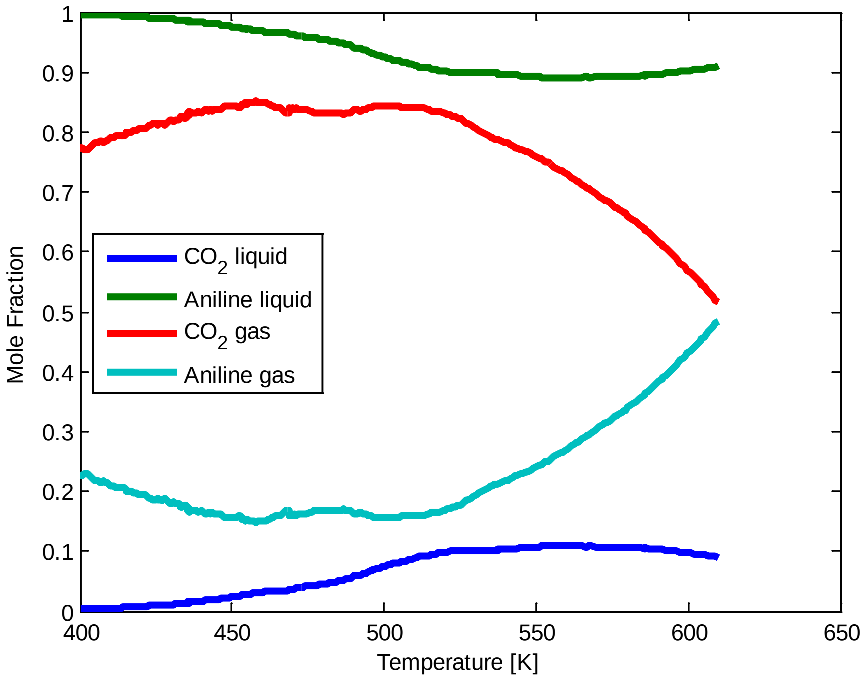

Figure 65: Mole fractions in the liquid (x_i) and gas (y_i) phases for carbon dioxide and aniline

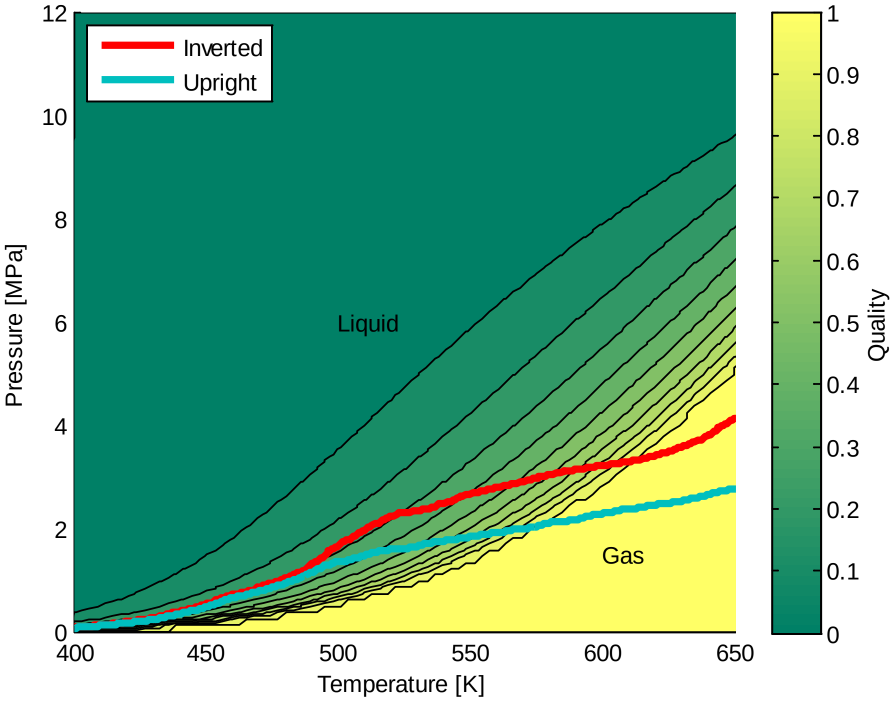

Figure 66: Average gas temperature vs Pressure for the 50 C/min experiment displayed with the mass vapor quality of aniline

Figure 65 shows the mole fraction of the liquid and gas phases for carbon dioxide and aniline, using the inverted temperature and pressure data. As would be expected, the liquid is primarily comprised of aniline, while the gas phase is a more even split. While the mole fraction of carbon dioxide in the liquid phase is low, generally below 0.1 (the mean over the temperature range is 0.05), this is still greater than the recommended limit ($x_i < 0.03$). Another issue is that the recommended pressure limit is 2 MPa, which is exceeded in the experiments.

Figure 66 shows the trace of the pressure and temperature seen in the experiments set against a quality chart of aniline. This indicates that there could be a significant amount of liquid aniline present.

5.2. Implementation of the VLE model

5.2.1. Description of Implementation

In order to implement this theory into the Sierra Thermal/Fluids code, for each species participating the vapor liquid equilibrium, a reaction represented the evaporation and condensation was created

$$CO_2^{liquid} \rightarrow CO_2^{gas} \qquad 112$$

$$HMWO^{liquid} \rightarrow HMWO^{gas} \qquad 113$$

$$LMWO^{liquid} \rightarrow LMWO^{gas} \qquad 114$$

The rate used to govern these equations is the Hertz-Knudsen equation, modified to allow for non-ideal behavior by using the fugacity of each phase in place of the pressure and saturation pressure:

$$\omega = \frac{A}{2 - C_c}\left(\frac{2}{\pi MRT}\right)^{1/2}\left(C_e f_{liquid} - C_c f_{gas}\right) \qquad 115$$

where A is the specific surface area, M is the molecular weight of the species, C_e and C_c are the evaporation and condensation coefficients, and f_{liquid} and f_{gas} are the fugacities of the species in each phase. For the purpose of this model, we are interested in modeling equilibrium and have no data on the kinetics of the phase change, the evaporation and condensations constants are set equal and to sufficiently large such that the equilibrium is maintained, but the kinetics are not unnecessarily stiff. Each gas phase species is ideal, therefore the $f_{gas} = P_i$ where P_i is the partial pressure and of the species and modeled using the Antonine equation (equation 107). The fugacity of CO_2 is modeled using Henry's law (equation 81), since we are interested in regimes about the critical pressure of CO_2.

5.2.2. Initial testing

The Vapor Liquid Equilibrium model is an addition to the Porous Media model. A finite element model composed of tetrahedral elements was evaluated in the Sierra Thermal/Fluids [16] code to computationally simulate the FIC experimental configuration (Figure 71). A three-step reaction mechanism reacts PMDI polyurethane foam from into carbon dioxide, light and heavy molecular weight organics, and char. The mass fraction of organics in the gas and condense are determined through the VLE equations. Pressurization is calculated using the ideal gas law. A radiative boundary condition is used to heat one end of the can, while convection and radiation cool the remaining surfaces. Foam effective conductivity, porosity and permeability are a function of reaction while other properties are constant or a function of temperature. The continuity, species, and enthalpy equation are solved in both the condensed and gas phases. The following section will give a detailed description of the model.

Initial testing of the VLE implementation revealed that the mass fractions of the condensed phase of the decomposition products would go negative, causing the simulations to crash. Testing on the 3D foam in a can model was impractical, due to the number of processors needed and the time needed to run a single simulation, therefore a 2D model was created.

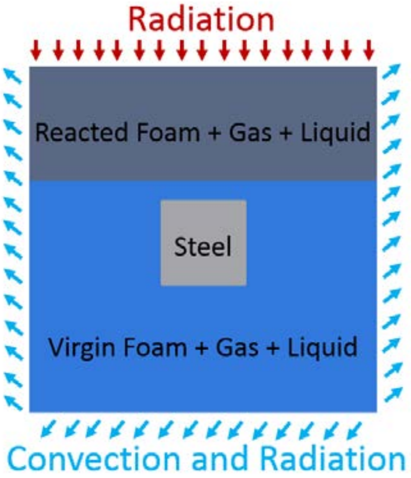

Figure 67: Schematic of the 2D VLE model for a Block

The 2D model would run to completion, however, it showed that the condensed mass fraction would go negative before returning to (near) zero in the inverted case. In the upright case, this did not occur. It was postulated that the problem appeared in only the inverted orientation because the decomposed gases where advecting to the cooler, virgin foam region, where it condenses. When the decomposition front would reach the condensed liquid and attempt to re-gasify it, this is when the negative mass fraction would occur.

The 2D model was still prohibitively slow for debugging (on the order of an hour run time) so a Five Element model was created. In order to replicate the behavior, a source of decomposition products that would condense and then gasify, representing the material that had decomposed in other cells of the 2D problem, had to be added. This was done by taking the mass fraction output from the 2D model (y_i), changing it to mole fraction (x_i), and using the ideal gas law (Eq. 118) along with the law of partial pressures (Eq. 117) to solve for the density for each decomposition product.

$$x_i = \frac{y_i/M_i}{\sum_i y_i/M_i} \qquad 116$$

$$P_i = x_i P_T \qquad 117$$

$$\frac{x_i P_T M_i}{RT} = \frac{m_i}{V} \qquad 118$$

A change was made to the code to prevent the negative mass fraction. Equation 115 is multiplied by a limiter:

$$limiter = 0.5\left(1 + tanh\left(\frac{\kappa_{reactant}}{\kappa_{product}} - 2 * \delta\right)/\delta\right) \qquad 119$$

where $\kappa_{reactant}$ is the molar density of the reactant clipped to be positive, $\kappa_{product}$ is the molar density of the product clipped to be grater than 1E-10 to avoid divide by zero, and δ = 1E-5. Whether the gas or liquid is the reactant vs product is determined based on the direction of the reaction not including the limiter. Clipping the reactants and the products prevented the non-physical negative situation, and including the hyperbolic tangent removed oscillations as equation 115 approached zero.

5.2.3. 5.3.1 2D Block Model

A 2D model of PMDI polyurethane foam surrounding a block of steel was created (Figure 67). The heating rate was 50°C/min, and was applied in both the inverted and upright orientations (for upright the heat was applied to the top of the block, in the inverted, the bottom).

One obstacle in using the VLE Model was populating the vaporization/condensation properties of the decomposition products. As discussed in section 5.1.5, Erickson [7] and Nemer [8] have analyzed the decomposition products, thus there is some knowledge of what these organics could be. Since the PMDI model already had two 'catch all' quantities for organic decomposition product, low molecular weight organics (LMWO) and high molecular weight organics (HMWO), the top four products listed by Erickson and Nemer were separated, by molecular weight, into one of these categories. Propylene glycol and aniline were 'light' organics and 4-methylaniline and phenyl isocyanate were 'heavy'.

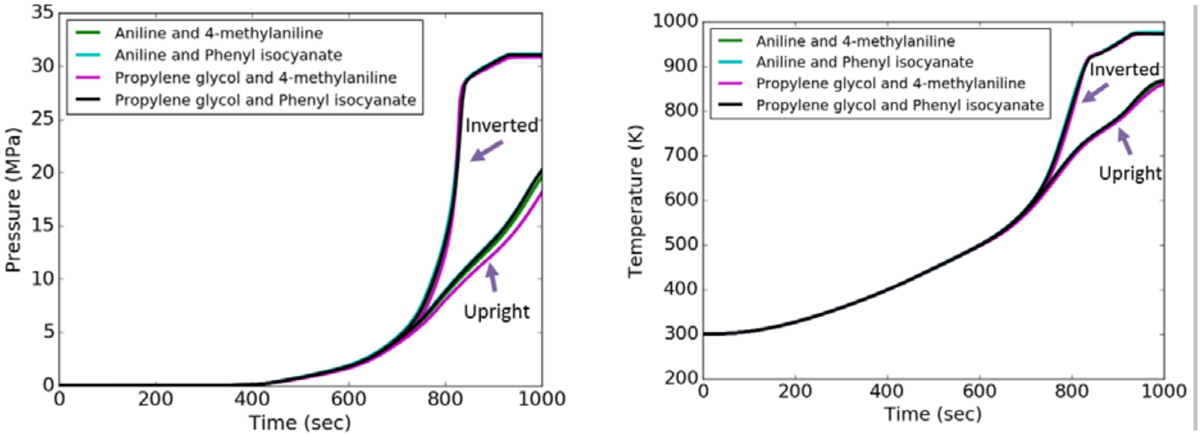

(a) (b)

Figure 68: Plots, over time, of (a) pressure and (b) temperature for the 2D block problem. Four combinations of representative decomposition products are compared.

All four permeations of these organic decomposition products were tested, and is shown in Figure 68. These results show that within our range of candidate decomposition products, there is not a strong effect on the pressure or temperature. Therefore, future studies will use the saturation pressure of aniline as the LMWO and 4-methylaniline as the HMWO.

Figure 67 shows 2D plots of temperature, aniline mass concentration (the mass of aniline per element), and aniline quality (if it is in the gas or liquid phase) for the inverted and upright orientations. As expected, in hotter regions, the aniline is in the gas phase. Also interesting is how the mass concentration shows how the advected aniline condenses in the cooler regions. It is important to note that once the aniline condenses, it is motionless, and will not move again until it returns to the gas phase. The inverted case is particularly interesting, as by 900 seconds all of the foam has reacted and the temperature is such that all the liquid aniline has returned to the gas phase. Buoyant plumes can also be seen.

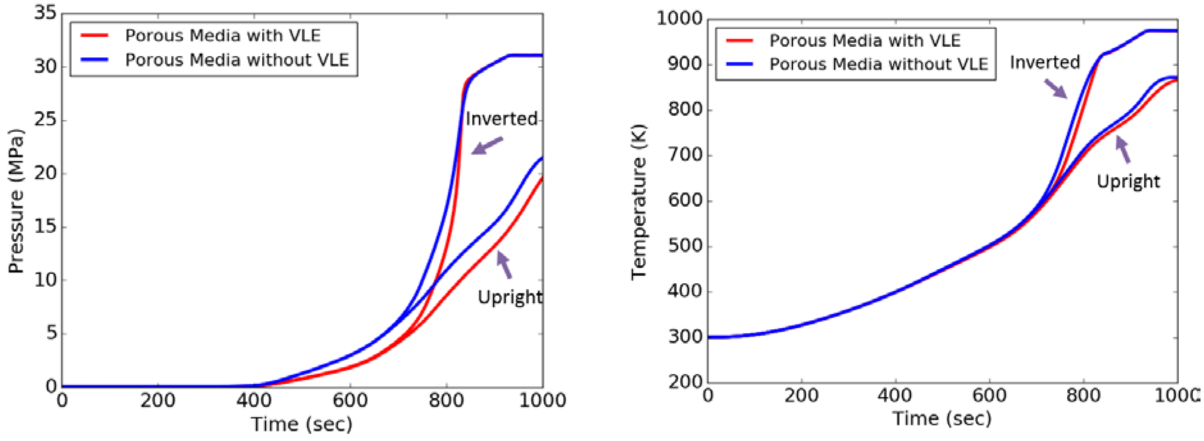

(a) (b)

Figure 69: Plots, over time, of (a) pressure and (b) temperature of the steel block for the 2D block problem, comparing the Porous Media with and without VLE models.

Figure 69 shows the time pressure and temperature traces for the 2D block, comparing the Porous Media Only and Porous Media with VLE models. As is expected, the VLE model predicts a lower pressure than the model without the VLE – this was the result that was hoped for. And reassuring aspect of these plots is that for the inverted case, after approximately 850 seconds, the two models match. Since there was no longer any liquid organics late in time, this would be the expected result.

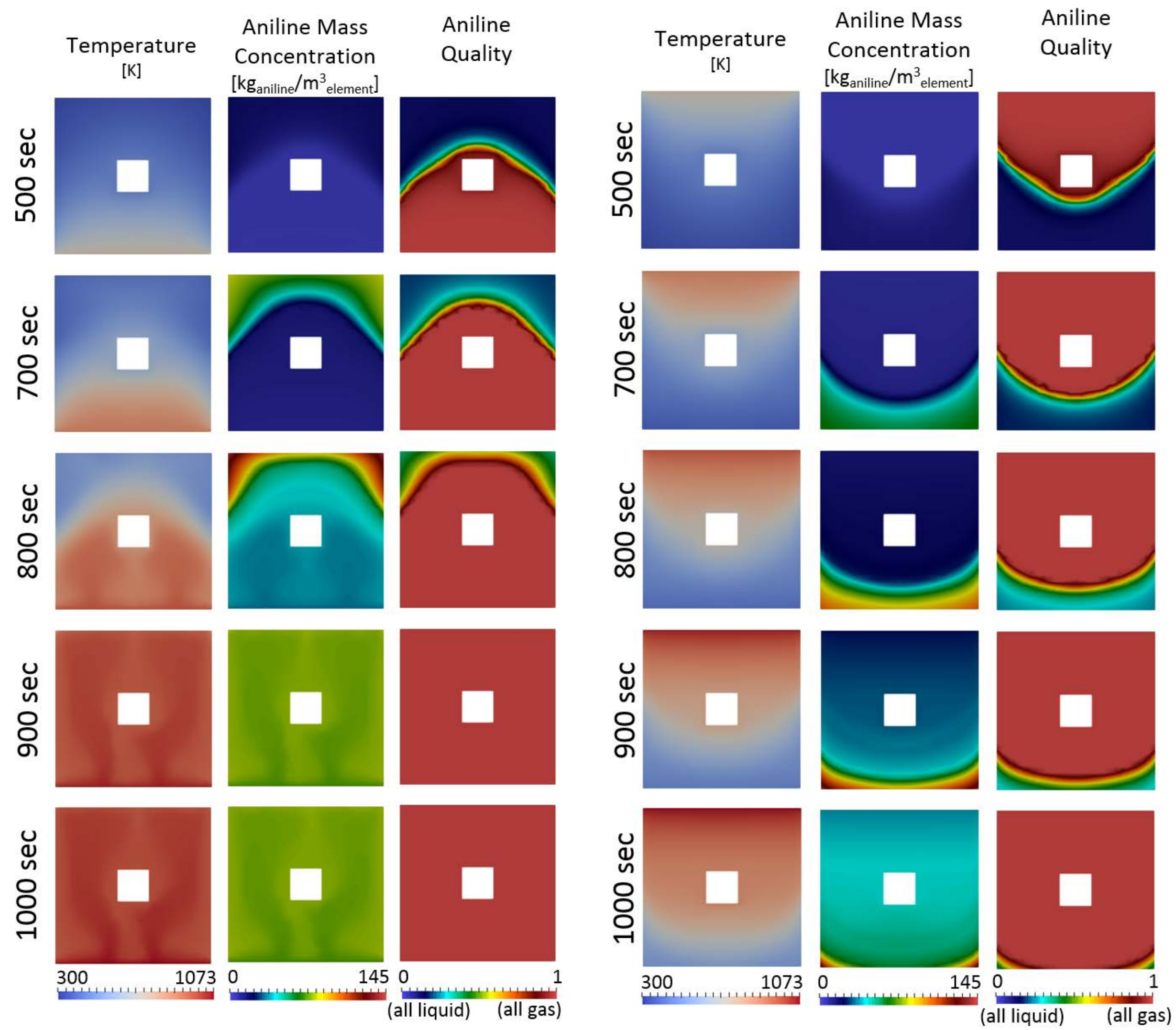

(a) (b)

Figure 70: Plots of temperature, aniline mass concentration, and aniline quality for the 2D block problem, shown at five points in time for (a) inverted and (b) upright.

5.3. 2D Foam in a Can

With the addition of the new physics, there was a desire to run a new sensitivity study. However, using the 3D model, the study would take prohibitively long. Therefore, A 2D model of Foam in a Can was created to quickly evaluate the sensitivity of the input parameters on responses.

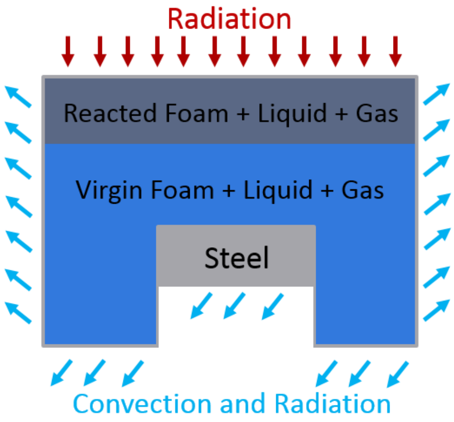

Figure 71: Schematic of the VLE model for FIC

5.3.1. Mesh Resolution Study

A quick mesh resolution study was performed to ensure that the sensitivity study would be performed on a converged mesh. Three meshes were created (Figure 72).

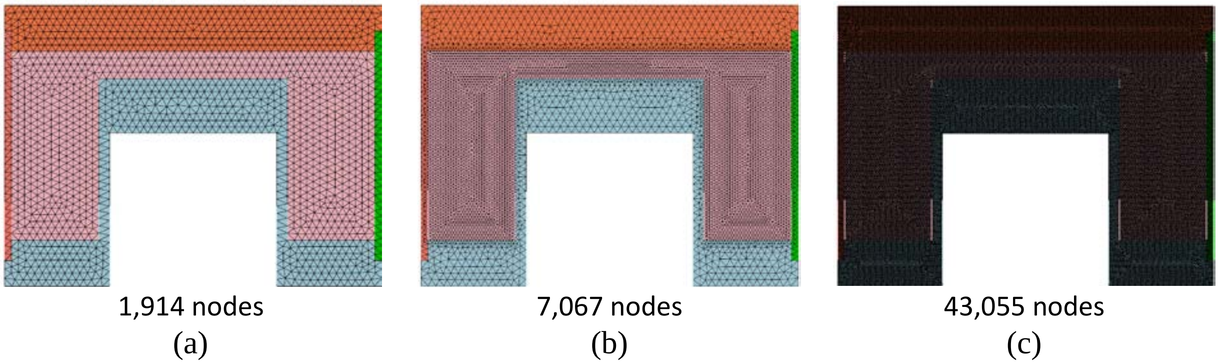

(a) (b) (c)

Figure 72: Three meshes used in the mesh resolution study and the number of nodes in the mesh (a) Coarse (b) Gradient, and (c) Finest

The first, ‘coarse,’ had elements of a similar size as the 3D version of the mesh. The second, ‘gradient’ was a more refined foam region, but coarse in the can region. The third, ‘finest’ was refined throughout the domain.

The results are shown in Figure 73. In general, all three meshes had similar results with two exceptions: the course mesh is 1 MPa lower than the other two meshes at the end of the simulation, and TC 25 is nearly 100 K cooler in the course mesh. Since there was little difference between the finest and gradient mesh, the latter was used in to evaluate the model.

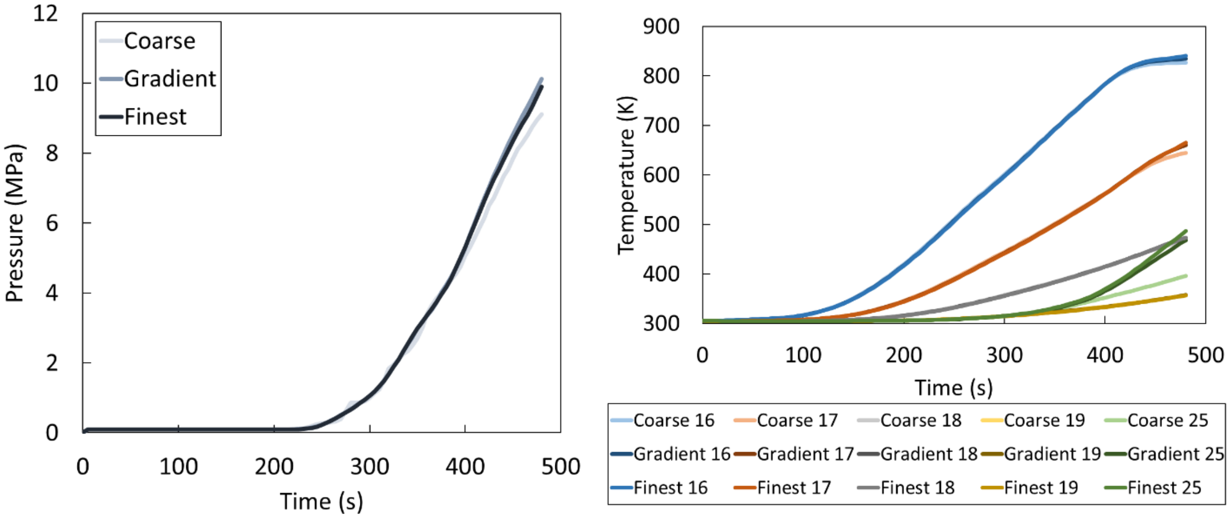

(a) (b)

Figure 73: Mesh resolution results for the Inverted 2D meshes for (a) pressure and (b) temperature

5.3.2. *Nominal Results*

Figure 75 and Figure 76 show the nominal simulation compared to experimental results. The permeability of the virgin foam and char, as well as the value for char β_R, were taken from the results of the Porous Media only optimization. (Organic liquid fraction was replaced by the vapor liquid equilibrium equations.) The results of the 2D simulations are very good in temperature, and qualitatively the pressure matches very well. One very promising result is that the upright pressure no longer has the incorrect inflection it had in the Porous Media model. Adjustments to unknown values, such as the permeability or the saturations pressures may yield better results. The sensitivity study will act as a guide in where to focus effort.

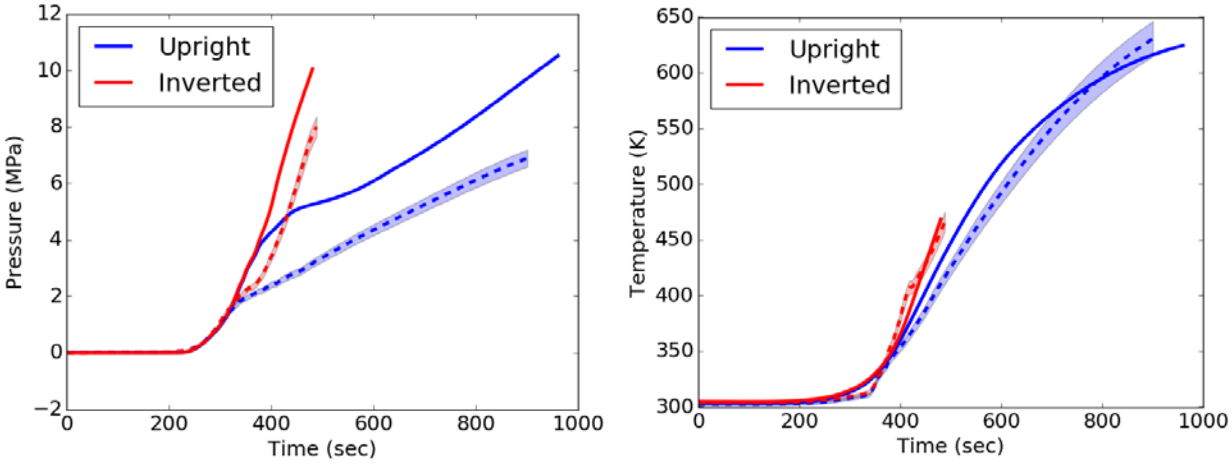

(a) (b)

Figure 74: Simulation results (solid) with experimental values (dashed) for upright (blue) and inverted (red) for the 150 °C/min heating rate for (a) pressure and (b) temperature of the embedded object (TC 25).

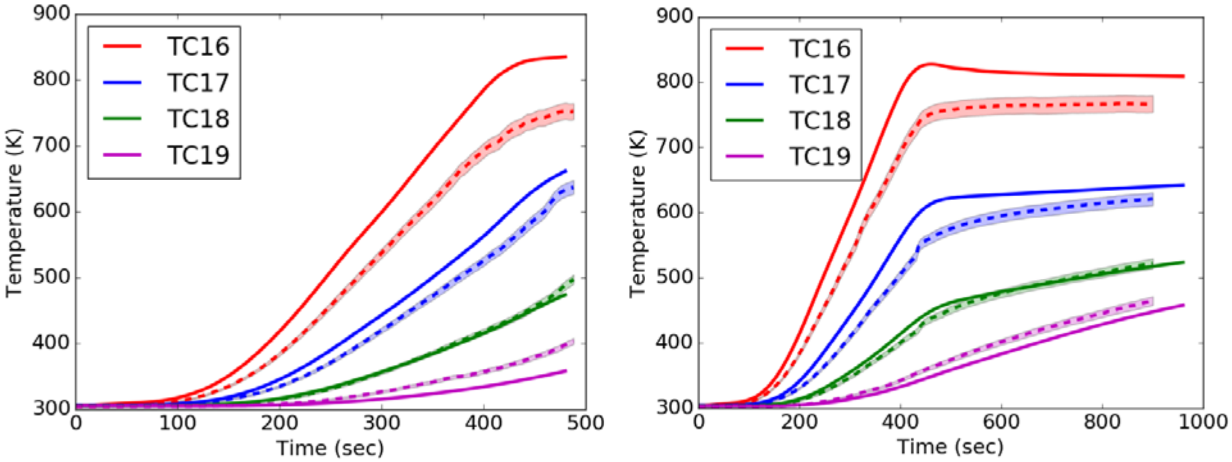

(a) (b)

Figure 75: Simulation results (solid) with experimental values (dashed) for the 150 °C/min heating rate for (a) inverted and (b) upright.

5.3.3. Uncertainty Quantification and Sensitivity Study

The uncertainty quantification and sensitivity study looked at 42 parameters, ranging from the material properties of the steel, the reaction mechanism, and the properties of the foam, including the virgin, char, gas, and liquid.

5.3.3.1. Latin Hypercube Method Background

A Latin Hypercube (LHS) approach (which does not rely on linearity) has been chosen for this sensitivity study. See Saltelli *et al.* [69] and Helton [70] for a description of the LHS method. The LHS approach and processing of the responses was performed using DAKOTA [59].

In a LHS approach, a cumulative distribution function (CDF) is specified for each parameter. Each CDF is divided into n_{LHS} intervals of equal probability. A random sample is generated from each interval for all parameters. This results in a vector of length n_{LHS} samples for each parameter

$$p_i = \left[p_{i,1}, p_{i,2}, \dots, p_{i,n_{LHS}}\right]^T \quad 120$$

The samples for each parameter are randomly combined with samples from the other parameters to give n_{LHS} random parameter vectors. The simulation is run with each of the random parameter vectors. The model response (i.e. temperature, pressure) for each random parameter vector is processed to calculate statistics (mean and standard deviation).

$$\mu_R = \frac{1}{n_{LHS}} \sum_{i}^{n_{LHS}} R_i \tag{121}$$

$$\sigma_R = \left[\frac{1}{n_{LHS} - 1} \sum_{i}^{n_{LHS}} (R_i - \mu_R)^2 \right]^{\frac{1}{2}} \tag{122}$$

The response R_i is the model run *i* with the random parameter vector (p_i). The LHS method requires specifying a distribution for each parameter. Because data are not available to formulate a distribution, a functional form is assumed. As a first estimate, a truncated normal distribution for each parameter is assumed with a mean and standard deviation shown in Table 26. Similar to the mean value method implementation (presented in Chapter 3), the mean is assumed to be a value of 1 that is multiplied by the nominal parameter values (i.e., thermal conductivity, $k(T) = p_i k_{nom}(T)$). The number of LHS samples was selected at a value of 420.

When a LHS approach is used, correlation coefficients can be directly calculated provided that $n_{LHS} \geq n_p$. The correlation coefficients are computed using the following equation:

$$r = \frac{\sum_{i}^{n_{LHS}} (p_i - \bar{p})(R_i - \bar{R})}{n_{LHS} \sigma_R \sigma_p} \tag{123}$$

where n_{LHS} is the number of samples, R_i is the value of the response of interest for the *i*th simulation, $\bar{R}$ is the mean value of the response, p_i is the value for the *i*th parameter, $\bar{p}$ is the mean value of the input parameter, σ_R is the standard deviation of the mean value of the response, and σ_p is the standard deviation of the mean value of the parameter. This approach assumes a linear correlation between the response and the parameter and is also referred to as the Pearson correlation coefficient.

The Pearson correlation coefficient will be 0 if there is no correlation between the parameter and the response. It will be positive if as the parameter value increases, so does the response value. It will be negative if the opposite is true. A value of 1 or -1 indicates a perfect fit.

Table 26: Input parameters used in LHS method.

Input parameter	σ_i	Input parameter	σ_i
BCs		*Reactions*	
Convection	0.10	Heat of Reaction 1	± 1000
Lid Temperature	0.02	Heat of Reaction 2	± 1000
		Heat of Reaction 3	± 1000
Foam		Activation Energy 1	0.02
Bulk Density	0.05	Activation Energy 2	0.02
Solid Density	0.10	Activation Energy 3	0.02
β_R	0.10	Mass Fraction Foam A	0.10
Bulk Conductivity	0.10	Mass Fraction Foam B	0.10
Specific Heat Capacity	0.10	Mass Fraction CO_2	0.10
Permeability	0.10	Mass Fraction HMWO	0.10
Molecular Weight	0.10		
		Gas Products	
Liquid		Specific Heat Capacity	0.10
Bulk Density	0.10	Mass Diffusivity	0.10
Solid Density	0.10	Viscosity	0.10
β_R	0.10	Molecular Weight LMWO	0.10
Bulk Conductivity	0.10	Molecular Weight HMWO	0.10
Specific Heat Capacity	0.10		
Permeability	0.10	*Steel*	
LMWO Saturation Pressure	0.10	Density	0.10
HMWO Saturation Pressure	0.10	Thermal Conductivity	0.10
		Specific Heat	0.10
Char		Emissivity	0.10
Bulk Density	0.10		
Solid Density	0.10		
β_R	0.10		
Bulk Conductivity	0.10		
Specific Heat Capacity	0.10		
Permeability	0.10		

5.3.3.2. Parameters with Special Considerations

While most of the parameters where varied by 10%, some required special consideration. From previous studies, it was known that the lid temperature and the virgin foam bulk density would dominate the results if varied the same as the other parameters. Since there are both well know, their range was reduced. The activation energy had to also be specially considered due to it being in the exponential. Its range was determined by looking at the spread in the TGA data. The nominal heat of reaction for all three reactions is zero, and thus using a multiplier would be futile. A range of ± 1000 was used, based on the range of literature data.

The saturation pressure was altered by changing the constants in the Antione equation (Eq 124).

$$P_{sat} = 10^{\left(A-\frac{B}{T+C}\right)} \tag{124}$$

It was decided to shift the saturation pressure up and down. Rewriting Eq 124 using logarithm properties yields 125.

$$P_{sat} = \frac{10^{A}}{10^{B/(T+C)}} \tag{125}$$

Since adjusting the saturation pressure by adjusting A is desired, a new variable *y* is introduced.

$$P_{sat2} = \frac{10^{Ay}}{10^{B/(T+C)}} \tag{126}$$

The ratio of the two saturation pressures is *x*, or the amount we want to vary the pressure by (in our case, *x* will range from 0.9 to 1.1).

$$\frac{P_{sat2}}{P_{sat}} = x = \frac{10^{Ay}}{10^{A}} = 10^{A(y-1)} \tag{127}$$

Rearranging, *y* can now be solved for.

$$\log_{10} x = A(y-1) \rightarrow \frac{\log_{10} x}{A} + 1 = y \tag{128}$$

Like the saturation pressure, determining the stoichiometry needed to be more carefully thought through. The original set of reactions is shown in equation set 129.

$$PMDI\ RPU = 0.45\ FOAMA + 0.15\ FOAMB + 0.4\ FOAMC$$

$$\begin{gathered} 0.45\ FOAMA \rightarrow 0.252\ CO_2 + 0.198\ LMWO \\ 0.15\ FOAMB \rightarrow 0.15\ HMWO \\ 0.4\ FOAMC \rightarrow 0.2\ HMWO + 0.2\ char \end{gathered} \tag{129}$$

Generalizing the stochiometric coefficients, it can be rewritten as:

$$\begin{gathered} aFOAMA \rightarrow \mathrm{v}\ CO_2 + \mathrm{w}\ LMWO \\ bFOAMB \rightarrow \mathrm{x}\ HMWO \\ cFOAMC \rightarrow \mathrm{y}\ HMWO + \mathrm{z}\ char \end{gathered} \tag{130}$$

Or:

$$FOAMA \rightarrow \frac{\mathrm{v}}{\mathrm{a}}\ CO_2 + \frac{\mathrm{w}}{\mathrm{a}}\ LMWO$$
$$FOAMB\ \rightarrow \frac{\mathrm{x}}{\mathrm{b}}\ HMWO \qquad 131$$
$$FOAMC \rightarrow \frac{\mathrm{y}}{\mathrm{c}} HMWO + \frac{\mathrm{z}}{\mathrm{c}} char$$

The stochiometric coefficients cannot be altered without ensuring that the equations remain balanced. There are several relationships that must be respected. In order for the *FOAMA* equation to balance, the following must be true:

$$a = v + w\ \rightarrow w = a - v \qquad 132$$

Likewise, for the *FOAMB* equation:

$$b = x \qquad 133$$

And for *FOAMC*:

$$c = y + z\ \rightarrow z = c - y \qquad 134$$

Finally, *FOAMA*, *FOAMB,* and *FOAMC* all must sum to one.

$$a + b + c = 1\ \rightarrow c\ = 1 - a - b \qquad 135$$

The result of this is that *FOAMA*, *FOAMB*, CO_2 and *HMWO* (in the *FOAMC* equation) will be varied, and *LMWO*, *HMWO* (in the *FOAMB* equation), and *char* will be driven to conserve mass.

5.3.3.3. Comparison of Model with Experiment

Once the ensemble of simulations was completed, the uncertainty in the temperature and pressure results could be quantified. There are two ways to look at this uncertainty, either by the standard deviation of the ensemble or by the maximum and minimum. The results are presented both ways, in Figure 76 through Figure 79. Figure 76 shows the pressure for both inverted and upright with uncertainty and compared to the experimental results. The inverted pressure, while not within the bounds of the first standard deviation, is within the min-max bounds. Upright is not in as close of agreement, however the minimum does at some points scrape the experimental bounds. While not quantitatively the same, qualitatively the agreement is good, and if the mechanism that determines with the upright breaks off from the inverted could be identified and shifted down 2 MPa, the quantitative agreement could be quite good.

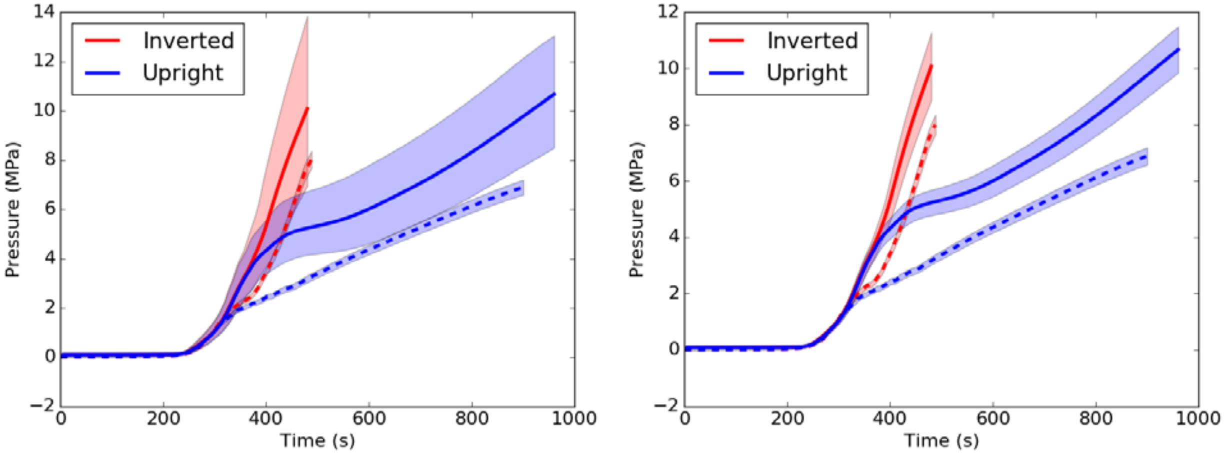

(a) (b)

Figure 76: Simulation results (solid) with experimental values (dashed) for upright (blue) and inverted (red) for the 150 °C/min heating rate for pressure with (a) the simulation error field representing the range of the simulations and (b) the simulation error field representing the first standard deviation of the simulations.

Figure 77 shows the results for TC25. The results here are very good: the inverted experimental results are within a standard deviation of the simulations; the upright experimental results are within the min-max, and very close to being within a standard deviation. These results are significantly better than what was seen with Porous Media only. One possible reason for this is that the liquid phase was given similar properties to the virgin phase, rather than the char. In the results shown in Chapter 4, the excess gases where sent to the char phase.

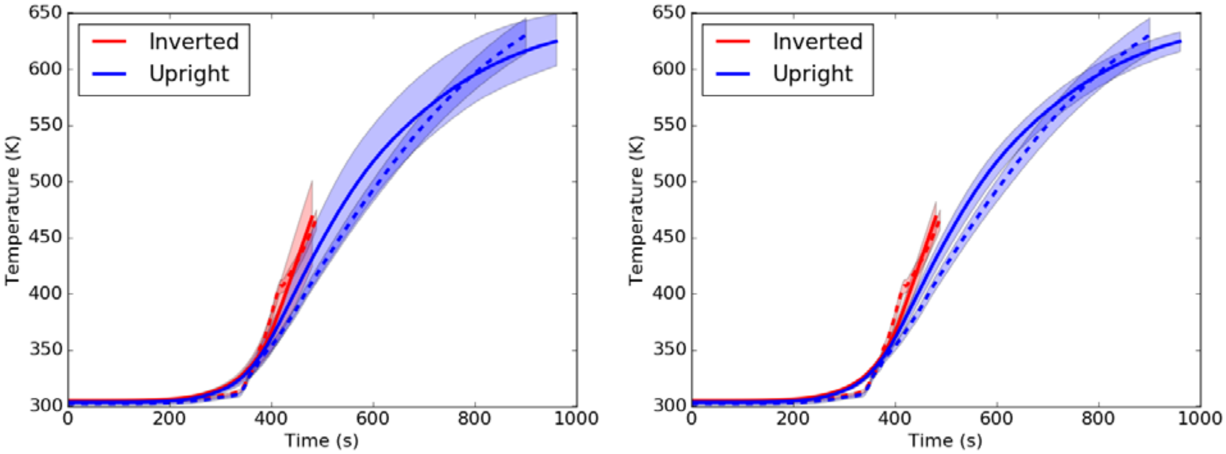

(a) (b)

Figure 77: Simulation results (solid) with experimental values (dashed) for upright (blue) and inverted (red) for the 150 °C/min heating rate for TC25 with (a) the simulation error field representing the range of the simulations and (b) the simulation error field representing the first standard deviation of the simulations.

Figure 78 and Figure 79 show the side thermocouples. The agreement here is similar to what has been seen in the previous models: prediction is better further from the heat source, which could be an outcome of not accurately modeling the weld or having a constant convective heat transfer coefficient.

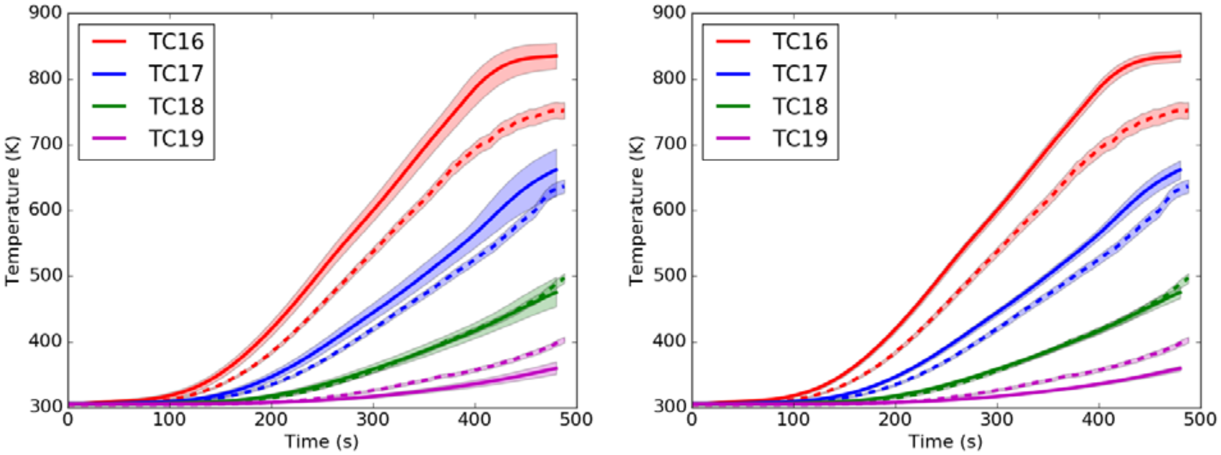

(a) (b)

Figure 78: Simulation results (solid) with experimental values (dashed) for the inverted orientation and the 150 °C/min heating rate for the thermocouples along the sides of the can with (a) the simulation error field representing the range of the simulations and (b) the simulation error field representing the first standard deviation of the simulations.

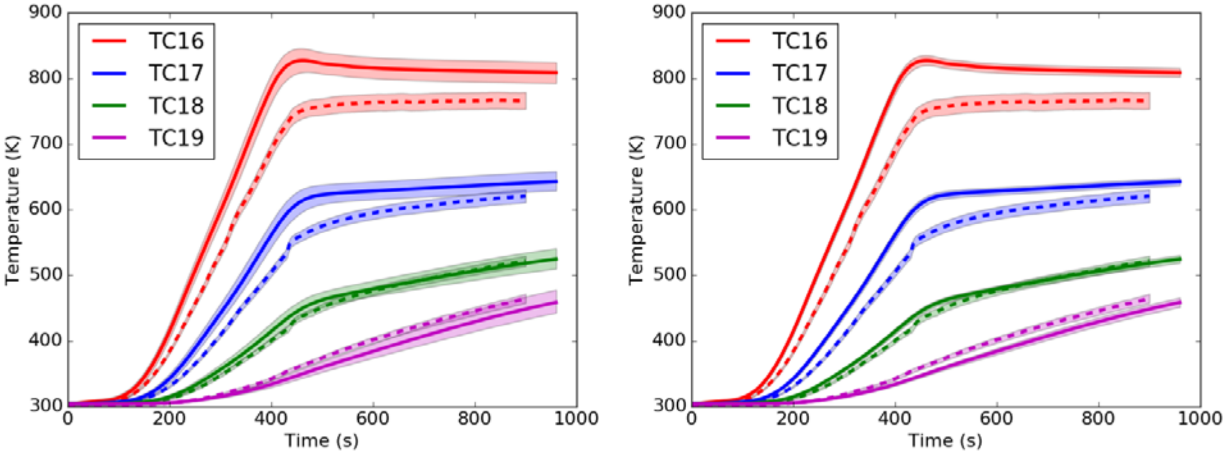

(a) (b)

Figure 79: Simulation results (solid) with experimental values (dashed) for the upright orientation and the 150 °C/min heating rate for the thermocouples along the sides of the can with (a) the simulation error field representing the range of the simulations and (b) the simulation error field representing the first standard deviation of the simulations.

5.3.3.4. Sensitivities

With 42 parameters, all of which had sensitivity information over the time, it was necessary to determine a way to make the information more digestible. To do this, the Pearson correlation (r) were integrated over time, and weighted by the response (R_i) at that time (so that early time variation before physics begin at a certain location are not over represented) as shown in equation 136. The results are shown in Figure 80.

$$\int_0^t |r(t)| * \frac{R_i(t)-R_i(t_0)}{R_{i\,max}}\, dt \tag{136}$$

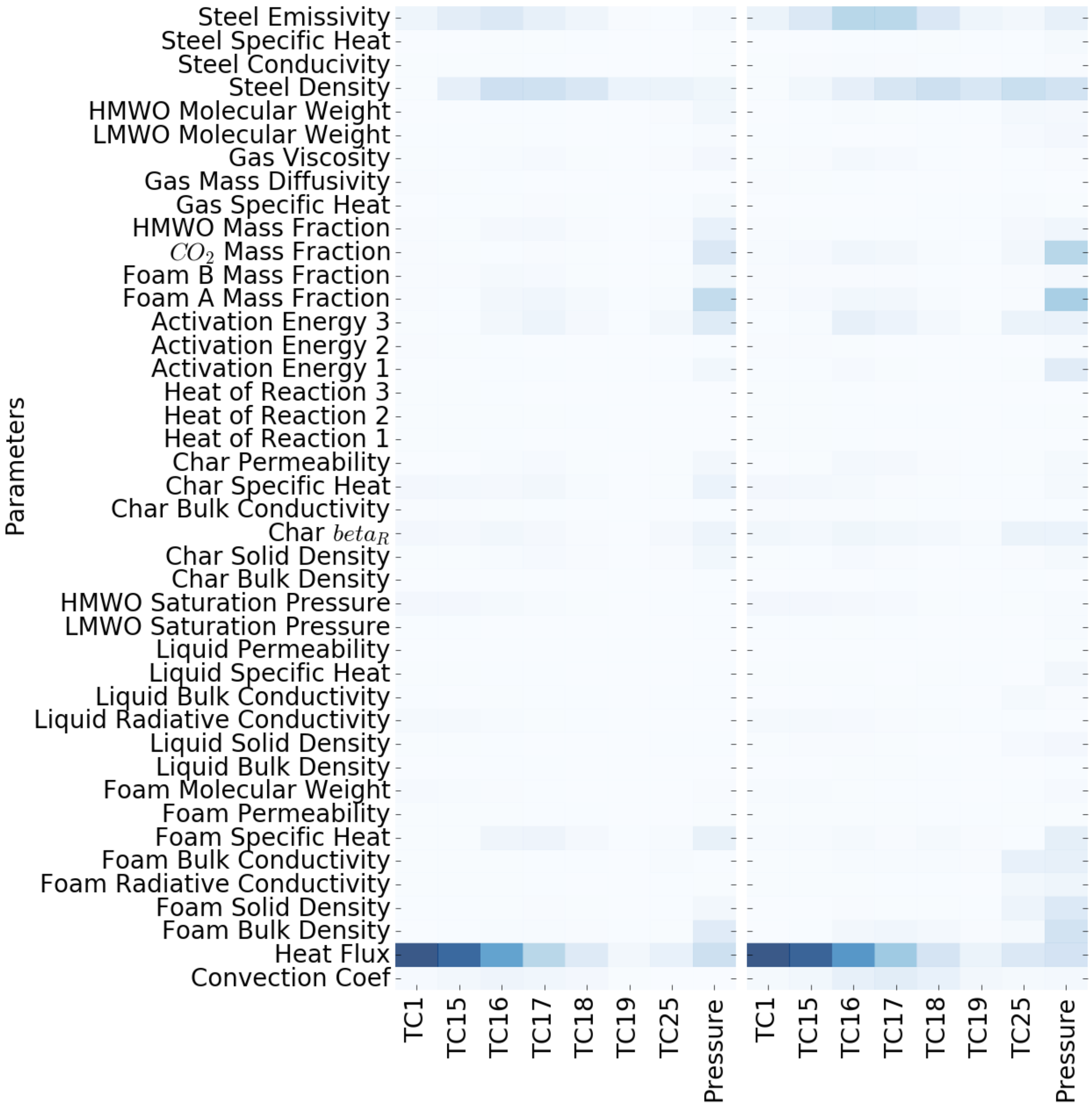

Inverted Upright

Figure 80: Heat maps that correlates each parameter with each response for the inverted (left) and upright (right) simulation. A darker color indicates that the response is more sensitive to the parameter.

Unsurprisingly, the heat flux boundary condition on the heated plate overwhelms the sensitivity of the thermocouples near it, so much so, that is washes out most of the information on the map. Thus, a second map, Figure 81, shows the same data, but with ‘heat flux’ removed.

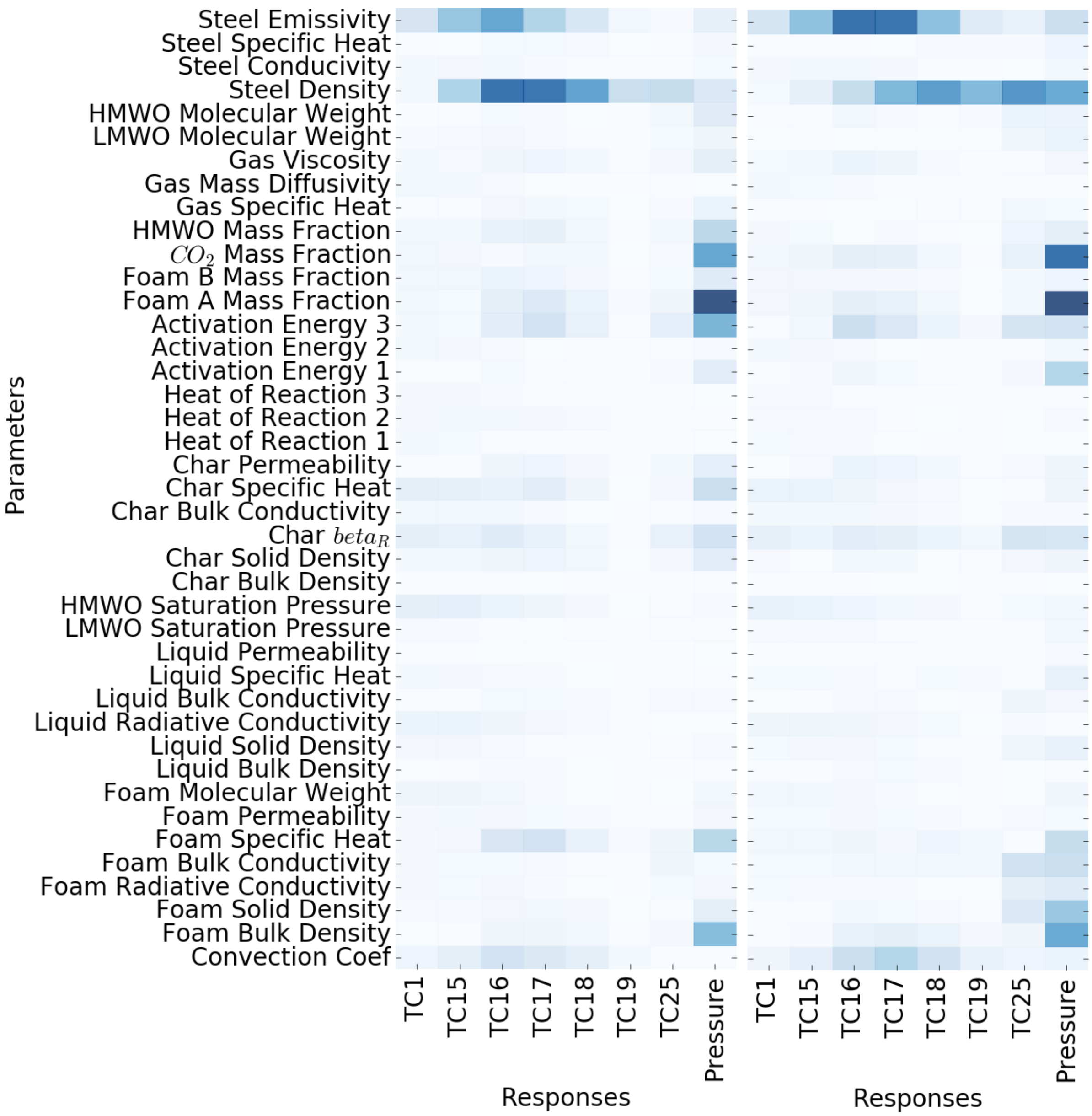

Inverted Upright

Figure 81: Heat maps that correlates each parameter with each response for the inverted (left) and upright (right) simulation. A darker color indicates that the response is more sensitive to the parameter. In this map, 'Heat Flux' was removed at a parameter in order to be able to view the effects of the other parameters.

This map shows several interesting interactions between the parameters and the responses. First, there is a difference between the inverted and upright responses. For example, steel density is not as important for TC25 in the inverted as it is in the upright. This is most likely due to more heat reaching the slug through alternative heat paths. In addition, the slug temperature is typically ~150K hotter at the end of the upright case, due to the increased time at temperature. This map also shows that TC 25 is not nearly as sensitive to the parameters as pressure and some of the other thermocouples, particularly in the inverted case. In the upright, some of the foam properties begin to increase in importance. Pressure appears to be the most sensitive to the widest range of parameters, from steel properties, to the reactions, and the foam's properties. The thermocouples along the side of the can tend to be most sensitive to the properties of steel, though they do also show a reaction to some of the foam properties (specific heat, for example) and the reactions.

While the heat maps provide a useful overview, viewing the time histories of the sensitivities for each response is also useful. Figure 82 through Figure 88 show the top five parameters, ranked using equation 136 for each of the thermocouples shown in the heat map. The legend for each figure is presented in terms of this ranking – in other words, the first parameter in the legend is the most important and the last the 5th most important. The styles of the lines are grouped by the property of the parameter: dotted lines are a boundary condition, dot-dash are a steel property, dash are a reaction property, and solid are a foam property. Each parameter has a unique line and style, for example, the heat flux on the lid of the can is always blue dots. As a reminder, the Pearson coefficient is 0 when there is no correlation between parameter and response, 1 when there is a perfect correlation (when parameter goes up, response goes up), and -1 when there is a perfect inverse correlation (when parameter goes up, response goes down).

Figure 82 shows TC1, and as should not be a surprise, the heat flux dominates at nearly 1 the entire simulation. The other parameters hover near zero, though they do change their exact order depending on if the simulation is upright or inverted. Probably most interesting is that the char radiative conductivity starts to become more important around 400 seconds (in both simulations), and since this parameter remains more important after that time, it jumps from 5th to 3rd between inverted and upright. This is a feature between upright and inverted will be seen in all the responses.

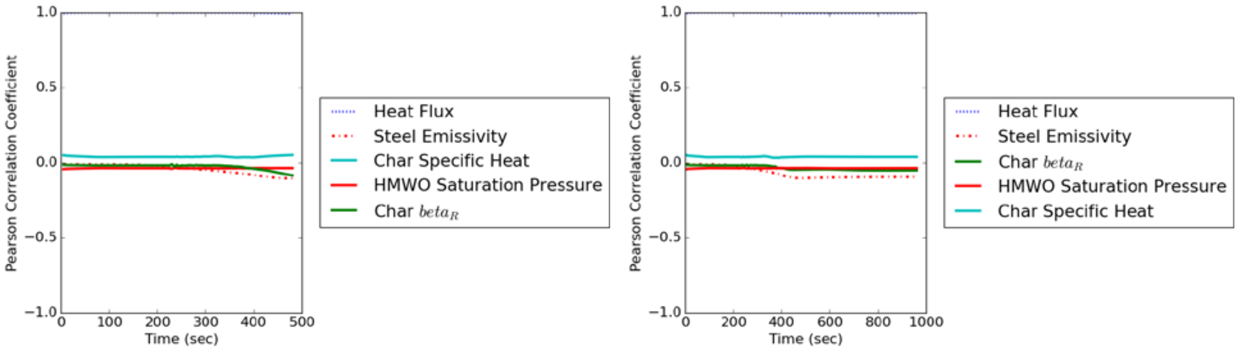

(a) (b)

Figure 82: Top five sensitive parameters for TC1 for (a) inverted and (b) upright.

Figure 83 shows TC 16. While the heat flux still dominates this thermocouple, the other parameters play a much larger role. One interesting difference between inverted and upright here is the importance of steel emissivity vs density. This is also seen in TC 17 Figure 84. At 250 seconds, density begins to become less important, leveling at around 500 seconds. This is the same time at which the temperatures level out – and the problem (at this thermocouple) has become similar to steady state. Thus, it is not surprising that the time dependent properties would tend towards zero at this point. However, the emissivity will be part of the radiation equations, will only increase with temperature. One can see the leveling out of this property as well.

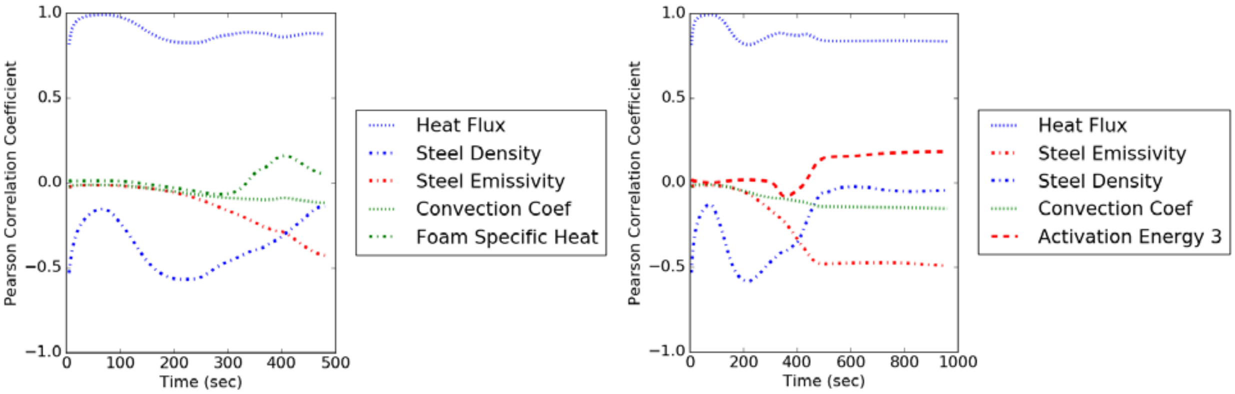

(a) (b)

Figure 83: Top five sensitive parameters for TC16 for (a) inverted and (b) upright.

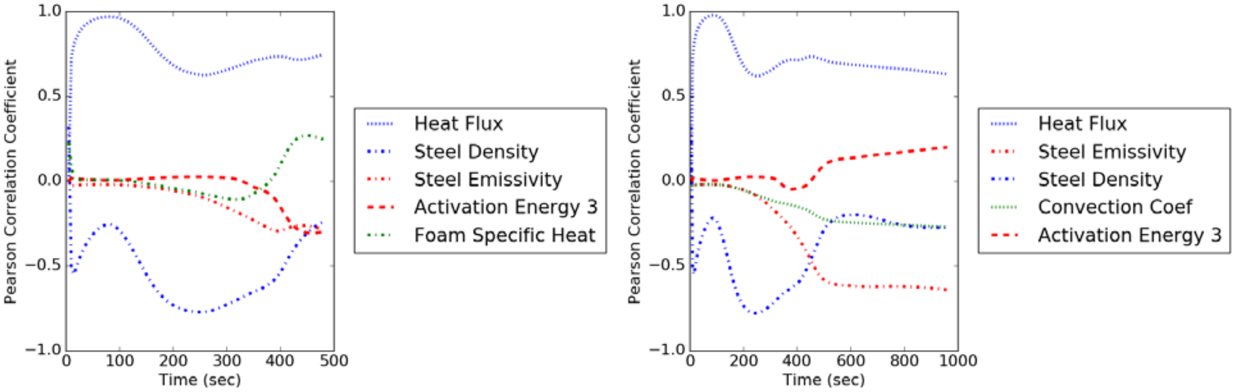

(a) (b)

Figure 84: Top five sensitive parameters for TC17 for (a) inverted and (b) upright.

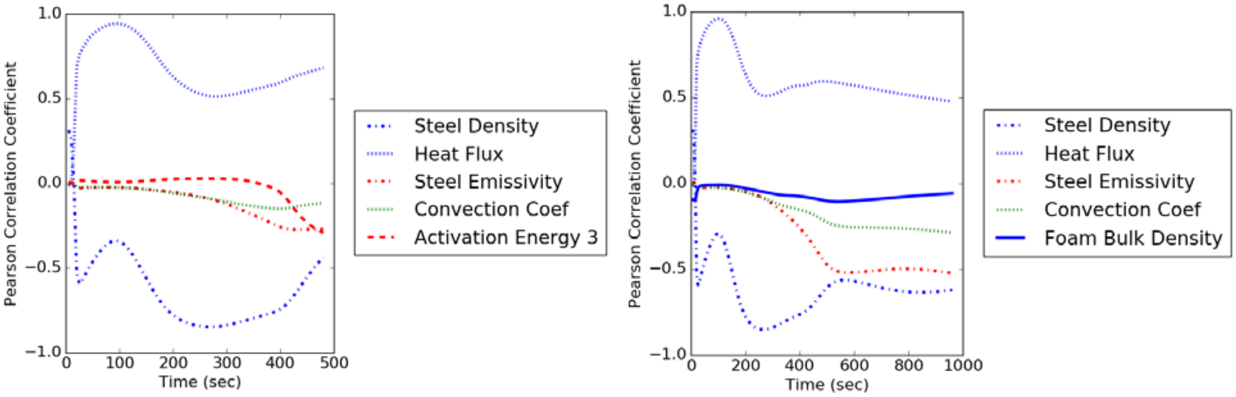

(a) (b)

Figure 85: Top five sensitive parameters for TC18 for (a) inverted and (b) upright.

Figure 85 and Figure 86 show TC 18 and 19, respectively. In these, heat flux loses the first position of importance to the density of the steel. In general, the properties that are not one of these two are becoming less important, the most extreme case being TC 19 in the inverted orientation.

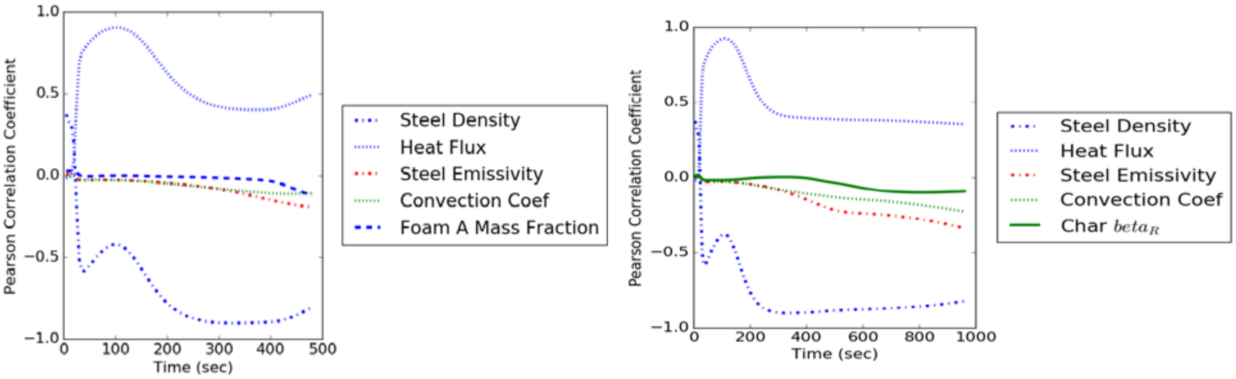

(a) (b)

Figure 86: Top five sensitive parameters for TC19 for (a) inverted and (b) upright.

Figure 87 shows the results for TC 25. Heat flux and steel density still dominate, however, now more of the foam properties and reaction mechanisms are in play. As the most direct heat path for TC 25 is through the foam, it makes sense that this would be true. That TC 25 is sensitive to the activation energy in the third reaction (*FOAMC*) makes sense, as this is the reaction that controls the production of char. This is also the material through which heat will travel later in time. There is also an interesting behavior with the foam activation energy in the third reaction in the upright case: the sign of the Pearson coefficient changes. This mean that for part of the simulation increasing the activation energy decreased the temperature, and later in time it increased the temperature.

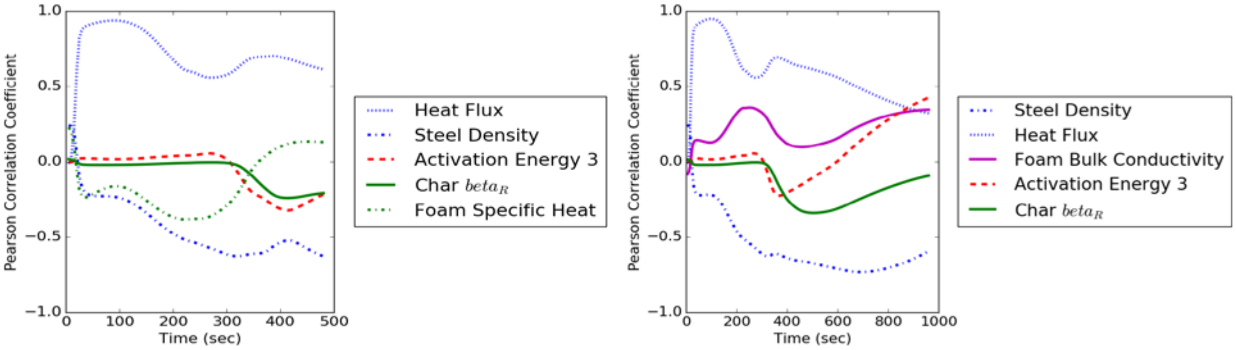

(a) (b)

Figure 87: Top five sensitive parameters for TC25 for (a) inverted and (b) upright.

Figure 88 show the sensitivities in pressure. The *FOAMA* mass fraction ('a' equation set 129) is now the most important. This is reasonable, as that is the reaction that controls the CO_2 (also seen to be important). What is interesting is that when *FOAMA* goes up, the pressure goes down. This is because of how the equations are constrained to conserve mass. Since *LWMO* is driven by the combination of *FOAMA* and CO_2, (equation 132), when *FOAMA* is increased without also increasing CO_2, *LWMO* is increased, which in turn decreases the pressure.

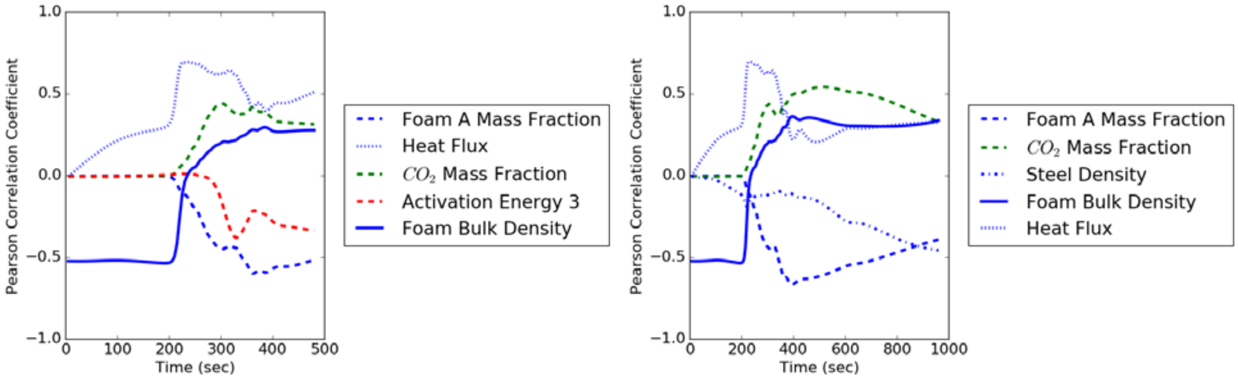

(a) (b)

Figure 88: Top five sensitive parameters for Pressure for (a) inverted and (b) upright.

These results highlight how sensitive the pressure is to the reactions. The reactions are known to be pressure dependent, as seen in the difference between the unconfined and partially confined TGA results. Therefore, at these pressures, how much confidence is there in the reactions? These results would indicate that time spent investigating this problem would be of high value.

5.4. 3D Foam in a Can Model

Figure 89 and Figure 90 show the results for the Porous Media with VLE model in 3D. The mesh that was used to run these simulations was the same one used in Chapter 4. The results match better in pressure than the previously reported 2D results, but they do not match well in temperature for TC 25. However, they are in better agreement than the Porous Media results presented in Chapter 4. The side thermocouples show similar agreement to the results in the prior sections.

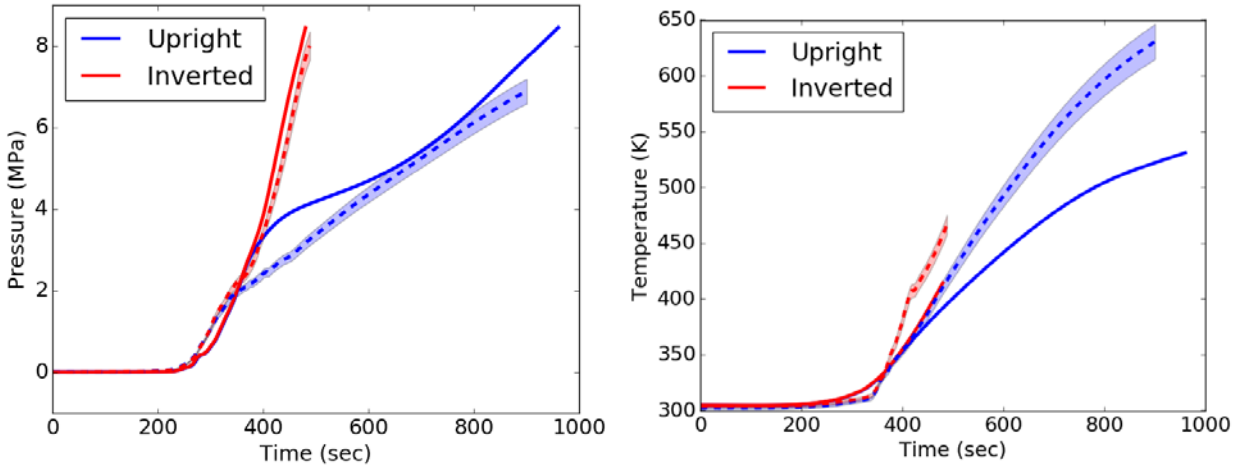

(a) (b)

Figure 89: Simulation results (solid) with experimental values (dashed) for upright (blue) and inverted (red) for the 150 °C/min heating rate for (a) pressure and (b) temperature of the embedded object (TC 25). These results are for the 3D mesh used in the Porous Media only study.

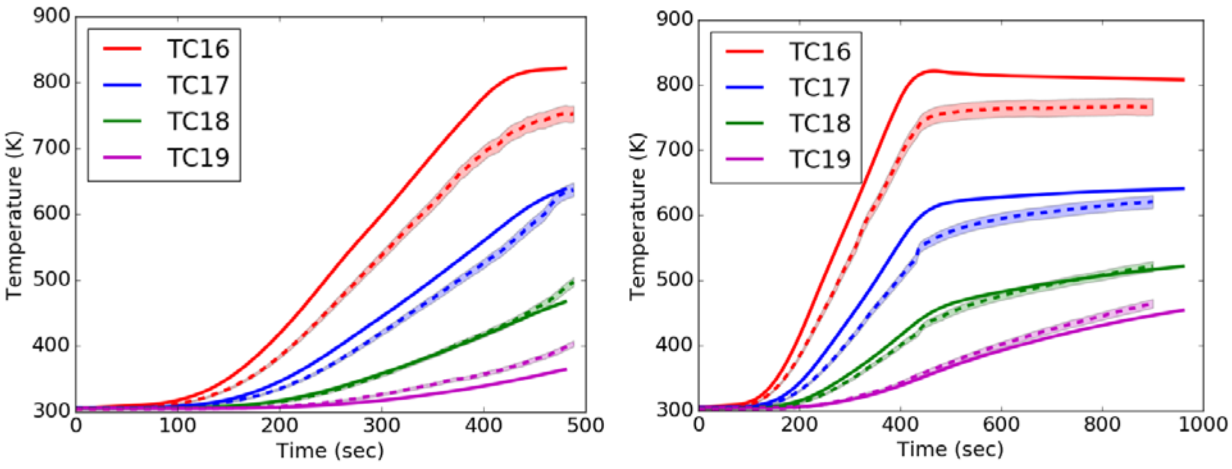

(a) (b)

Figure 90: Simulation results (solid) with experimental values (dashed) for the 150 °C/min heating rate for (a) inverted and (b) upright. These results are for the 3D mesh used in the Porous Media only study.

The stark difference between the 2D and 3D results were puzzling until the mesh resolution study was recalled. Figure 91 shows the 2D results for the course mesh – the one that was created to match the 3D mesh that was used in the Porous Media simulations. These results are similar to those seen in Figure 89. While the 3D mesh was converged for the Porous Media simulations, it appears that when the VLE is added, the mesh needs to be further refined. The similarities between Figure 89 and Figure 91 create the possibility that computationally expensive activities, such as mesh resolution, calibration, sensitivity, and uncertainty quantification can be done on a 2D mesh and extrapolated to 3D.

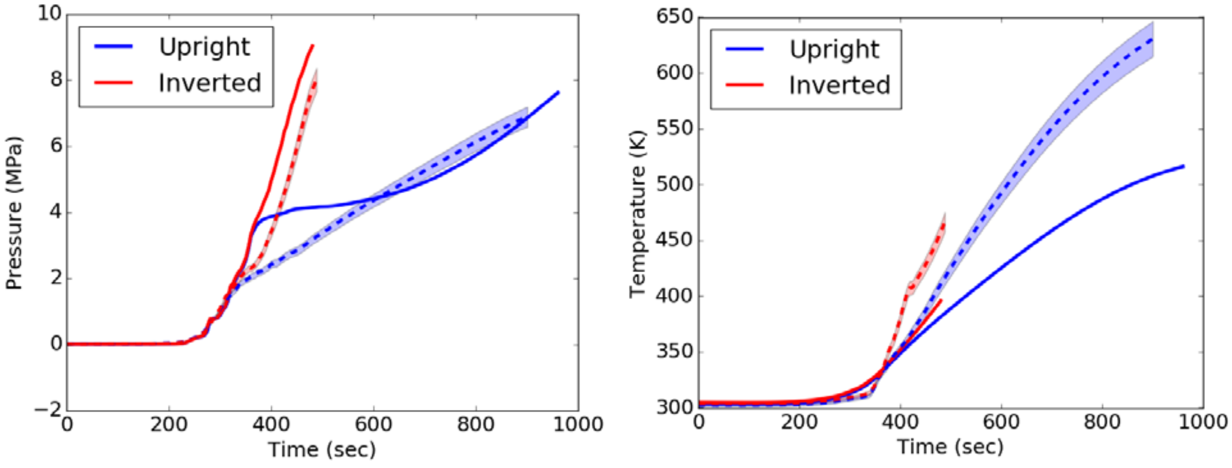

(a) (b)

Figure 91: Simulation results (solid) with experimental values (dashed) for upright (blue) and inverted (red) for the 150 °C/min heating rate for (a) pressure and (b) temperature of the embedded object (TC 25). These results are for the 2D coarse mesh.

5.5. Remarks

The addition of the VLE equation to the Porous Media model improved the predictivity of the simulations, while at the same time replacing an unknown, calibrated parameter (organic condensed fraction). Drastic improvements were seen in temperature agreement, and qualitatively the upright pressure prediction was improved. Being able to create the liquid phase is a big step towards the multiphysics model that is needed to model this complex problem.

However, improvement does come with a cost. The addition of the VLE equations does require a more refined mesh for solution convergence. That resolution study, as well as other activities in 3D is left to future work.

Also left to future work are additional calibrations of unknown parameters, such as the permeabilities. Further understanding of how the reactions change with pressure is also essential to accurate prediction. In addition, the properties of the liquid must also be addressed, as currently it is given the same material properties as the virgin foam, since there is currently little experimental data on the properties of the liquid. Further experiments are needed to fully characterize the liquid phase.

This work also highlights some of the difficulty in quantifying uncertainty. In this case, most of the parameters were given a 10% uncertainty, however that may not be representative of how well the parameters are known. However, increasing the input uncertainty increases the output uncertainty, and thus doing this blindly will only obscure results. There is also the issue of how to deal with parameters that vary in complicated ways, such as the saturation pressure or stoichiometry. More advanced UQ techniques could lead to better results.

6. CONCLUSION

The goal of the work was to create a model that could predict temperature and pressure in a sealed can filled with PMDI polyurethane foam. Three models have been presented to this end – each one to varying degrees of accuracy: No Flow, Porous Media, and Porous Media with VLE. Below is an outline of the highlights of each model.

6.1. 6.1 Comparison of the models

No Flow Model

- Temperature and Pressure Calculation
  - Temperature is solved for by the heat equation
  - Pressurization calculated using ideal gas law
    - There is no advection of gases
- Reaction Mechanism
  - A three-step reaction mechanism decomposes PMDI polyurethane into CO_2, light molecular weight organics (LMWO), heavy molecular weight organics (HMWO), and char.
    - CO_2, LMWO, and HMWO are all in the gas phase, and char is in the solid phase
      - There are no liquids present
- Material Properties
  - Foam effective conductivity and foam porosity are a function of reaction
  - Other material properties are constant or function of temperature

Porous Media Model

- Temperature and Pressure Calculation
  - Continuity, species, and enthalpy equations are solved for in condensed and gas phases
  - Gas velocity is solved using Darcy's approximation for flow through a porous material
  - The ideal gas law is used to relate density to pressure
- Three step reaction mechanism
  - A three-step reaction mechanism decomposes PMDI polyurethane into CO_2, light molecular weight organics (LMWO), heavy molecular weight organics (HMWO), and char.
    - CO_2, LMWO, and HMWO are all in the gas phase, and char is in the solid phase.
      - There are no liquids present
- Material Properties

    - Foam effective conductivity, foam porosity, and foam permeability are a function of reaction
    - All other material properties are constant or function of temperature

Porous Media with VLE

- Temperature and Pressure Calculation
    - Continuity, species, and enthalpy equations are solved for in condensed and gas phases
    - Gas velocity is solved using Darcy's approximation for flow through a porous material
    - The ideal gas law used to relate density to pressure
- Three step reaction mechanism
    - A three-step reaction mechanism decomposes PMDI polyurethane into CO_2, light molecular weight organics (LMWO), heavy molecular weight organics (HMWO), and char.
        - CO_2, is in the gas phase and char is in the solid phase.
        - Phase of light and heavy organics determined by Henry's or Raoult's law, and can be either gas or liquid
- Material Properties
    - Foam effective conductivity, foam porosity, and foam permeability are a function of reaction
    - All other material properties are constant or function of temperature

Each of the models have their strengths and weaknesses. Figure 92 presents a side by side comparison of the three models. The No Flow model lacks the ability to predict orientation, however it runs quickly and can predict temperature well. In cases where the using the physics based models is computationally infeasible, the No Flow model is a good option.

The Porous Media model can differentiate between the two orientations. However, to achieve this, several parameters had to be calibrated, as there was no way to measure them. In addition, the reaction mechanism was calibrated into order to achieve the results presented (organic liquid fraction). While these calibrations seem to hold at other heating rates, it is not clear if it is geometry independent – further testing is needed. In addition, the Porous Media model requires a more refined grid and takes significantly more computational resources to run. And while pressure agrees well, the temperature of the slug is under predicted. Possible causes for this under prediction will be discussed in the next section.

The Porous Media with VLE model includes not the physics for gas advection, it also predicts the vapor/liquid split in the decomposition products. This addition removed one of the calibrated parameters (organic liquid fraction). The results compare well in both temperature and pressure. However, the Porous Media with VLE model requires a yet again refined mesh, which will make it even more computationally expensive to run. Also, the liquid phase does not as of yet advect, however, its creation is the first step to a multiphase model that includes liquid flow.

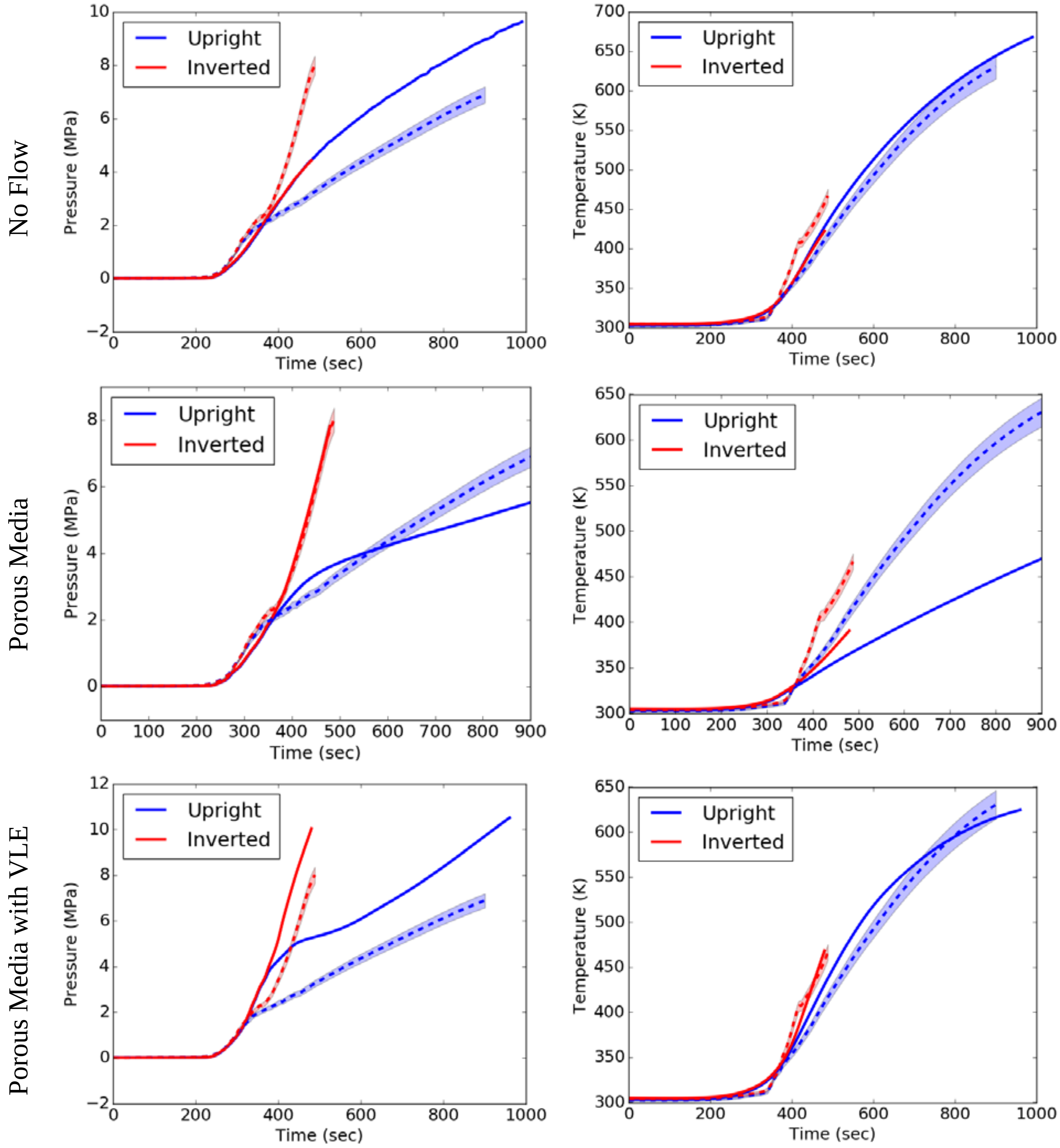

(a) (b)

Figure 92: A comparison of the three models. Simulation results (solid) with experimental values (dashed) for upright (blue) and inverted (red) for the 150 °C/min heating rate for (a) pressure and (b) temperature of the embedded object (TC 25).

6.2. 6.2 Future Work

The end goal of the project is to create a full multiphase flow model. As seen in Table 27, there has been incremental progress to this goal, but it is not yet achieved. However, while future work is directed towards the multiphase flow objective, there is still work to be done on the other models.

Table 27: Progression of the model over time

	No Flow	Porous Media	Multiphase Flow
Temperature	✓	✓	✓
Pressure	✓	✓	✓
Gas Flow		✓	✓
Liquid Flow			✓

For all the models, there is still the open question on the best way to model radiation. The radiative effective conductivity is only applicable for optically thick materials – so if a structured char is not left behind, then using the method is a poor assumption. Other radiation models should be explored, including radiation enclosures that are a function of reaction and participating media models.

When exploring the Porous Media with VLE model, it was discovered that if the liquid phase properties were set to be the same as the virgin foam, the agreement between experiment and simulation was much better. This calls into question sending the excess ‘organic liquid fraction’ materials to the char phase in the Porous Media model. This may be contributing to the poor agreement in temperature. Creating a faux liquid phase and examining its material properties would be prudent. If there is a large difference, re-calibration may be in order.

Additional heating rates should be examined for the Porous Media with VLE model, as well as a new calibration of the permeabilities and Rosseland mean extinction coefficient for the char, to see if they differ from those found in the Porous Media calibration.

Test UQ, mesh, and calibration studies should be run in 2D and 3D to see if the results coincide. Considering the computational resources needed to run the more complicated models, anything that can lessen the burden will be of great importance.

Both the Porous Media and Porous Media model with VLE need to be tested in a range of heating rates and geometries to confirm predictiveness. Additional experiments will be needed to validate these new heating rates and geometries.

Finally, now that a liquid phase can be generated, the ability to advect that liquid needs to be implemented into the code. This functionality will need to undergo rigorous testing of the sort presented in this work for the other models. Experiments will be needed to better understand the liquid’s properties, in order to accurately model it. And additional validation experiments will also be needed.

REFERENCES

[1] C. Beyler and M. Hirschler, “Thermal Decomposition of Polymers,” in *SFPE Handbook of Fire Protection Engineering*, National Fire Protection Association, 2001, pp. 110–131.

[2] K. L. Erickson and J. Oelfke, “Effect of Ambient Oxygen Concentration on Thermal Decomposition of Polyurethanes Based on MDI and PMDI,” ACS Publications, 2009.

[3] K. L. Erickson, A. B. Dodd, R. E. Hogan, and K. J. Dowding, “Heat Transfer, Foam Decomposition, and Container Pressurization: Comparison of Experimental and Modeling Results,” presented at the Interflam, Nottingham, UK, 2010.

[4] K. L. Erickson, A. B. Dodd, and E. C. Quintana, “Physical Behavior and Container Pressurization During Thermal Decomposition of Polyurethane Foams,” in *Proceedings of BCC 2011*, Stamford, 2011.

[5] K. L. Erickson, A. B. Dodd, and R. E. Hogan, “Modeling Pressurization Caused by Thermal Decomposition of Highly Charring Foam in Sealed Containers,” in *Proceedings of BCC 2010*, Stamford, CT, 2010.

[6] World Health Orgnaization, “4,4′-Methylenediphenyl Diisocyanate And Polymeric 4,4′-Methylenediphenyl Diisocyanate,” *IARC Monographs on the Evaluation of Carcinogenic Risks to Humans*, vol. 71, pp. 1049–1058.

[7] K. L. Erickson, “Thermal decomposition mechanisms common to polyurethane, epoxy, poly (diallyl phthalate), polycarbonate and poly (phenylene sulfide),” *Journal of Thermal Analysis and Calorimetry*, vol. 89, no. 2, pp. 427–440, 2007.

[8] M. B. Nemer, C. F. Brooks, B. Shelden, M. M. Soehnel, and D. A. Barringer, “Rheological and Mechanical Property Measurements of PMDI Foam at Elevated Temperatures,” Sandia National Lab.(SNL-NM), Albuquerque, NM (United States), 2014.

[9] R. Hadden, A. Alkatib, G. Rein, and J. L. Torero, “Radiant Ignition of Polyurethane Foam: The Effect of Sample Size,” *Fire Technology*, vol. 50, no. 3, pp. 673–691, May 2014.

[10] T. Rogaume *et al.*, “Development of the Thermal Decomposition Mechanism of Polyether Polyurethane Foam Using Both Condensed and Gas-Phase Release Data,” *Combustion Science and Technology*, vol. 183, no. 7, pp. 627–644, Apr. 2011.

[11] L. Bustamante Valencia, T. Rogaume, E. Guillaume, G. Rein, and J. L. Torero, “Analysis of principal gas products during combustion of polyether polyurethane foam at different irradiance levels,” *Fire Safety Journal*, vol. 44, no. 7, pp. 933–940, Oct. 2009.

[12] C. D. Blasi, “Analysis of Convection and Secondary Reaction Effects Within Porous Solid Fuels Undergoing Pyrolysis,” *Combustion Science and Technology*, vol. 90, no. 5, pp. 315–340, Apr. 1993.

[13] I. Vermesi, N. Roenner, P. Pironi, R. M. Hadden, and G. Rein, “Pyrolysis and ignition of a polymer by transient irradiation,” *Combustion and Flame*, vol. 163, pp. 31–41, Jan. 2016.

[14] O. M. Putzeys, A. C. Fernandez-Pello, G. Rein, and D. L. Urban, “The piloted transition to flaming in smoldering fire retarded and non-fire retarded polyurethane foam,” *Fire and Materials*, vol. 32, no. 8, pp. 485–499, Dec. 2008.

[15] C. Lautenberger and C. Fernandez-Pello, “Generalized pyrolysis model for combustible solids,” *Fire Safety Journal*, vol. 44, no. 6, pp. 819–839, Aug. 2009.

[16] Sierra Core Team, *Sierra Thermal Fluids Code*. Albuquerque, NM: Sandia National Laboratories, 2017.

[17] A. R. Khoei and T. Mohammadnejad, “Numerical modeling of multiphase fluid flow in deforming porous media: a comparison between two-and three-phase models for seismic

analysis of earth and rockfill dams," *Computers and Geotechnics*, vol. 38, no. 2, pp. 142–166, 2011.

[18] D. K. Todd, *Ground water hydrology*. John Wiley and Sons, Inc, New York, 1959.

[19] K. Khanafer and K. Vafai, "The role of porous media in biomedical engineering as related to magnetic resonance imaging and drug delivery," *Heat and Mass Transfer*, vol. 42, no. 10, pp. 939–953, Aug. 2006.

[20] A. J. Barra and J. L. Ellzey, "Heat recirculation and heat transfer in porous burners," *Combustion and Flame*, vol. 137, no. 1–2, pp. 230–241, Apr. 2004.

[21] A. J. Barra, G. Diepvens, J. L. Ellzey, and M. R. Henneke, "Numerical study of the effects of material properties on flame stabilization in a porous burner," *Combustion and Flame*, vol. 134, no. 4, pp. 369–379, Sep. 2003.

[22] A. B. Dodd, C. Lautenberger, and A. C. Fernandez-Pello, "Numerical examination of two-dimensional smolder structure in polyurethane foam," *Proceedings of the Combustion Institute*, vol. 32, no. 2, pp. 2497–2504, 2009.

[23] A. B. Dodd, C. Lautenberger, and C. Fernandez-Pello, "Computational modeling of smolder combustion and spontaneous transition to flaming," *Combustion and Flame*, vol. 159, no. 1, pp. 448–461, Jan. 2012.

[24] J. E. J. Staggs, "Heat and mass transport in developing chars," *Polymer Degradation and Stability*, vol. 82, no. 2, pp. 297–307, Jan. 2003.

[25] C. Denecker, J. J. Liggat, and C. E. Snape, "Relationship between the thermal degradation chemistry and flammability of commercial flexible polyurethane foams," *Journal of Applied Polymer Science*, vol. 100, no. 4, pp. 3024–3033, May 2006.

[26] J. Zhang, T. J. Shields, and G. W. H. Silcock, "Effect of melting behaviour on flame spread of thermoplastics," *Fire and Materials*, vol. 21, no. 1, Dec. 1998.

[27] K. M. Butler, "A model of melting and dripping thermoplastic objects in fire," *Fire and materials*, pp. 341–352, 2009.

[28] K. M. Butler, E. Oñate, S. R. Idelsohn, and R. Rossi, "Modeling polymer melt flow using the particle finite element method," in *Eleventh International Interflam Conference, London, England*, 2007, pp. 929–940.

[29] E. Oñate, R. Rossi, S. R. Idelsohn, and K. M. Butler, "Melting and spread of polymers in fire with the particle finite element method," *International Journal for Numerical Methods in Engineering*, 2009.

[30] A. C.-T. Sun, *Foam Liquefaction Model under Abnormal Thermal Environment: A Multiphase, Coupled-physics, ALE Approach*. United States. Department of Energy, 2006.

[31] D. R. Noble, E. P. Newren, and J. B. Lechman, "A conformal decomposition finite element method for modeling stationary fluid interface problems," *International Journal for Numerical Methods in Fluids*, p. n/a-n/a, 2009.

[32] G. Rein, C. Lautenberger, A. Fernandez-Pello, J. Torero, and D. Urban, "Application of genetic algorithms and thermogravimetry to determine the kinetics of polyurethane foam in smoldering combustion," *Combustion and Flame*, vol. 146, no. 1–2, pp. 95–108, Jul. 2006.

[33] M. C. Bruns, J. H. Koo, and O. A. Ezekoye, "Population-based models of thermoplastic degradation: Using optimization to determine model parameters," *Polymer Degradation and Stability*, vol. 94, no. 6, pp. 1013–1022, Jun. 2009.

[34] S. Garcia, J. Guynn, and E. P. Scott, "Use of Genetic Algorithms In Thermal Property Estimation: Part Ii - Simultaneous Estimation Of Thermal Properties," *Numerical Heat Transfer, Part A: Applications*, vol. 33, no. 2, pp. 149–168, Feb. 1998.

[35] M. Chaos, M. M. Khan, N. Krishnamoorthy, J. L. de Ris, and S. B. Dorofeev, “Evaluation of optimization schemes and determination of solid fuel properties for CFD fire models using bench-scale pyrolysis tests,” *Proceedings of the Combustion Institute*, vol. 33, no. 2, pp. 2599–2606, Jan. 2011.

[36] K. J. Overholt and O. A. Ezekoye, “Quantitative testing of fire scenario hypotheses: a bayesian inference approach,” *Fire Technology*, vol. 51, no. 2, pp. 335–367, 2015.

[37] M. C. Bruns, “Inferring and Propagating Kinetic Parameter Uncertainty for Condensed Phase Burning Models,” *Fire Technology*, vol. 52, no. 1, pp. 93–120, Jan. 2016.

[38] S. I. Stoliarov, N. Safronava, and R. E. Lyon, “The effect of variation in polymer properties on the rate of burning,” *Fire and Materials*, vol. 33, no. 6, pp. 257–271, Oct. 2009.

[39] G. T. Linteris, “Numerical simulations of polymer pyrolysis rate: Effect of property variations,” *Fire and Materials*, vol. 35, no. 7, pp. 463–480, Nov. 2011.

[40] A. Matala and S. Hostikka, “Probabilistic simulations of cable fires in a cable tunnel,” in *20th international conference on structural mechanics in reactor technology, Helsinki, Finland*, 2009.

[41] P. T. Summers, B. Y. Lattimer, S. Case, and S. Feih, “Predicting compression failure of composite laminates in fire,” *Composites Part A: Applied Science and Manufacturing*, vol. 43, no. 5, pp. 773–782, May 2012.

[42] P. T. Summers, B. Y. Lattimer, S. Case, and S. Feih, “Sensitivity of thermo-structural model for composite laminates in fire,” *Composites Part A: Applied Science and Manufacturing*, vol. 43, no. 5, pp. 783–792, May 2012.

[43] N. Bal and G. Rein, “Relevant model complexity for non-charring polymer pyrolysis,” *Fire Safety Journal*, vol. 61, pp. 36–44, Oct. 2013.

[44] N. Bal and G. Rein, “On the effect of inverse modelling and compensation effects in computational pyrolysis for fire scenarios,” *Fire Safety Journal*, vol. 72, pp. 68–76, Feb. 2015.

[45] J. Suo-Anttila, A. B. Dodd, and D. Jernigan, “Thermal Mechanical Exclusion Region Barrier Breach Foam Experiments SAND2012-7600,” Sandia National Lab.(SNL-NM), Albuquerque, NM (United States), 2012.

[46] J. Suo-Anttila, J. Koenig, A. B. Dodd, and E. C. Quintana, “Thermal Mechanical Failure Exclusion Region Barrier Breach Foam Experiments SAND2013-7346,” Sandia National Lab.(SNL-NM), Albuquerque, NM (United States), 2013.

[47] M. E. Larsen and A. B. Dodd, “Uncertainty quantification for foam in can experiment.,” Sandia National Lab.(SNL-NM), Albuquerque, NM (United States), Sandia Internal Memorandum.

[48] R. Taylor, H. Groot, and J. Ferrier, “Thermophysical properties of two foams, TPRL 1964,” Thermophysical Properties Res. Lab, West Lafayette, IN, 1998.

[49] T. Neet, “Development of non-TDI polyurethane encapsulation foams,” PDO 705898 final report, 1994.

[50] G. Jin, G. Venkatesan, M. Chyu, and J. Zheng, “Measurement of thermal conductivity and heat capacity of foam insulation during transient heating, AV7569 final report,” Department of Mechanical Engineering, Texas Tech University, 1998.

[51] R. Siegel and J. Howell, *Thermal radiation heat transfer*, 2nd ed. Cambridge: Hemisphere Publishing, 1982.

[52] J. Reichman, “Determination of Absorption and Scattering Coefficients for Nonhomogeneous Media. 1: Theory,” *Applied Optics*, vol. 12, no. 8, pp. 1811–1815, 1973.

[53] S. Scott, J. Templeton, J. Ruthruff, P. Hough, and J. Peterson, “Computational solution verification applied to a thermal model of a ruggedized instrumentation package,” presented at the Computational Methods and Experimental Measurements XVI, A Coruña, Spain, 2013.

[54] J. Hughes, *The Finite Element Method*. Mineloa: Dover.

[55] *MATLAB*. Natick, MA: The MathWorks Inc., 2016.

[56] *Python Programming Language*. http://www.python.org: Python Software Foundation.

[57] R. M. J. Kramer and D. R. Noble, “A conformal decomposition finite element method for arbitrary discontinuities on moving interfaces: CDFEM for Arbitrary Discontinuities On Moving Interfaces,” *International Journal for Numerical Methods in Engineering*, vol. 100, no. 2, pp. 87–110, Oct. 2014.

[58] Y. Cengel and M. Boles, in *Thermodynamics: An Engineering Approach*, 5th ed., New York: McGraw-Hill, 2006, pp. 697–698.

[59] B. Adams *et al.*, *Dakota, A Multilevel Parallel Object-Oriented Framework for Design Optimization, Parameter Estimation, Uncertainty Quantification, and Sensitivity Analysis: Version 6.0 User’s Manual, SAND2014-4633*. Albuquerque, NM: Sandia National Laboratories, 2014.

[60] V. Vesovic, W. A. Wakeham, G. A. Olchowy, J. V. Sengers, J. T. R. Watson, and J. Millat, “Transport Properties of Carbon Dioxide,” *J. Phys. Chem. Ref. Data*, vol. 19, no. 3, pp. 764–808, 1990.

[61] E. Cussler, *Diffusion: Mass Transfer in Fluid Systems*, 2nd ed. New York: Cambridge University Press.

[62] P. Atkins, *Physical Chemistry*. Oxford: Oxford University Press, 2014.

[63] S. Skogestad, *Chemical and Energy Process Engineering*. CRC Press, 2008.

[64] F. Smith and A. Harvey, “Avoid Common Pitfalls When Using Henry’s Law,” *Chem. Eng. Progress*, vol. 2007, no. September, pp. 33–39.

[65] T. H. Fletcher, A. R. Kerstein, R. J. Pugmire, M. Solum, and D. M. Grant, “A chemical percolation model for devolatilization: summary,” *Brigham Young University*, 1992.

[66] National Institute of Standards and Technology, “Chemistry Webbook: Aniline.” .

[67] M. Hobbs, K. Erickson, and T. Chu, “Modeling decomposition of unconfined rigid polyurethane foam,” *Polymer Degradation and Stability*, vol. 69, pp. 47–66, 2000.

[68] P. Luehring and A. Schumpe, “Gas solubilities (hydrogen, helium, nitrogen, carbon monoxide, oxygen, argon, carbon dioxide) in organic liquids at 293.2 K,” *Journal of Chemical and Engineering Data*, vol. 34, no. 2, pp. 250–252, 1989.

[69] A. Saltelli, K. Chan, and E. Scott, “Chapter 6,” in *Sensitivity analysis*, New York: Wiley.

[70] J. Helton, “Latin hypercube sampling and the propagation of uncertainty in analyses of complex systems,” Sandia National Laboratories, Albuquerque, SAND2001-0417, 2001.

DISTRIBUTION

1	MS0825	Roy Hogan	1514
1	MS0825	James Hartley	1514
1	MS0836	Nick Francis	1514
1	MS0836	Joe Shelton	1514
1	MS0840	Tim Koehler	1513
1	MS9042	Terry Johnson	8253
1	MS9042	Curt Nilsen	8253
1	MS9052	Amanda Dodd	8366
1	MS9159	Patricia Hough	8754
1	MS9957	Victor Brunini	8253
1	MS9957	Tricia Gharagozloo	8253
1	MS9957	Ryan Keedy	8253
1	MS9957	Matthew Kury	8253
1	MS9957	Jeremy Templeton	1151
1	MS0899	Technical Library	9536 (electronic copy)

Sandia National Laboratories